UNIVERSITY OF GHANA

COLLEGE OF BASIC AND APPLIED SCIENCES

COMPUTATIONAL ASSESSMENT OF THE INFLUENCE OF BEAM HARDENING FILTERS ON IMAGE QUALITY AND PATIENT DOSE IN CT SCANNERS

BY

EMMANUEL WORD ATTAAKU

(10934571)

THIS THESIS / DISSERTATION IS SUBMITTED TO THE UNIVERSITY OF GHANA, LEGON IN PARTIAL FULFILMENT OF THE REQUIREMENT FOR THE AWARD OF MPHIL MEDICAL PHYSICS DEGREE.

DEPARTMENT OF MEDICAL PHYSICS

MAY, 2025

DECLARATION

This thesis is the result of research work carried out by Emmanuel Word Attaaku in the Department of Medical Physics, School of Nuclear and Allied Sciences, University of Ghana, under the supervision of Prof. Stephen Inkoom, Dr. Theresa Bebaaku Dery and Dr. William Osei-Mensah

It is my conviction that, no part of this work has been presented in part or whole to any other university or institution for the award of a diploma, or degree at any level. Duly other works and/or researches cited in this work have been acknowledged under references.

Sign: ..... Sign: .....

Emmanuel Word Attaaku

(Student)

Date: 26TH OCTOBER, 2025.

Professor Stephen Inkoom

(Principal Supervisor)

Date: 26TH OCTOBER, 2025.

Sign.. ..... Sign: .....

Dr. Theresa Bebaaku Dery

(Co-Supervisor)

Date: 26TH OCTOBER, 2025.

Dr. William Osei-Mensah

(Co-Supervisor)

Date: 26TH OCTOBER, 2025.

ABSTRACT

Beam hardening filters have long been employed in X-ray Computed Tomography (CT) to preferentially absorb soft and low-energy X-rays having no or little contribution to image formation, thus allowing the reduction of patient dose and beam hardening artefacts. The aim of the study was to develop a computational program to assess the influence of additional copper (Cu) and aluminium (Al) filters on patient dose and image quality, and seek an optimum filter thickness for the CT scanner using virtual experimental phantom measurements. Computed Tomography (CT) is crucial for medical diagnosis, but concerns about high radiation doses necessitate minimizing patient exposure without compromising image quality. The effectiveness of beam hardening filters as a solution was investigated. Using the Monte Carlo N-Particle Code (MCNP) and Virtual Editor (VIS ED), a 64-slice Philips CT scanner was modeled in an experimental research design. Computational Catphan phantoms representing human tissues were utilized to assess different BHF configurations' impact on image quality and patient radiation dose. Statistical analysis was performed using SPSS. The study revealed that beam hardening filters significantly affect patient dose and image quality. The optimal beam hardening filter, that balances patient dose and image quality was the 0.48 mm thickness of the conically shaped additional copper filter, or the 1.61 mm thickness of the Rectangular shaped additional Copper beam filter. And for Aluminium the optimum filter that give best quality image was the 2.60 mm conically shaped additional Aluminium beam filter. Striking a compromise between dose reduction and image quality preservation. These findings attest to the effectiveness of the optimal filter thicknesses in providing adequate filtration. Substantial reduction in patient dose was achieved while maintaining reasonable image quality in terms of contrast and spatial resolution.

DEDICATION

This research work is dedicated to my immediate family; my children, Rev. J. W. and Mrs. Felicia Atta-Kweku my parents and not forgetting my siblings, Victor A. Attaaku and Priscilla A. Attaaku and my sweet hero and herons of my loin Nhyria K. Atta-Kweku and Lynn Ramsdale Adom Atta-Kweku.

ACKNOWLEDGEMENT

I want to specially thank my most able supervisors with a grateful heart, Prof. Stephen Inkoom, Dr William Osei-Mensah, and Dr Theresa Bebaaku Dery for their marvelous contributions, constructive criticism, corrections, encouragement and guidance throughout the time of putting together this research.

I am also thankful to Rev. Joseph Wilfred and Mrs. Felicia A. Omani Atta-Kweku, my parents and Victor K. A. Attaaku and Priscilla A. Attaaku, my siblings for always supporting me psychologically and financially and my very small nuclear family, Kofi Nhyria Atta-Kweku and Lynn Ramsdale Adom Atta-Kweku.

Finally, a special thank you to all my family and friends, especially Nana Akwaba Amankrah for always being on my nerves to study even when I am sleeping and all St Mary's Boys' Senior High school (Takoradi-Apowa) 2023 and 2024 batch of science students who were exposed to Tertiary education as they often see me on my project work.

TABLE OF CONTENTS

Contents **Page**

LIST OF FIGURES

LIST OF TABLES

LIST OF ABBREVIATIONS

BHF	Beam Hardening Filter
SHP	Spherical Head Phantom
ABHF	Additional Beam Hardening Filter
AABHF	Additional Aluminium Beam Hardening Filter
ACBHF	Additional Copper Beam Hardening Filter
RABHF	Rectangularly shaped Additional Beam Hardening Filter
CAABHF	Conically shaped Additional Aluminium Beam Hardening Filter
CAC	
BHF	Conically shaped Additional Copper Beam Hardening Filter
UGMC	University of Ghana Medical Centre
SPSS	Statistical Package for the Social Sciences
RAABHF	Rectangular-shaped Additional Aluminium Beam Hardening Filter
CT	Computer Tomography
RACBHF	Rectangular-shaped Additional Copper Beam Hardening Filter
2-D	Two Dimensional
3-D	Three Dimensional
CAT	Computerized Axial Tomography
ALARA	As Low as Reasonably Achievable
MCNP	Monte Carlo N-Particle Code
VIS ED	Virtual Editor
WET	Water equivalent thickness

CHAPTER ONE

INTRODUCTION

1.1 Background

Computed Tomography (CT) is a valuable diagnostic tool in modern radiology, providing non-destructive, rapid imaging of internal structures with detailed image output. CT has therefore emerged the preferred cross-sectional diagnostic imaging method (Rogalla, *et al.*, 2009). However, the use of ionizing radiation in CT exposes patients to high radiation doses, because when polychromatic X-ray beams used for CT imaging travel through the patient, soft and low energy X-rays, which are not very important for image formation are preferably highly absorbed compared to high-energy photons.

According to compelling epidemiological studies conducted by Rehani et al. (2001), it has been experimentally established that the absorbed dose from CT scans can frequently reach or exceed critical levels. This worrisome finding reveals that higher doses of radiation absorbed by patients could significantly increase the risk of radiation side effects and potential carcinogenic effects, as solidified by expert consensus from the International Commission on Radiological Protection (ICRP, 2007) and Rehani et al. (2001).

One strategy to address this issue is the installation of an additional beam hardening filter (BHF) to the collimator of the CT scanner, which could reduce the patient's exposure to radiation by further filtering the X-ray stream. This results in a more homogenous beam that could be used for imaging, reducing both the effect of beam hardening and the absorbed dose of the patient. Studies have shown that the addition of a BHF could significantly reduce patient radiation dose (Ay *et al.*, 2013; Robert, 1988), making CT safer for patients.

However, the attachment of an additional BHF to the collimator of the CT scanner may increase statistical noise or quantum mottle and reduce the ability to identify low contrast (Cruz-Bastida *et al.*, 2014). These limitations could be mitigated through computational assessment and optimization of the CT beam filters to reduce patient radiation dose while improving image resolution.

Therefore, the attachment of an additional BHF to the collimator of the CT scanner could significantly reduce patient radiation dose and make CT a safer and more effective diagnostic tool. Computational assessment and optimization of the CT beam filters could further improve image quality while minimizing radiation exposure, helping to maintain CT's advantage over other imaging technologies.

1.2 Statement of Problem

CT is a widely used and highly effective imaging modality that has revolutionized the field of medical imaging. But considering the collection of publications as illustrated in figure 1.1 below, undertaking CT scan poses much danger and detrimental effects to patients.

Figure 1. 1:A collection of screenshot images of publications stating the consequences undertaking imaging by CT scanning

These may be as a result of the use of inadequate filtration during CT imaging procedures which pose a significant risk to patient health, including exposure to harmful radiation that can lead to cancer and other serious health conditions. On the other hand, excessive filtration can lead to poor image quality and incorrect diagnoses, compromising the effectiveness of CT imaging. These challenges pose by inadequate filtration and excessive filtration exists because of the nature of polychromatic X-ray beams used for the CT scanning and the internal in-built beam hardening filters of the CT scanner.

To address these critical issues, this research study is conducted to evaluate the influence of beam hardening filters (BHF) on image quality and patient dose in the Philip brand 64-slice X-ray CT scanner and provide valuable insights into the optimal filter thickness that balances patient safety with image quality.

By identifying the ideal BHF thickness, this will help to minimize the risks associated with CT imaging and enhance diagnostic accuracy. This will ultimately translate into improved patient care, better treatment outcomes, and reduced healthcare costs.

1.3 Objective of the Study

The main objective for the study was to obtain an optimum filter thickness for the 64-slice CT scanner using computational approach.

The specific objectives were;

1. Simulation of additional filters and evaluate its effect on patient dose and image quality using the Monte Carlo software.
2. Assessment of the effect of X-ray filtration on image resolution

1.4 Relevance and Justification

The proposed research study was critically important because it would address a significant gap in the literature by evaluating the impact of beam hardening filters (BHF) on patient dose and image quality. The findings of this study would have practical implications for healthcare professionals, helping them to make more informed decisions regarding CT imaging procedures and ultimately improving patient care.

This study was particularly timely given the growing concern regarding the widespread reliance and preference of both patients and clinicians for CT scans as the primary imaging modality for medical procedures involving ionizing radiation. It is imperative that studies be made to delve into the intricacies of this technology to ensure its optimal utilization, minimize potential health risks and improve the cost-effectiveness of CT imaging. By developing techniques to reduce radiation

doses during CT imaging, unique opportunity to address these pressing concerns, enhance patient safety, and contribute to the advancement of medical imaging practices.

In addition, this research study has the potential to revolutionize CT imaging by providing valuable information for optimizing CT imaging protocols and improving diagnostic accuracy while minimizing radiation exposure. By using computational models to assess the impact of BHF on image quality and patient dose, informed decisions could be made regarding CT imaging procedures, ensuring that patients receive the most effective and safest diagnostic tests possible. The findings of this study would have a significant impact on patient safety, diagnostic accuracy, and healthcare costs, making it an essential area of research for the future of medical imaging.

1.5 Scope and Limitations of the Study

One limitation was the use of digital phantoms instead of human subjects. Although this approach is common in the field of medical physics, the results may not fully depict the effects of BHF on human subjects in a clinical setting. This is because computational simulations may not replicate all the complexities of the imaging process *in vivo*.

Despite these limitations, the study offers valuable insights into the effectiveness of different BHF compositions and thicknesses, and the analysis conducted with software will provide reliable and valid results.

1.6 Organization of the Thesis

This study structurally comprises of five chapters. And in addition to the afore written introductory Chapter, there are four other chapters. The introductory Chapter also known as Chapter 1, introduces the research study with the background of the study, the problem statement, objective

and relevance of the study. The Chapter 2 provides a literature review of previous studies related to the scope of the research, ensuring that the study is grounded in relevant theoretical concepts and methods. Chapter 3 describes the use of computational models and thus provides valuable insights into the optimal design of BHF and its impact on image quality and diagnostic accuracy.

The results of the study are presented in Chapter 4, followed by discussion and analysis of the findings. The contribution of the study to knowledge is highlighted in this section, demonstrating the importance of the research for improving patient safety, diagnostic accuracy, and healthcare costs.

The Chapter 5 is the conclusion and recommendations of the study. The recommendations for policy, practice, and further research in the final chapter underscore the significance of this research. All supporting details can be found in the appendix.

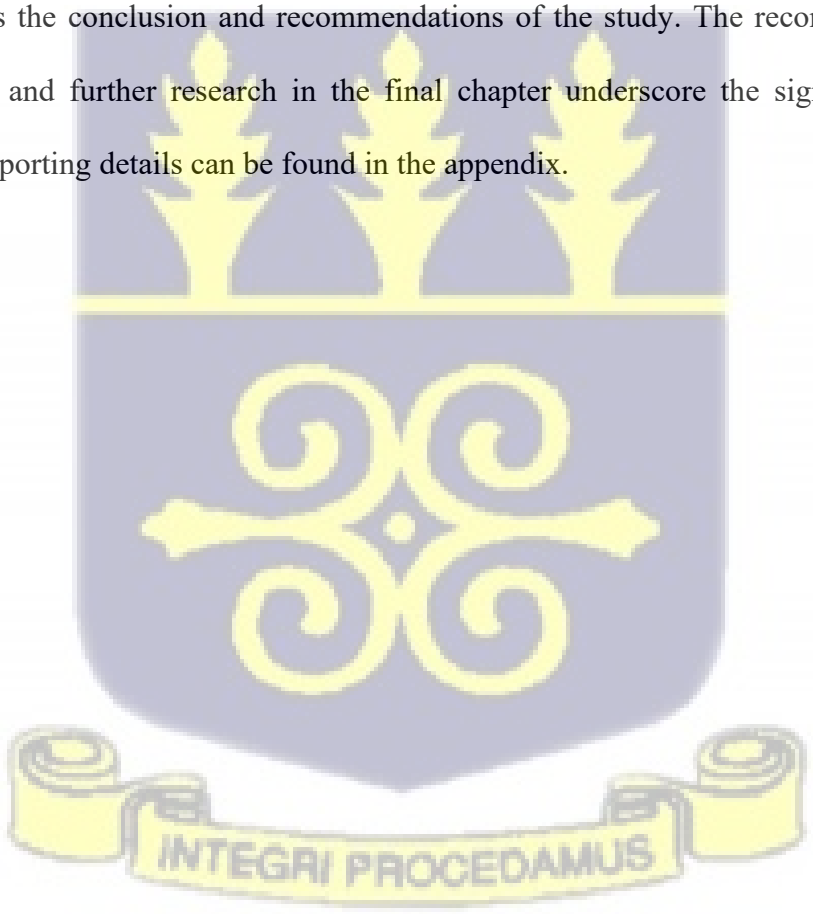

CHAPTER TWO

LITERATURE REVIEW

This chapter provides detailed background regarding basic knowledge in CT and Beam hardening. This chapter provides a review of relevant literature applicable to this research study.

2.1 The Computed Tomography

The CT is one many imaging modalities and widely used. The CT scan as a system is made up of different components but of critical interest to the study is the X-ray tube, detectors and the inherent filters.

The CT as an imaging technique combines X-ray technology with advanced computer algorithms to generate detailed cross-sectional images ("slices") of the human body (Villarraga-Gómez, *et al.*, 2019). Villarraga-Gómez, *et al. (2019)* further mentioned that, CT offers several advantages over other imaging modalities. It provides valuable information with excellent spatial resolution, which aid visualization of small structures and abnormalities for the diagnosis, treatment planning, and monitoring of various medical conditions. Additionally, CT imaging can be performed rapidly, making it particularly useful in emergency situations (Schmidt, 2012). The Cross-sections are reconstructed from measurements of attenuation coefficients of X-ray beams passing through the volume of the object under study (Michael, 2001).

However, CT imaging is associated with ionizing radiation exposure, which raises concerns about potential risks, particularly with repeated or high-dose examinations (Kalra, et al., 2004). But according to Schmidt (2012) scientists canot state conclusively that CT scans cause cancer until ongoing prospective studies of that link generate results. In the meantime, they estimate cancer outcomes using dose–response models derived from other radiation-exposed groups, such as

atomic-bomb survivors and patients treated with radiation. Efforts to optimize CT imaging protocols and reduce radiation dose to patients while maintaining image quality have been a major focus of research and technological advancements in the field (Ay, et al., 2013).

2.1.1 The Operation of the CT scan

The CT works basically on the principle of measuring the density of the tissue under study by the calculation of the attenuation coefficient as X-ray beam passing through tissues of an object. By this fundamental principle, the CT scan allows the reconstruction of the density of the body, by a two-dimensional section perpendicular to the axis of the acquisition system (Hsieh, Computed tomography: principles, design, artifacts, and recent advances., 2003; Hendee & Ritenour, Medical imaging physics, 2003).

The patient is placed on the couch and automatically moved through the scanner, as the X-ray beams and detectors rotate around the bed. The X-ray tube emits bremsstrahlung photons, as well as characteristic X-rays. The photons that reach the detector are less than the photons that are emitted due to attenuation in the patient. Attenuation values of the X-ray beam are recorded and the data is used to build a 3-D representation of the scanned object/tissue which is called the image.

2.1.2 Image Formation

Unlike traditional X-ray imaging in radiography, which relies on radiographic film as a detector to directly capture images, Computed Tomography (CT) utilizes digital detectors that convert X-ray data into images through a complex reconstruction process. Concerning image construction by the CT, the image of the section of the object irradiated by the X-ray is reconstructed from a large number of measurements of attenuation coefficient. It gathers together all the data coming from the elementary volumes of material through the detectors. Using the computer, it presents the

elementary surfaces of the reconstructed image from a projection of the data matrix reconstruction, the tone depending on the attenuation coefficients (Michael, 2001).

Therefore, the image constructed by the CT is a digital image that consists of a square matrix of elements (pixel), each of which represents a voxel (volume element) of the tissue of the patient as illustrated in figure 2.1. The measurement made by a CT scan detector is proportional to the sum of the attenuation coefficients.

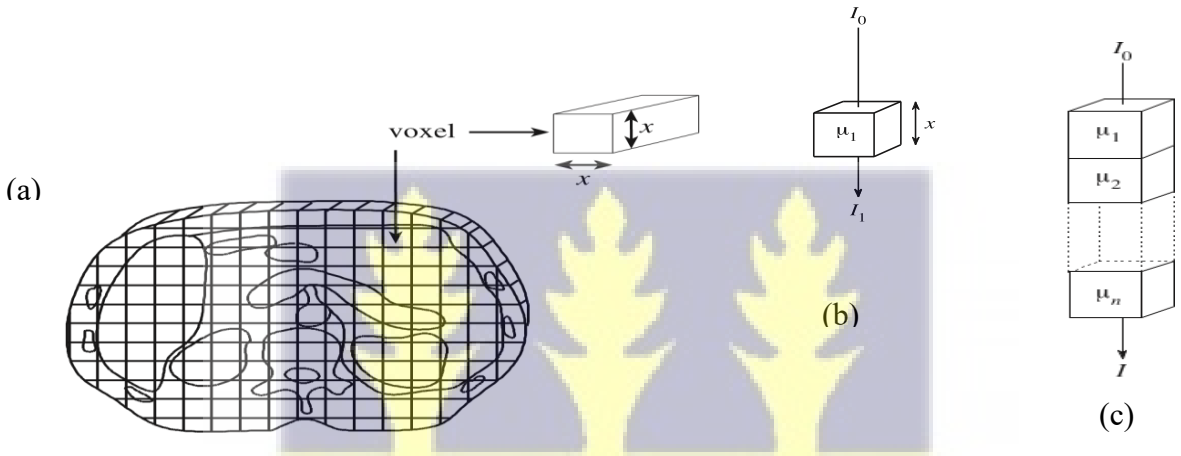

Figure 2. 1;**Image Formation** (a) Each pixel in the image represents a voxel of tissue in the Patient (b) The transmission of an X-ray beam through a single voxel, and (c) A ray sum is the sum of attenuation coefficients along the path of a single ray through the pat

If the X-ray beam is assumed to be a single energy, the incident intensity of the unattenuated X-ray beam $\boldsymbol{I_0}$, travelling through a small volume of patient tissue of thickness χ and an attenuation coefficient $\boldsymbol{\mu_1}$ then the intensity of the transmitted X-ray beam $\boldsymbol{I_1}$, is given as

$$I_1 = I_0 e^{\mu_1 x} \qquad (1)$$

The intensity of the incoming X-ray beam will be determined by;

$$I = I_0 e^{-\chi \Sigma_{i=1}^{n} \mu_1} \qquad (2)$$

The equation (2) could be rearranged as;

$$In\frac{I_0}{I} = x\sum_{i=1}^{n}\mu_1 \qquad (3)$$

As a result, the attenuation coefficients of the voxels in the path of the beam are proportional to the natural logarithm of the ratio of incident to transmitted X-ray intensity.

The typical CT image is composed of 512 rows, each of 512 pixels, i.e., a square matrix of 512 x 512 = 262,144 pixels (one for each voxel). In the processing of the image, the value of the attenuated coefficient for each voxel corresponding to these pixels needs to be calculated. A tomographic image of the patient is then constructed by a computer using complex mathematical algorithms based on the "pre-processed" CT dataset (Fleischmann & Boas, 2011).

2.1.3 Image Display

The CT scanner translates the measured voxel attenuation coefficients to CT numbers before the image are displayed on the screen. The relationship between a voxel's attenuation coefficient, $\boldsymbol{\mu_1}$ and the accompanying pixel's CT number N_i for that voxel is as follows:

$$N_i = 1000 \times \frac{\mu_1 - \mu_w}{\mu_w} \qquad (4)$$

where μ_w is the attenuation coefficient of water.

The CT number is based on measurements carried out using the premier clinical CT scanner, the EMI Mark 1 head scanner in 1972 by Sir Godfrey Hounsfield, relating the linear attenuation coefficient of a localised region of a material under study with the attenuation coefficient of water (Thomas, et al., 2005). The CT is expressed in dimensionless Hounsfield Units (HU) as an integer. As a result, less computer memory and storage space is needed. So, the signal transmitted by the

detector is processed by the PC in the form of digital information for the CT image reconstruction. But this image may be degraded by artifacts.

2.2.0 Beam Hardening Filters in Computer Tomography

The images provided by the CT provides detailed cross-sectional images of the human body or the material under study. However, the CT imaging is often affected by beam hardening challenges (Boas & Fleischmann, 2012), which can degrade image quality and compromise diagnostic accuracy. These challenges frequently occurs because the CT operate on polychromatic X-ray beams which comprises of both soft and hard X-rays.

Beam hardening occurs when low-energy X-ray photons are preferentially absorbed by the patient's body, altering the X-ray beam's energy distribution. This could cause streaks and shading artifacts in reconstructed images. Boas and Fleischmann in their studies noted that sometimes, the reconstructed X-ray images look strange, with some edges being brighter than the rest, even if the material is the same all over this is usually referred to as “beam Hardening artifacts”. This challenge usually comes from the hypothesis that X-ray beam emission is linear rather than a spectrum mix of different energies (Karabut, 2006).

To mitigate these artifacts challenge and enhance image quality, beam hardening filters (BHF) was first suggested in 1978 and introduced inherently into the CT scanner (Kalender, 2011). Beam hardening filters are used to selectively attenuate higher energy X-rays, leading to a more uniform X-ray spectrum, minimising artifacts and produces improved image quality for diagnostic accuracy. Beam Hardening filters (BHF) are metal sheets which are typically made low atomic number (Z) materials such as aluminium (Al), copper (Cu) or high-Z materials such as tungsten (W) or molybdenum (Mo) that are placed in the path of the X-ray beam before it enters the patient

to “pre-harden” the X-ray spectrum or in otherwise selectively absorb low-energy X-rays and minimise the low energy photon which would not contribute any way to image formation.

However, beam pre-hardening, also known as beam filtration again can be done, if possible, by placing the whole sample(s) in a metal tube or liquid bath and use the surrounding metal or liquid as a filter material, reducing not only soft X-rays from the source, but also the scattering effect.

In 64-slice CT scanners made by Philips, there are filters added to the spinning part of the scanner called the gantry (Philips, 2021) and Boas & Fleischmann, 2012. These filters can be made thicker or thinner and have different shapes. It all depends on what kind of pictures are needed for the patient and the diagnosis. For instance, thinner filters might be used for kids or to see small things, while thicker filters could be used for bigger patients or to look at dense things like bones.

Chen, et al.(2016) in their study proposed a new beam hardening correction method using a filter based on material decomposition. The filter was designed to separate the X-ray beam into two parts, a high-energy and a low-energy beam, and then recombine them in such a way that the beam hardening effect is reduced. The filter was evaluated using both simulated and experimental data, and the results showed that the filter was effective in reducing the beam hardening artifact, resulting in images with improved contrast and accuracy.

Benítez et al. (2010) also investigated the use of a beam hardening filter in CT imaging. In their study, they proposed a filter based on the concept of beam hardening index (BHI), which is a measure of the degree of beam hardening in the image. The filter was designed to reduce the BHI value by selectively attenuating the high-energy part of the X-ray beam. The filter was evaluated using both phantom and clinical data, and the results showed that the filter was effective in reducing the beam hardening artifact and improving image quality. Beam filtration is found to be

effective in reducing the artifact and improving image quality in both experimental and clinical settings.

2.2.1 Theory Beam Hardening Filters

The use of beam hardening filters in CT imaging is based on the principle of energy-dependent X-ray attenuation. According to the Beer-Lambert law, the attenuation of an X-ray beam as it passes through a material is proportional to the material's thickness and its linear attenuation coefficient.

$$I = I_0 e^{\left(-\frac{\mu}{\rho}\right)\rho\chi} \qquad (5)$$

where I_0 is the intensity of the unattenuated X-ray beam, and I is the beam's intensity after it traverses a thickness of Material $\boldsymbol{x}$ characterized by a linear attenuation coefficient $\boldsymbol{\mu}$. The term μ/ρ is the mass attenuation coefficient (cm^{-2} g^{-1}) of the object. The linear attenuation coefficient is a function of the energy of the X-rays and the atomic number of the material (Kalender, 2011).

The design of beam hardening filters involves selecting either low-Z materials or a high-Z material that can efficiently absorb low-energy X-rays. The Aluminium and Copper material are commonly used materials for beam hardening filters in CT imaging, as they have low atomic numbers and good X-ray absorption properties.

Recent advances in beam hardening filter design include the use of multi-material filters that can selectively absorb different energy ranges of X-rays. For example, a dual-layer filter can be designed with a low-Z material on the top layer to selectively absorb low-energy X-rays, and a high-Z material on the bottom layer to absorb higher energy X-rays (Chen, et al., 2016).

2.2.2 The Effect of Filtration of X-ray Beams

While beam hardening filters are helpful in making CT scan images better and more accurate, they also have some limitations (Ay, et al., 2013). For instance, using filters can make the patient

receive more radiation because extra X-rays are needed to make up for the low-energy X-rays absorbed by the filter. Also, using filters can make the images less clear due to more noise. Both instances inadequate filtration and excessive filtration could be detrimental to patients, as patients will receive higher doses as a result of soft and low energy X-rays. The experience of beam hardening artifacts which can complicate image interpretation and diagnoses, potentially mimicking or hiding pathological conditions. The intensity of the X-ray beam post-filtering affects both patient exposure and image quality, with high contrast objects leading to degraded images and reduced clinical accuracy. The balance between using higher energy radiation for better imaging quality and considering factors like beam filters is highlighted (Martin, 2007).

Beam filters are important in CT scans. Glas (2000) and Ay *et al.* (May 2013) emphasis that beam hardening using filters impact image quality and diagnostic accuracy. This effect of using BHF can either be positively or negative. They help to decrease certain image issues caused by beam hardening and make the images better. Using filters needs to be done carefully because it might mean more radiation and noise in the images. Scientists keep working on designing and improving these filters to make CT scans even better and safer for patients (Pelc, 2014).

2.3 Computational Models

Computational models have been developed to assess the performance of beam hardening filters. These models simulate the interaction of X-rays with different materials and geometries to predict the attenuation of the X-rays and the corresponding CT image quality. By using computational models, researchers can optimize the design of beam hardening filters for specific imaging applications and patient sizes.

The Monte Carlo simulation is a stochastic method that simulates the movement of individual X-ray photons through different materials, allowing researchers to predict the attenuation of X-rays and the corresponding CT image quality. In a study by Zhao (2017), a Monte Carlo simulation was used to optimize the design of a tungsten-based beam hardening filter for pediatric cardiac CT imaging. The simulation predicted the optimal thickness of the filter and its performance in reducing beam hardening artifacts.

Another computational model for beam hardening is the finite element method (FEM). FEM models simulate the physical behavior of materials under external forces, such as X-ray radiation. In a study by Barua *et al.* (2022) an FEM model was used to optimize the design of a beam hardening filter for CT imaging of high-density materials such as bone. The FEM model predicted the optimal shape and thickness of the filter to reduce beam hardening artifacts while maintaining image quality.

Computational models provide a valuable tool for assessing the performance of beam hardening filters in CT imaging. By using Monte Carlo simulations or finite element models, researchers can optimize the design of filters for specific imaging applications and patient sizes, leading to improved image quality and diagnostic accuracy.

2.3.1 Monte Carlo N-Particle Code

The Monte Carlo N-Particle (MCNP) code stands as an indispensable cornerstone for scientists and researchers across diverse fields, propelling the boundaries of scientific simulation and technological innovation. The MCNP N-Particle code was developed by Los Alamos National Laboratory. The whole development idea of the MCNP code started at Los Alamos National Laboratory in the 1940s when by Fermi, Ulam, Metropolis, von Neumann, and Richtmyer introduced the concept of Monte Carlo method for solving complex mathematical problems

(Forster III, Rising, & Sood, 2021). The MCNP code is a capable tool for simulating the transport of various particles such as photons, neutron, electrons and other charged particles. The code's continuous development has been driven by the growing demand for accurate and efficient simulations in diverse scientific domains.

The use of the Monte Carlo N-Particle Code in developing a computational program for the CT scanner has been extensively explored in the literature. Ay (2005) developed a simulator for fan- and cone-beam CT scanners, which was validated through comparison with experimental measurements. Jansen (2009) used Monte Carlo calculations to derive normalized organ doses from CT examinations, with a focus on software optimization and X-ray source modeling. Chantzi (2020) designed a Monte Carlo model for a Dual Source Computed Tomography (DSCT) scanner, which was validated for dose and image quality assessment. Manser (2017) implemented a Monte Carlo model for an in vivo micro CT system, focusing on characterizing scatter radiation. These studies collectively demonstrate the versatility and effectiveness of the Monte Carlo N-Particle Code in developing computational programs for CT scanners, with applications ranging from scanner performance evaluation to dose and image quality assessment.

2.3.2 Virtual Editor

The Visual Editor for Monte Carlo N-Particle is recognized internationally as the best code for visually creating and graphically displaying input files for MCNP (Schwarz, *et al.*., 2005). The visual editor software for the MCNP computer code enables the creation of the geometry portion of an input file while dynamically viewing the geometry as it evolves.

The Virtual Editor is a valuable tool for simulation and computational experimental studies, as it can enhance real experiments (Zheng, 2010), aid in understanding complex structures and

principles (Yubao, 2017), and simplify the validation of systems and experiments (Sklyarov, 2009).

The development of a visual editor for the MCNP code has significantly enhanced its usability, allowing for the creation and modification of input files with ease (Schwarz, 1994). This tool has been further improved to read in 2D CAD files, expanding its capabilities (Schwarz, 2005). These advancements have made the simulation of a CT scanner program with the MCNP code more accessible and efficient.

2.4 Validating of Computational Models

Validating computational models for assessing the performance of beam hardening filters in computed tomography imaging is crucial to ensure their accuracy and reliability. Validation involves comparing the predictions of the computational model to experimental measurements to verify their consistency and reliability. In the case of beam hardening filters, validation typically involves measuring the attenuation of X-rays through different materials and comparing them to the predictions of the computational model.

One method for validating computational models is the use of phantoms, which are objects designed to mimic the physical properties of human tissue. Phantoms can be made from materials with known attenuation coefficients, allowing researchers to measure the attenuation of X-rays passing through them and compare them to the predictions of the computational model. In a study by Ay, *et al.*, (2013) a cylindrical phantom was used to validate the accuracy of a computational model for assessing the performance of a beam hardening filter in CT imaging. The phantom was made from different materials, and the attenuation of X-rays through the phantom was measured experimentally and compared to the predictions of the computational model. The results showed

good agreement between the experimental measurements and the predictions of the computational model.

Another method for validating computational models is to compare the predictions of the model to experimental measurements of CT image quality. In a study by Choi *et al., (2020)*., a computational model was developed to optimize the design of a beam hardening filter for CT imaging of high-density materials. The predicted attenuation of X-rays through the filter was compared to experimental measurements, and the resulting CT images were evaluated for image quality. The results showed that the predicted attenuation matched well with the experimental measurements and that the optimized filter design led to improved image quality.

2.5 Quantitative Analysis

Quantitative analysis of beam hardening filters is important to optimize their performance in CT imaging. Several methods have been proposed for quantitative analysis of beam hardening filters in a 64-slice CT. Water equivalent thickness, noise and contrast, and image-based analysis are some of the methods used for quantitative analysis of beam hardening filters in a 64-slice CT. By using these methods, researchers can optimize the design of beam hardening filters for specific imaging applications and patient sizes,

2.5.1 Water Equivalent Thickness:

Water equivalent thickness (WET) is a commonly used parameter for characterizing the performance of beam hardening filters. WET is defined as the thickness of water that would produce the same level of attenuation as the filter. In a study by Khattak *et al.* (2018), they noted that the WET of different beam hardening filters was measured using a 64-slice CT. The study found that the WET of the filter increased with its thickness and atomic number.

2.5.2 Noise and Contrast:

Noise and contrast are important parameters for assessing the performance of beam hardening filters in CT imaging. Noise refers to the variation in CT image intensity that is unrelated to the object being imaged. Contrast refers to the difference in CT image intensity between different regions of the object. According to the research study by Chu *et al.,* (1981), the noise and contrast of a tungsten-based beam hardening filter were compared to those of an aluminium-based filter. The study found that the tungsten-based filter produced lower noise and higher contrast than the aluminium-based filter.

2.5.3 Image-Based Analysis:

Image-based analysis is another method for quantitatively analysing of the performance of beam hardening filters in CT imaging. Image-based analysis involves comparing CT images with and without the filter to assess the improvement in image quality. In a study by Rana et al., (2015), the performance of different beam hardening filters was compared using image-based analysis. The study found that a Aluminium-based filter produced the highest improvement in image quality.

2.5.4 Different Beam Hardening Filter

Different types of materials are used as beam hardening filters, each with unique material properties and thicknesses. Therefore, a comparison of different beam hardening filters is necessary to determine which filter is best suited for a particular imaging application.

Ay et al., (2013), compared the performance of two different beam hardening filters, one made of Aluminium and the other made of copper, in a 64-slice CT. The study found that both were effective in reducing radiation absorption dose but the Aluminium filter had a higher water equivalent thickness (WET) than the Copper filter therefore less of Cu than Al is needed to

attenuate same beam to a certain value, However, the Copper filter produced less noise in the reconstructed images, suggesting that it could be used in situations where noise is a concern.

Another study by Szulc and Judy (1979) compared the performance different beam hardening filters. The study found that filter materials with atomic number between 29 to 40 are optimal for CT scanners and recommended if the filter material is aluminium the possible minimum thickness should be 4 mm to give the highest improvement in image quality. For Jennings (1988), four filters were compared in a 64-slice CT. The filters were made of aluminium, copper, brass, and iron. The study made a conclusion that found that copper (Cu) beam hardening filters are preferable to aluminium filters as they are about 10% more efficient. However, in a study on the optimization of the thickness of the Cu filter for contrast-enhanced projection radiology, Morrell et al., (2004), reported that 0.3 mm Cu reduces the rate of entrance surface dose by 56% without significantly affecting image contrast.

It can be deduced that; the comparison of different beam hardening filters is necessary to determine which filter is best suited for a particular imaging application. The performance of the filter can be evaluated using parameters such as WET, noise, and contrast. Overall, the choice of beam hardening filter will depend on the specific imaging application and the trade-offs between different parameters.

2.7 Influence of Beam Hardening Filters on Image Quality

Beam hardening filters are commonly used in computed tomography (CT) imaging to improve image quality by reducing beam hardening artifacts. However, the use of filters can also have an impact on image quality and diagnostic accuracy, which is an important consideration when choosing a filter for a particular imaging application.

A study by Ay *et al.,* (2013) evaluated the impact of two different beam hardening filters, one made of aluminium and the other made of a copper material, on image quality and diagnostic accuracy in a 64-slice CT. The study found that both filters significantly reduced beam hardening artifacts and improved image quality. However, the copper filter produced less noise in the reconstructed images and had a higher signal-to-noise ratio, indicating that it could improve diagnostic accuracy.

In another study, Chen, et al., (2016) evaluated the impact of different beam hardening filters, including a water phantom, on image quality and diagnostic accuracy in a 64-slice CT. The study found that the use of a water phantom as a filter significantly reduced beam hardening artifacts and improved image quality. However, the use of the water phantom also reduced the contrast of the images, which could have a negative impact on diagnostic accuracy.

A study by Faby *et al., (2015)* compared the diagnostic accuracy of two different beam hardening filters, one made of aluminium and the other made of a composite material of tungsten and epoxy resin, in a 64-slice CT. The study found that both filters significantly reduced beam hardening artifacts and improved image quality. However, the composite filter produced higher contrast and had a higher signal-to-noise ratio, indicating that it could improve diagnostic accuracy.

The choice of beam hardening filter can have a significant impact on image quality and diagnostic accuracy in CT imaging. The performance of the filter can be evaluated using parameters such as noise, signal-to-noise ratio, and contrast. While the use of a filter can improve image quality, it is important to consider the potential trade-offs between image quality and diagnostic accuracy when choosing a filter for a particular imaging application.

2.8 The Phantom

Virtual phantoms have emerged as a valuable tool in medical imaging research, offering a practical means to evaluate and improve imaging devices and techniques. The virtual phantoms help provide a reference signal without the need for the physical phantom such as validation of imaging techniques, optimisation protocols, and assessment performance parameters especially in experimental studies on computed tomography (CT) scans. Moström (1986) emphasized the value of biologic phantoms in evaluating and comparing CT scanner performance, particularly in simulating the clinical setting. Plautz (2012) further demonstrated the potential of phantoms in optimizing radiography performance of a clinical proton CT scanner. Olerud (1999) developed an anthropomorphic phantom for quantitative assessment of image quality in CT, showing a positive correlation between dose and image quality. Nakaya (2014) extended this concept by developing a CT phantom for the development of a robotic Interventional Radiology system, highlighting the importance of phantoms in experimental studies for medical imaging equipment. Various types of phantoms are employed in CT studies, each serving a specific purpose.

2.8.1 The Catphan phantom

The Catphan phantom, a widely used tool for evaluating CT image quality, has been found to provide stable results over time, with axial scans showing better low-contrast resolution and less noise than helical scans (Husby et al., 2017). Husby and his collaborator further found that image quality parameters remained stable over time when using the Catphan 600 phantom on a CT scanner. Goodenough (1977) developed a phantom with modular sections for measuring contrast sensitivity, sensitometric response, spatial resolution, noise, and uniformity. Davis (2020) further confirmed the reliability of the Catphan phantom, specifically the 604 model, for multi-centre image quality audits. These studies collectively highlight the importance of the Catphan phantom

in ensuring the accuracy and reliability of CT imaging. This stability is crucial for ensuring the accuracy and reliability of CT imaging. The Catphan phantom provides complete characterization of maximum imaging performance for axial and spiral CT scanners. The Catphan 500 provides a comprehensive set of measurements to evaluate your CT scanner's sensitometry, uniformity, geometric and low contrast sensitivity performance. It consists of 4 modules enclosed in a 20 cm housing; such as CTP528 High Resolution Module, CTP401 Slice Geometry and Sensitometry Module, CTP486 Uniformity Module and the CTP 515 low contrast module. For the study, the CTP 515 low contrast module is of interest.

CTP515 Low Contrast Module: The CTP515 consists of a series of cylindrical rods of various diameters and three contrast levels to measure low contrast performance. The 40 mm-long rods provide consistent contrast values at all z-axis positions, thereby avoiding any volume-averaging errors as you scan through the section. The unique sub-slice test objects enable evaluation of the effectiveness of different scan protocols (pitch, slice width and reconstruction algorithms) in resolving sub-slice low contrast objects.

For selection of helical and multi-slice image protocols, unique sub-slice low contrast targets (truncated cylinders) have been included in this module. Comparing the images obtained by scanning the sub-slice targets with different imaging settings (slice width, pitch and reconstruction algorithms) provides valuable information to assist with the selection of optimal protocols for identifying small low contrast objects such as tumours.

All the various samples and the background material have equivalent effective atomic numbers; only the density is varied to produce changes in the effective attenuation coefficients. Sub-slice targets have a nominal 1.0 % contrast and z-axis lengths of 3, 5, and 7 mm. For each of these lengths, there are targets with diameters of 3, 5, 7 and 9 mm.

The Catphan phantom can be used to assess the effect of beam hardening filters on image quality and patient dose. The Catphan phantom is a commonly used phantom in CT imaging to evaluate the performance of imaging systems.

In the context of beam hardening filters, which are typically used in computed tomography (CT) imaging, the Catphan phantom can be employed to simulate a range of tissue densities and attenuation coefficients. By introducing different beam hardening filters and imaging techniques, the phantom can be imaged to evaluate the impact on image quality and patient dose.

The Catphan phantom mimic various tissues and can be used to simulate organs or anatomical structures of interest. By placing the phantom in the CT scanner and acquiring images with and without the beam hardening filters, the effects of the filters on image quality, such as noise, contrast, and spatial resolution, can be assessed.

Additionally, the phantom can be used to quantify the changes in patient dose resulting from the use of beam hardening filters. Radiation dose measurements can be performed using dosimeters placed within the phantom or by analysing the CT dose index (CTDI) values obtained during the imaging process. By utilizing the Catphan phantom in these experiments, researchers and clinicians can evaluate the performance of beam hardening filters, optimize imaging protocols, and make informed decisions regarding image quality and radiation dose in CT imaging.

The Sphere Head Phantom (SHP) is intricately designed spherical structure that symbolizes innovation and precision in the realm of neuroimaging. Its anatomical accuracy and tailored composition mimic the complexities of the human head, providing researchers and medical professionals with an unparalleled platform for testing, calibration, and optimization of advanced imaging modalities.

The spherical Head phantom in the field of neuroimaging is use for simulating the intricate interplay of tissues and structures within the human brain, the Sphere Head Phantom allows researchers to fine-tune imaging protocols, optimize image quality, and explore the limits of diagnostic capabilities. Its versatility enables the evaluation of various imaging modalities, including magnetic resonance imaging (MRI), positron emission tomography (PET), computed tomography (CT), and more, all within a controlled and reproducible environment.

Moreover, the Sphere Head Phantom serves as a benchmark for quantitative analysis, ensuring the accuracy and reliability of imaging measurements. By providing a known ground truth, this remarkable tool enables the validation and comparison of imaging techniques, leading to enhanced diagnostic accuracy and improved patient outcomes.

2.9 Implications for Clinical Practice

In conclusion, the use of beam hardening filters in 64-slice CT imaging has been shown to significantly reduce beam hardening artifacts and improve image quality, which could lead to more accurate diagnosis and treatment of various clinical conditions. Computational assessment of these filters has played a crucial role in identifying the most effective filters for specific clinical applications, as well as optimizing imaging parameters for optimal image quality and radiation dose.

The findings of this literature review suggest that the use of appropriate beam hardening filters in 64-slice CT imaging can help overcome some of the limitations of this imaging modality, such as beam hardening artifacts, which can reduce diagnostic accuracy. Furthermore, computational assessment of these filters can provide a cost-effective and efficient means of evaluating filter performance and optimizing imaging parameters.

In clinical practice, the selection of beam hardening filters should be based on the specific clinical application and imaging requirements. The choice of filter material, thickness, and shape can significantly influence the imaging performance of the filter, and should be carefully considered to achieve optimal image quality and radiation dose.

Overall, the use of beam hardening filters in 64-slice CT imaging represents an important advancement in CT imaging technology, and computational assessment of these filters has played a crucial role in advancing their development and optimizing their performance for clinical practice

CHAPTER THREE

MATERIALS AND METHOD

This chapter of this study describe the methods and materials used for the research study, this includes the research study design, the material and equipment employed, methodology, data collection, analysis methods, validation, and limitations to the work.

3.1 Study design

In this computational simulation study, software and modeling techniques were used to assess the effects of beam hardening filters on CT image quality and patient doses.

3.2 Materials

Monte Carlo N-Particle Code (MCNP) Version 2.7.0 and the Virtual Editor (VIS ED) were used for this study. The MCNP was used for modelling the geometry of the CT head, the source and material specification of the scanner while the VIS ED was used to set and check the geometry of the experiment.

These software programs simulate the CT scanning process with Philip's 64-slice X-ray CT scanners, taking into account BHF's influence on X-ray radiation characteristics and interactions with digital phantoms.

3.2.1 Additional Filters and Phantoms

Apart from the modeling techniques used, computationally modelled Copper (Cu) and Aluminum (Al) disc of two different shape (both rectangular and conical) and thickness (0.5 - 1.6 mm Cu, 0.53 – 4.14 mm Al) were used as Beam Hardening Filters as portrayed of Table 4.3 (Ay, et al., 2013). Each additional filter plate either Aluminum or Copper were installed on the scanner's collimator aperture.

Table 3.1: Range of additional filter thickness used for the CT imaging

Serial Number	Catphan Phantom	
	Aluminium Filters	Copper Filters
1.	0.53 mm	0.15 mm
2.	1.06 mm	0.28 mm
3.	2.60 mm	0.48 mm
4.	3.08 mm	0.68 mm
5.	4.14 mm	0.75 mm
6.	Nil	1.40 mm
7.	Nil	1.61 mm

3.2.2 Virtual Catphan 500 Phantom

The Catphan 500 phantom, is incorporated in the modelled CT scanner using the MCNP code and simulated. The virtual Catphan 500 phantom was selected based on their anatomical reliability, tissue characteristics and generalizability in clinical practice. The virtual modelled Catphan 500 phantom digitally was made up of rods as cell mimicking the composition of the human beings.

The Catphan 500 phantom was especially designed for evaluation of various image quality parameters in CT and was used worldwide for image quality assurance testing. The quick and easy positioning of the Catphan phantom makes it best for routine quality assurance of any CT machine. The Catphan phantom's patented design includes many exclusive features that make it easy to achieve perpendicular alignment. Operators find the need of eliminating the repositioning of the Catphan since all the test sections are arranged at prescribed intervals from the first module. The integral case mount allowed the phantom to be positioned in the scanner, supported off the end of

the table, eliminating table artefacts. The Catphan 600 model was made from solid-cast materials, eliminating material absorption of water and leaks associated with water bath phantoms. It was constructed from modules that fit snugly into a durable 20 cm housing. The Catphan 600, sixth generation model designed to evaluate the maximum performance potential of multi-slice CT scanners.

Figure 3.1: Picture of Catphan 500 Phantom (Men, et al., 2015)

To assess the absorbed dose through the Catphan phantom via computational simulations, we emulate the Catphan phantom as if it were undergoing actual patient scans. Through this process, we precisely calculate the radiation doses absorbed by various organs and tissues. The Catphan phantom serves as a pragmatic and efficient surrogate for the human body, providing a valuable avenue for preliminary analysis and profound insights into patient dosages.

Immersing the phantom within a virtual CT scanner environment, unlock the capability to assess the distribution of radiation doses with precision. This approach not only enhances understanding but also underscores the practicality and effectiveness of utilizing the Catphan phantom in advancing the comprehension of patient dose dynamics.

3.2.3 Statistical Tool

The Statistical Package for the Social Sciences (SPSS) version 29.0, statistical methods software was used for the analysis of the simulated results. The data obtained from the computational simulations were analysed using statistical methods. Descriptive statistics was used to summarize image quality metrics and patient dose parameters. Comparative analysis will be conducted to evaluate the differences between the additional varied BHF configurations.

3.3 Method

Figure 3.2 was the framework of the methodology used for the study. The first stage of the study entails modelling of the 64-slice CT scanner, the second stage was the simulation of the modelled CT system with BHF using various thickness of copper plate (Cu) and aluminium (Al) plate and the third stage was the assessment of the influence of BHF on image resolution and patient dose.

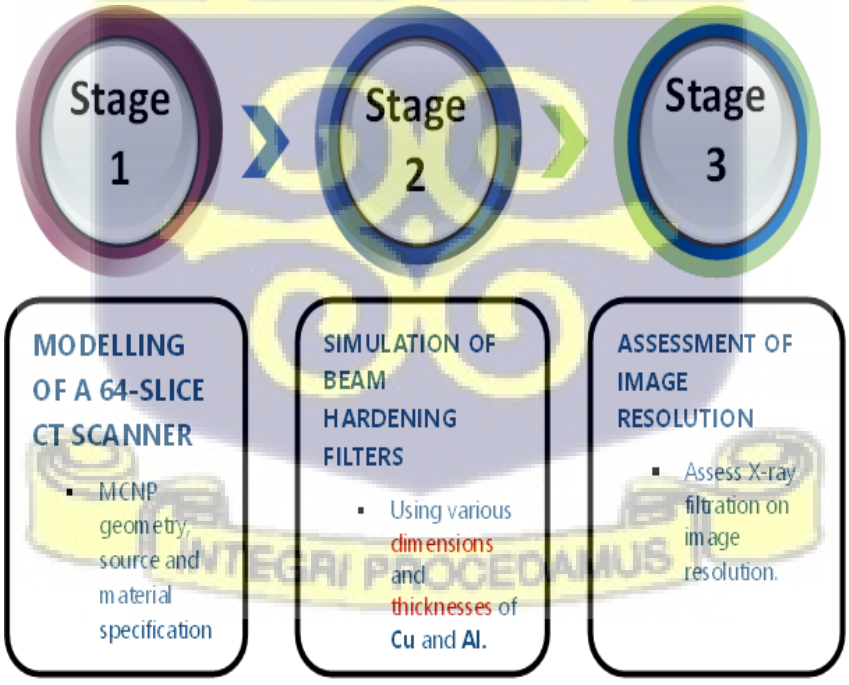

Figure 3.2: Framework of three stages of the study

3.3.1 Modelling of the 64-Slice CT Scanner

In this modelling phase, the 64-slice Philips CT scanner Brilliance iCT Family Version 4.1.10 is modelled using the Monte Carlo N-Particle (MCNP) code taking into consideration the MCNP geometry, the source, the collimator, the BHF, the Catphan 500 phantom, and the material specification as documented by the CT scan manual. For this work, two different design and modelling of the CT scanner was done. First with a Rectangularly shaped Additional Beam Hardening Filter (RABHF) and the other with a Conically shaped Additional Beam Hardening Filter (CABHF). The modelling of the CT scanner was based on the physical specifications of the Philip brand 64-slice X-ray CT scanner at University of Ghana Medical Centre (UGMC) for imaging, including the beam energy spectrum, the phantoms interaction with X-rays, filtration, detector configuration and other components of the scanner.

Figure 3.3: 64-Slice CT scanner at University of Ghana Medical Centre (UGMC), 2023.

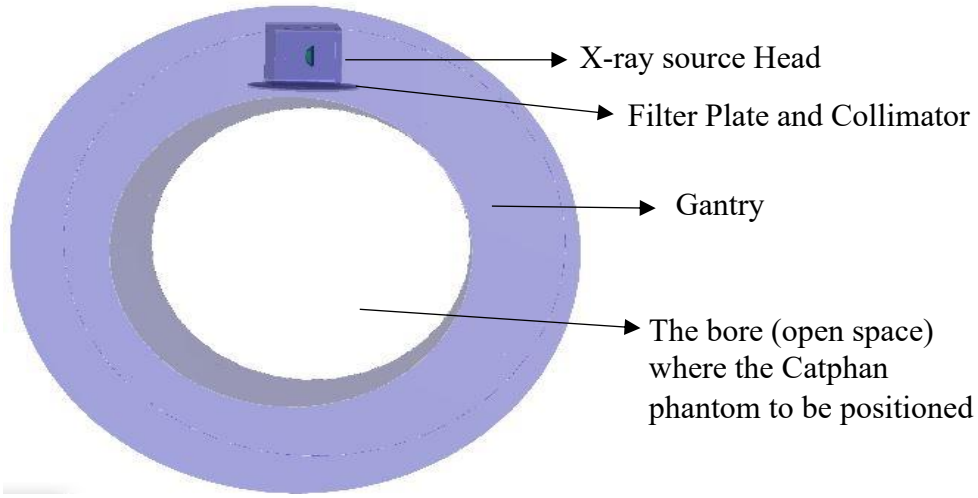

Figure 3.4: An Interface of the modelled CT scanner incorporated with the Catphan 500 phantom

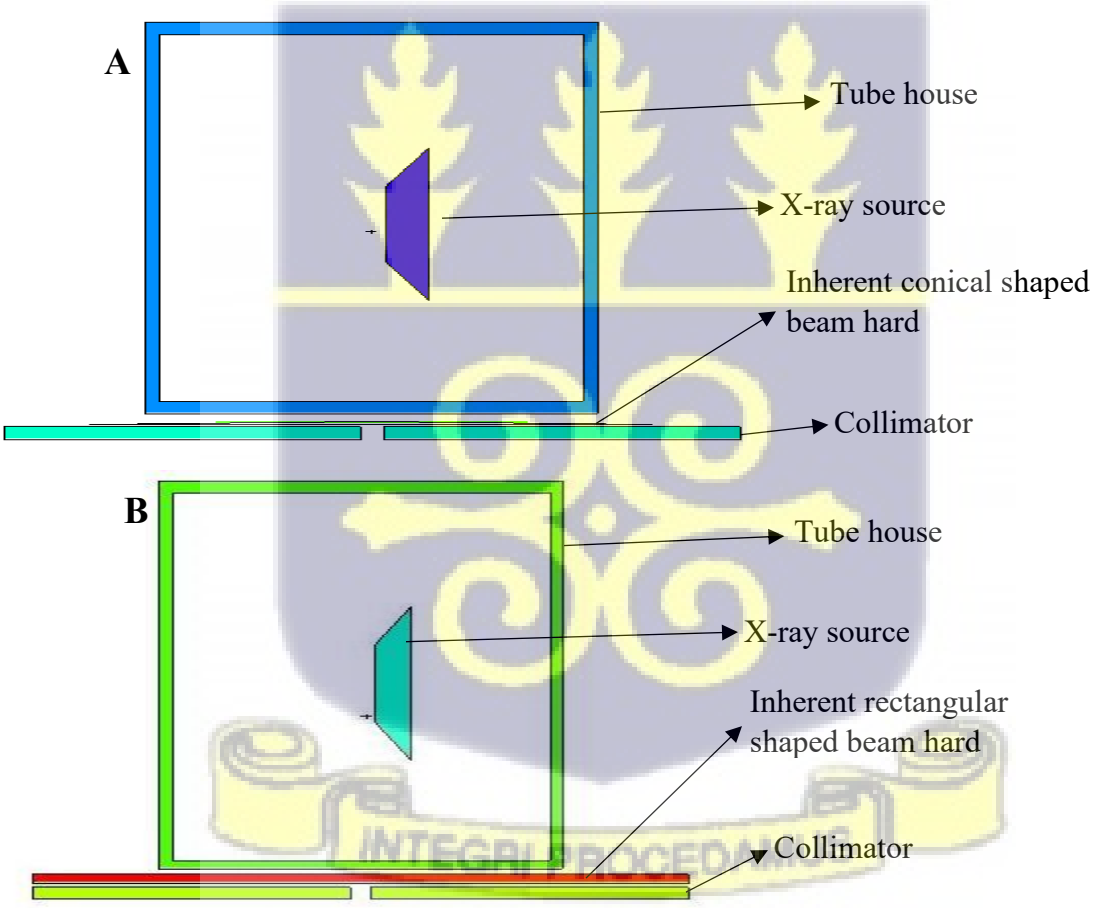

Figure 3. 5: (A) The Head of the CT scanner with conical inherent additional filter (B) the Head of the CT scanner with a rectangular inherent additional filter, illustrating the source, collimator and the inherent additional filters.

3.3.2 Modelling of the Catphan phantom embedded in 64-Slice CT Scanner

The Catphan phantom was meticulously modelled, incorporating various components such as rods, Slices, Spheres and disks, ensuring that the model accurately reflects biological tissues. This MCNP modelled Catphan phantom is integrated into the MCNP modelled 64-slice Philips CT scanner, positioning the Catphan phantom within the scanner's bore as portrayed in Figure 3.6 **A**.

The rods of the Catphan Phantom, which are cylindrical structures made from various materials, are represented as red circles of different sizes in **Figure 3.6 B**. These circles are labelled with numbers and referred to as "cells," indicating different components or regions for measurement within the model. **Figure 3.7 D** illustrates this interface. The design of these rods enables the testing of important imaging parameters, such as spatial resolution (the ability to distinguish fine details) and contrast sensitivity (the effectiveness of differentiating between various tissue densities).

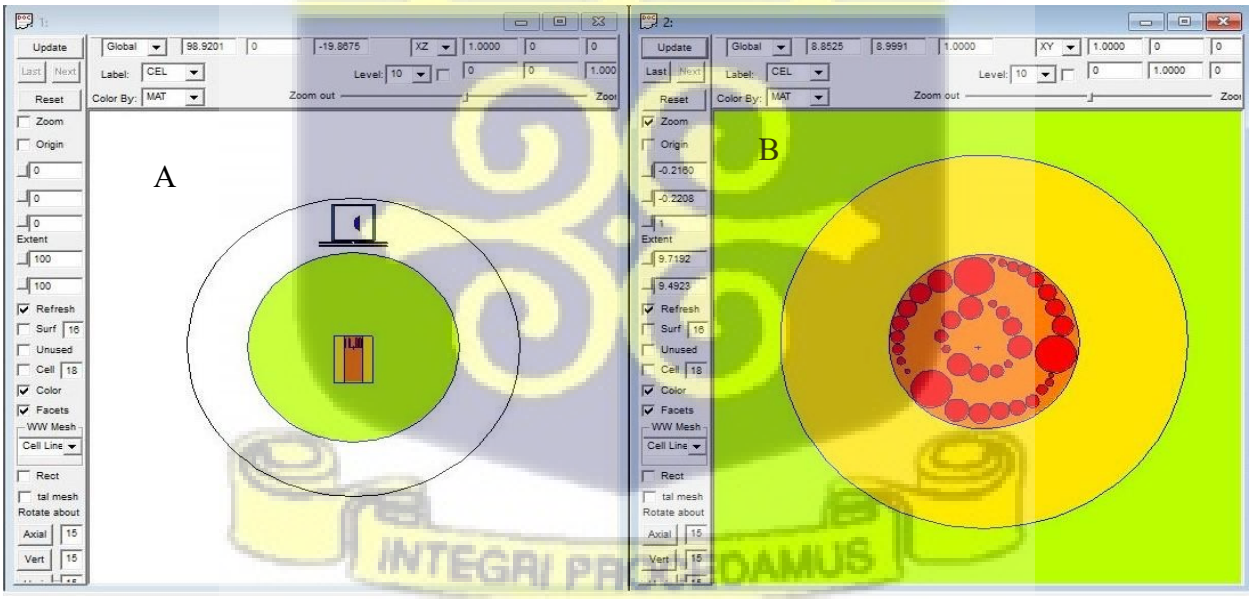

Figure 3. 6: Interface of the 2-D Visual Editor (Vis. Ed) displaying a model of the 64-slice Philips CT scanner (Brilliance iCT Family Version 4.1.10). The top left image (A) shows the Catphan 500 phantom positioned within the bore of the CT scanner, while the top right image (B) presents a cross-sectional view of the Catphan 500 phantom.

The rods herein referred to as cells contain materials with known attenuation characteristics, referred to as energy bins. These energy bins facilitate the evaluation of how well the imaging system differentiates between different tissue densities (Contrast Resolution). They also enable analysis of how varying photon energies interact with the phantom materials, enhancing overall imaging performance.

The geometrical arrangement of the Catphan phantom is meticulously calibrated to replicate clinical conditions, ensuring that the simulation results would be relevant and applicable. For each material in the phantom, the mass attenuation coefficients were utilized to understand how effectively each material interacts with X-ray photons at specific energy levels.

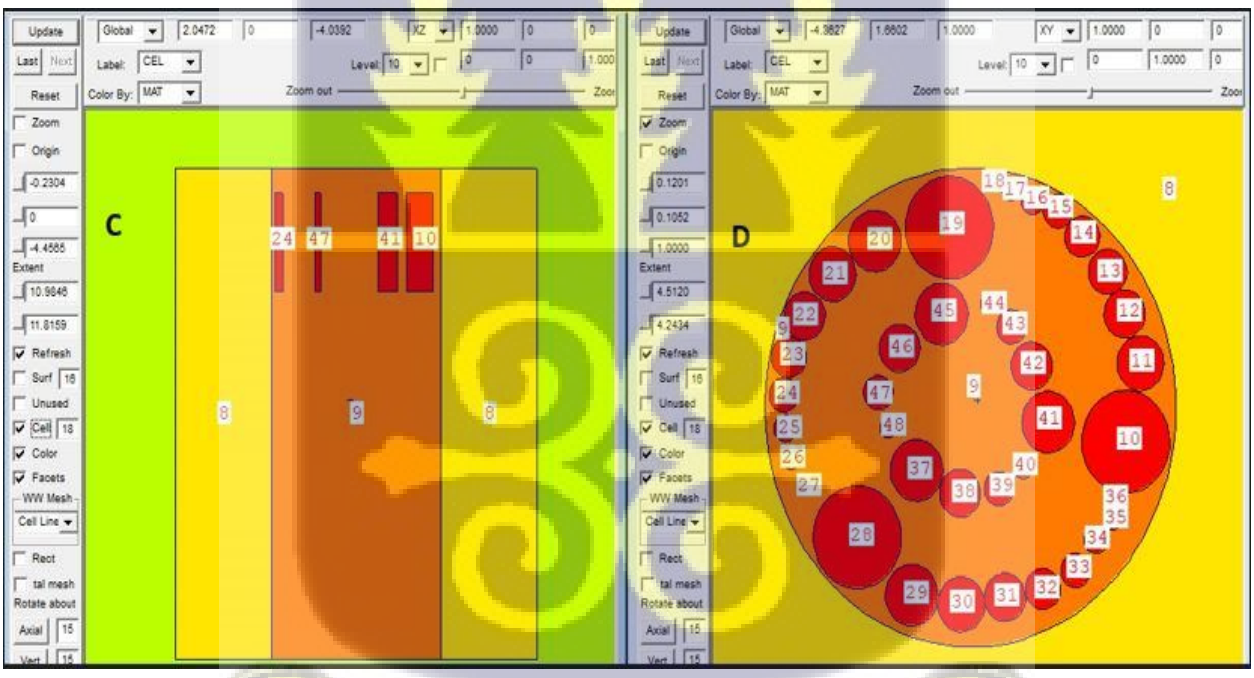

Figure 3.7 Left-hand image (C) is a cross-sectional view (in the xz plane) of the Catphan phantom and the right-hand image (D) is the cross-sectional view (in the xy plane) of the Catphan 500 phantom uniquely labelled with their associated cell numbers.

High doses at specific locations indicate areas where patients might receive excessive exposure. This information is crucial for optimizing scanning protocols and minimizing radiation dose,

especially in sensitive populations like pediatric patients. Monitoring spikes in dose at specific locations helps in quality control of CT equipment, ensuring that it operates within safe dose levels and delivers consistent imaging quality.

3.3.3 Simulation Stage

A computational simulation of the CT scanner was carried out using the modelled 64-sliced CT imaging scanner simulation software Monte Carlo N-Particle (MCNP) code. The software will simulate the interactions of X-rays with Catphan 500 phantom positioned at the bore of the CT scanner as illustrated as Figure 3. 6.

The particularly selected shaped Additional Beam Hardening Filter (either rectangularly or conically shaped) parameter was incorporated into a Monte Carlo software program, and simulated through the CT scanning process at different filter configurations under same specific simulation conditions such as X-ray beam with 120 kilovolt peaks (kVp), a tungsten target, and an anode angle typically 20°. For each simulation of CT scanning process, the Rectangularly-shaped Beam Hardening Filter was simulated first at varied thicknesses before seamlessly transitioning to the simulation of the Conically-shaped Beam Hardening Filters.

During each simulation scanning process, the Beam Hardening Filters was strategically affixed to the collimator of the MCNP-modelled CT scanner, setting the stage for a meticulously simulated exploration. This involved a dynamic adjustment of the filter thickness in successive iterations, each simulation building upon the successful completion of its predecessor. This iterative refinement process not only enhanced precision but also allowed for a comprehensive analysis of the impact of varying filter thicknesses on the CT scan performance, ultimately contributing to a more nuanced understanding of the interplay between the filter configuration and simulation outcomes.

The software generated and calculated the corresponding energy emitted. Which was subsequently used to determine the virtual CT images quality.

This simulation provided valuable information about the distribution of radiation in the patient and how it interacted with the filter.

3.3.4 Assessment of Image and Patient Dose

The CT image matrices, simulated through advanced computational techniques, undergo thorough evaluation to precisely determine both patient dose and image quality. Employing the results derived from the simulation, we accurately estimate dose measurements, ensuring a comprehensive understanding of the impact of BHF on patients' radiation exposure. The in-depth analysis of radiation absorption by the Catphan 500 phantom, a faithful mimic of human body tissues, serves as a crucial tool in evaluating the influence of BHF. This valuable insight guides the optimization of CT imaging protocols, strategically aimed at minimizing radiation doses while upholding diagnostic accuracy. Our approach not only enhances patient safety but also underscores our commitment to advancing medical imaging practices through thoughtful and effective optimization strategies.

Following the acquisition of patient dose data, a meticulous analysis employing deviation analysis techniques was undertaken. The results obtained from this deviation analysis are subjected to a quantitative assessment, offering a nuanced understanding of the impact of diverse BHF configurations on both image resolution and diagnostic accuracy. Specifically, the beam filter demonstrating the highest sum of absolute deviations from the mean dose was identified as the optimal filter for achieving superior image quality. This rigorous process forms the basis for selecting the most effective filter thickness, ensuring an informed decision that prioritizes optimally balance patient dose and image quality while maintaining precision in diagnostic

outcomes. In this phase of optimization, the determination of the optimal filter thickness is guided by deviation analysis. This evaluation was engaged by calculating the absolute of the deviation of each measured patient dose distribution from the mean dose to achieve a finely tuned equilibrium.

3.4 Data Collection

The simulation and optimization results were analysed and presented in graphical and tabular forms. The data collected included the radiation dose to the phantom and image quality metrics each filter thickness simulated. The optimal filter thickness identified through the optimization algorithm was reported.

3.5. Statistical Analysis

The data collected from the simulation and optimization phases of the research study was analysed using Statistical Package for the Social Sciences (SPSS) statistical methods software. The statistical analysis helped to determine the effectiveness of different shapes and thicknesses of the copper and aluminium used as BHF material. The collected data was analysed to determine the significance of any observed differences in image quality and patient dose between the different filter thicknesses simulated. A *p*-value of less than 0.05 was considered statistically significant.

3.6 Validation

The results of the computational study were validated by comparing to known reference values obtained using a physical phantom. For this work, the reference data was the experimental research study of Ay, et al. (2013). By comparing the simulated results with actual imaging data, the study validates the findings and assess the translational potential of the research.

CHAPTER FOUR

RESULTS AND DISCUSSION

This chapter presents the results obtained from the simulation of the modelled Catphan phantom placed in a CT scanner for CT dose measurements when beam filters of different thickness were varied. The results are further analyzed and discussed in this section.

4.1 Results of Validation

Figure 4.1 shows of the design of a two-dimensional (2-D) image of the MCNP modelled CT scanner incorporated with the Spherical Head phantom (SHP) a replica kind of the CTDI (Computed Tomography Dose Index) phantom.

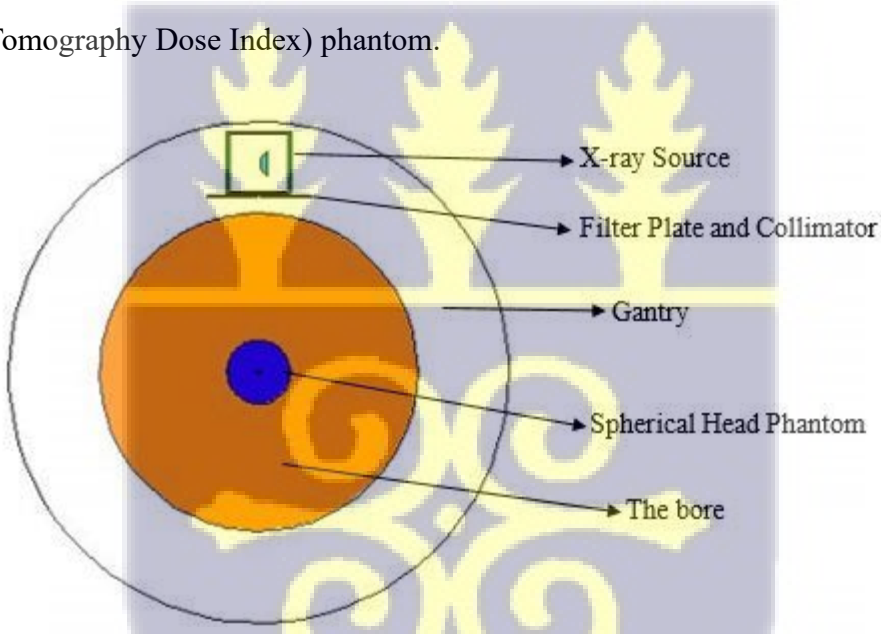

Figure 4. 1: The MCNP modelled CT scanner incorporated with the Spherical Head Phantom (SHP).

The MCNP modelled CT scanner incorporated with the SHP (the CTDI phantom) was simulated to validate its replicability and reliability to the Philips CT scanner Brilliance iCT Family Version 4.1.10 brand. Table 4.1 provides the result of the information on the validation of the MCNP

modeled CT scanner. This table depicts the radiation dose distribution at different point on the 16 cm diameter of the SHP when placed in the center of the Gantry opening, on the head holder.

Table 4.1: Percentage Deviation from actual dose distribution

Location	Dose distributed at different point on an infant head /mGy	MCNP Dose distribution to the phantom /mGy	Deviation from manual dose distribution /mGy	Percentage deviation (%)
1. 12 o'clock position	36.6	35.9	0.7	1.91
2. 6 o'clock position	35.1	34.4	0.7	1.91
3. Center of the phantom	32.2	32.2	0.0	0.0
4. 9 o'clock position	35.6	34.9	1.0	1.97
5. 3 o'clock position	35.3	34.7	0.6	1.70

Table 4.1 clearly showed the dose deviation and the percentage deviation of the MCNP modelled CT scanner from the dose distribution documented in the manual of the Philip brand CT scanner. From Table 4.1 on the dose distribution, it was observed that at the 12 o'clock position, the CT scanner had the maximum dose of 36.6 mGy and 35.9 mGy by the MCNP modelled CT scanner. Again, both CT scanners had the same minimum dose of 32.2 mGy at the center of the SHP. At the 6 o'clock position of SHP the dose distributed was 35.1 while the MCNP CT scanner measured a drop dose delivered as 34.4 mGy, which was a decrease of dose delivered of 0.7 mGy deviation from the CT scanner. And at the 9 o'clock position the dose delivered by the referenced CT scanner was 35.6 mGy while that the MCNP CT scanner was 34.9 mGy and the deviation was -1.0 mGy. While these deviations indicate some differences between the manual and MCNP calculations, they are within an acceptable range since dose distribution analysis show deviation range less than

± 2 mGy or 2 % generally dose uniformity test ensure that the dose deviation should not exceed a percentage of at least 5 % due to patient safety (Philips, 2021).

Considering the overall trend of the data, with small deviations and percentage deviations, it can be concluded that the MCNP Code software is generally acceptable for modelling and designing the Philip brand CT scanner in terms of dose distribution.

4.1.1 Aluminium filter simulated results

Computationally the Rectangularly-shaped Additional Aluminium Beam Hardening Filter (RAABHF) was attached to the collimator of the MCNP modelled CT scan and simulated successively at different thicknesses. Figure 4.2 shows virtually the position of the rectangular shaped filters when fixed computationally as part of the X-ray head for simulation.

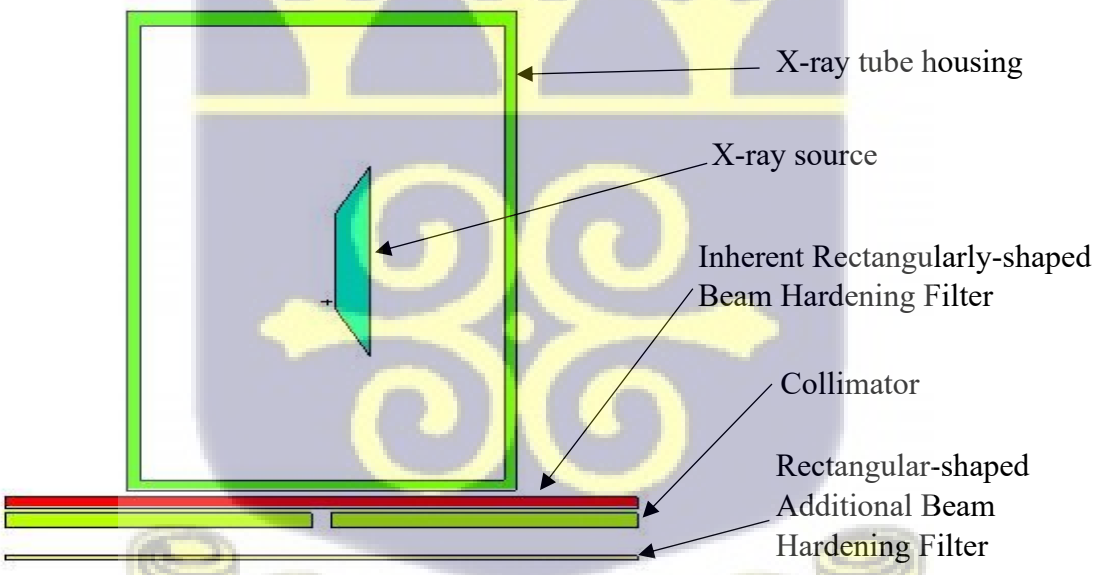

Figure 4.2: The modelled CT scan X-ray tube head with rectangularly shaped filter

And Figure 4.3 depicts virtually the outlook of the MCNP designed and modelled CT scan incorporated with the Catphan phantom in the bore and the rectangularly-shaped beam Hardening Filter attached to the collimator to form part of the X-ray head.

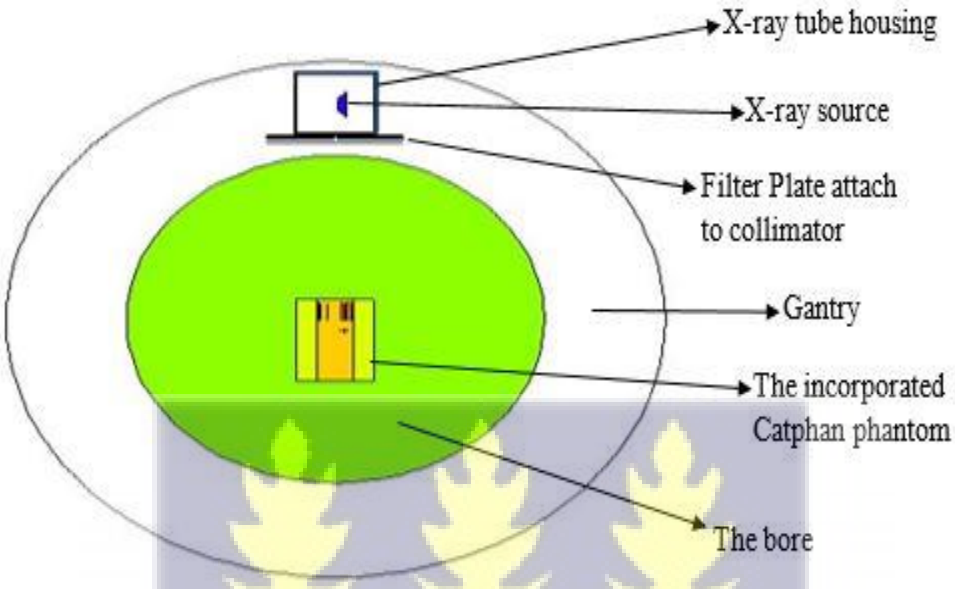

Figure 4.3: The MCNP modelled CT scanner incorporated with the Catphan phantom

Table 4.3 of Appendix F present a comprehensive output result of the radiation dose exposed to different rods, (from cell 10 to cell 48) of the digital Catphan phantom which is situated computationally within the bore of the MCNP modelled CT scanner. The output data was measurements specifically noted when the varied thicknesses of the Rectangular-shaped Additional Aluminum Beam Hardening Filter (RAABHF) was computationally attached to the collimator of the MCNP modelled CT scan and simulated successively.

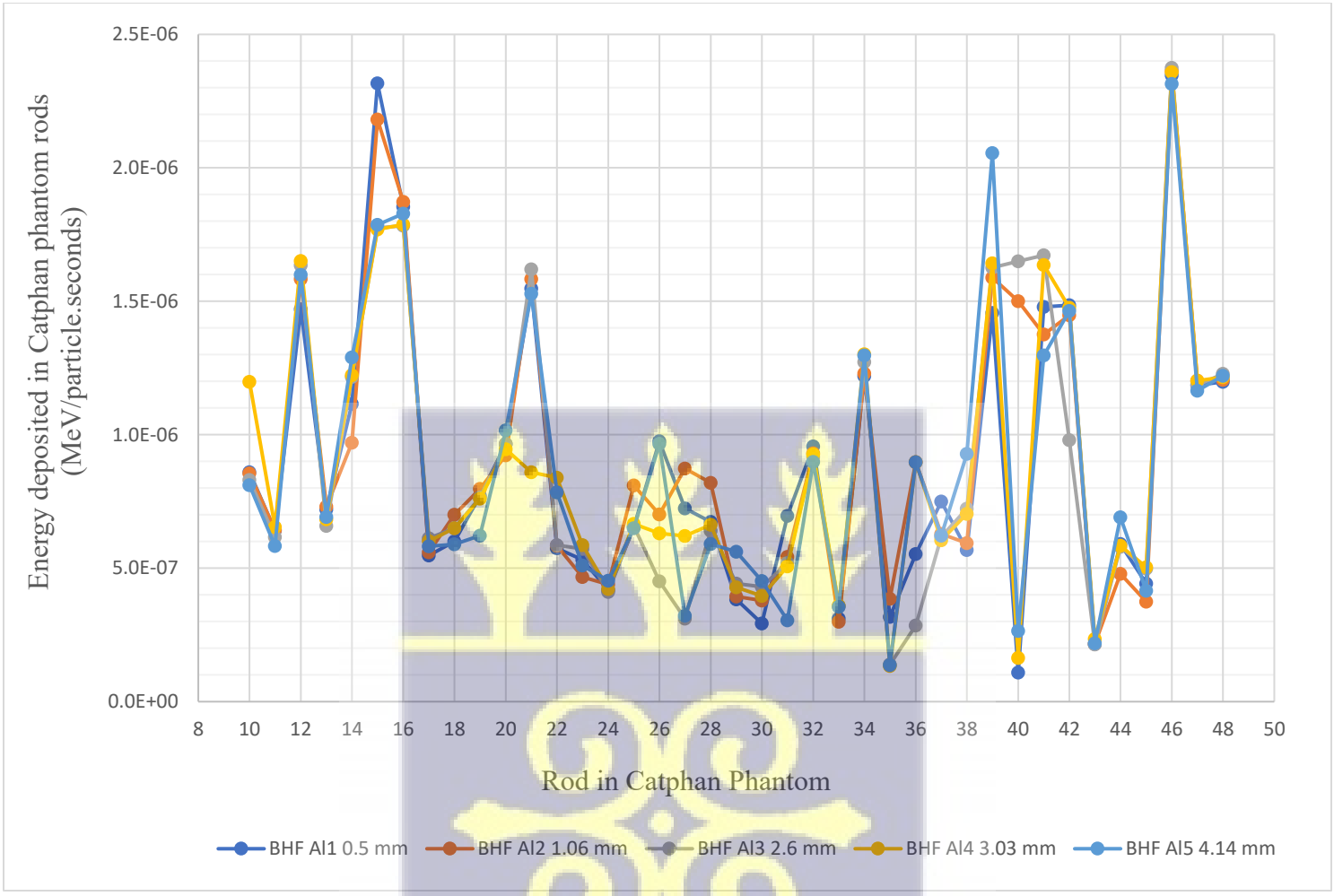

Figure 4. 4: Graphical representation of dose distribution of different thicknesses of Rectangular-shaped Aluminium filters

Figure 4.4 is a graphical demonstration of the output results of Table 4.3 of Appendix F, when the Rectangular-shaped Additional Aluminum Beam Hardening Filter (RAABHF) was used under the influence of same specific simulation conditions such as X-ray beam with 120 kilovolt peaks (kVp), a tungsten target, and an anode angle typically 20°. The chart compares the measured radiation doses to the rods of the Catphan phantom labelled cells 10 to 48 against the filter thickness, highlighting the varying doses based on the aluminum beam hardening filter's thickness.

Considering the overall trend of the data, suggests that thicker filters (e.g., 4.14 mm, 3.03 mm) tend to exhibit slightly higher radiation doses at peak points compared to thinner filters. The highest dose of 2.37485E-06 MeV/particle.second was received by cell 46 of the phantom, when the thickness of the RAABHF was 2.6 mm. The spike tells of the radiation dose received at that specific point of the phantom measured in MeV/particle.second. This actually depicts the intensity of radiation interaction with the specific rod within the modelled Catphan phantom incorporated to the MCNP modelled CT scanner. Thicker filters increase the radiation dose received by the phantom, which might enhance image quality but could lead to higher patient exposure. And the lowest dose received generally was 1.09E-07 MeV/particle.second by cell 40 at a beam filter thickness of 0.53 mm. This low radiation dose was received because the filter was thinner, it means thinner filters reduce dose variability, potentially reducing exposure but possibly affecting image contrast.

Specifically, as the filter thickness increases from 0.53 mm to 2.60 mm, there was a notable trend of decreasing energy dosage exposure across most rods (from Cells 10 to 47) of the phantom. This suggested that thicker beam hardening filters will filter out more radiation with lower energies. Therefore, radiation with lower penetrative energy are exposed to the phantom cells making the

cells of the phantom to absorb more radiation doses, under same conditions, indicating a potential correlation between filter thickness and radiation attenuation.

With an additional rectangular-shaped filter thickness of 1.06 mm, the maximum dose decreases to 5.6647E-06 MeV/particle.second, as observed in cell 18. Meanwhile, the minimum dose decreases to 1.5513E-08 MeV/particle.second in cell 36. The thicker filter attenuates the X-ray beam further, leading to reduced doses across the distribution.

Stepping up to a thickness of 2.6 mm, the maximum dose remained similar at 5.6305E-06 MeV/particle.second in cell 18. However, the minimum dose further decreased to 4.9323E-08 MeV/particle.second in cell 36. The increased filter thickness continued to modify the energy distribution, resulting in a reduced dose. At 3.03 mm thickness of RAABHF, the maximum dose remains relatively consistent at 5.6386E-06 MeV/particle.second in cell 18. The minimum dose stayed the same as well, at 1.5513E-08 MeV/particle.second in cell 36. The dose distribution maintains a similar pattern with minimal changes. Finally, with a thickness of 4.14 mm, the highest energy reaches cell 9, resulting in the highest dose. The lowest energy, and correspondingly the lowest dose, was received by cell 36.

It could be deduced that as the thickness of the aluminum beam hardening filters increased, the dose distribution was affected. Thicker filters resulted to greater attenuation of the X-ray beam, leading to a decrease in the maximum and minimum doses received by the objects being scanned. This demonstrated how the thickness of the aluminum filters plays a crucial role in shaping the dose distribution in CT scanners.

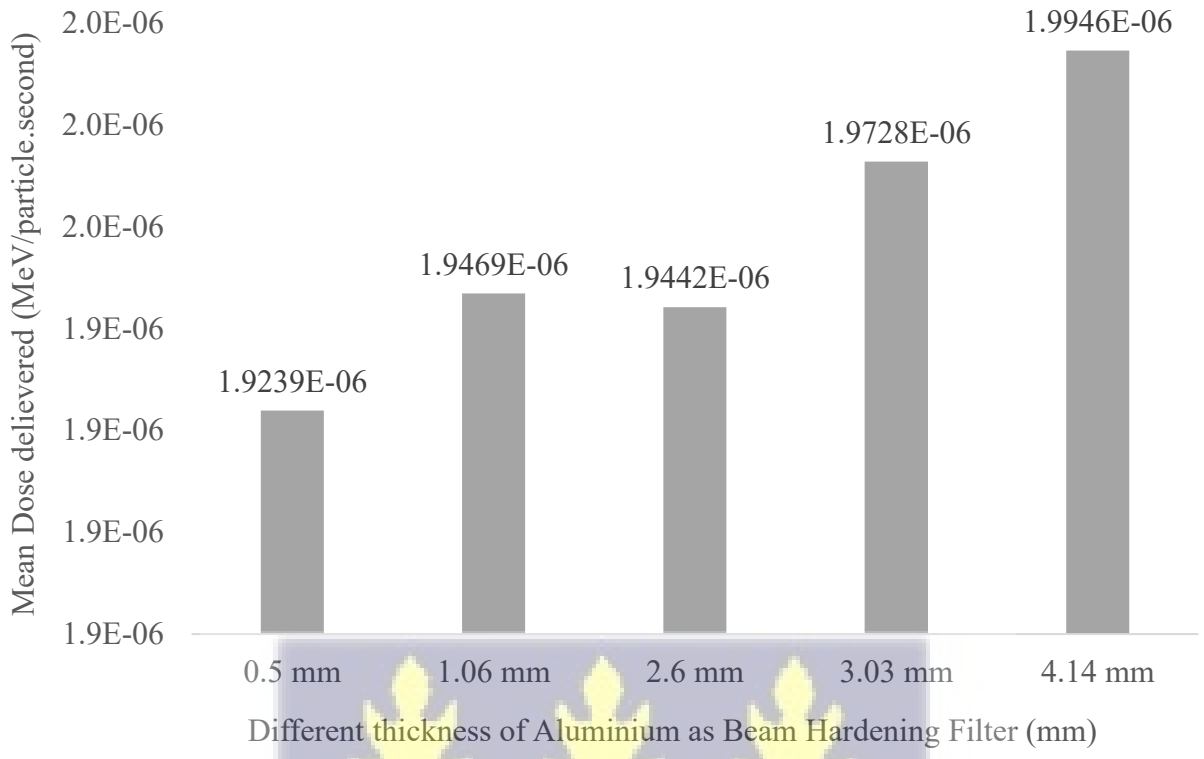

Figure 4. 5: Graphical representation of the mean dose distribution to the Catphan Phantom with varied thickness of Aluminium beam filters.

Figure 4.5 graphical representation was considered for the output result of the mean energy distribution at various thicknesses. By comparative analysis, the maximum mean energy dose of 1.9946E-06 MeV/particle.second was observed absorbed by the Catphan phantom when the RAABHF had a thickness of 4.14 mm whiles the lowest mean energy dose of 1.9239E-06 MeV/particle.second was noted as beam filter thickness of 0.5 mm was inputted. At a thickness of 1.06 mm, 2.6 mm and 3.03 mm the mean energy dose distribution was 1.9469E-06 MeV/particle.second, 1.9442E-06 MeV/particle.second and 1.9728E-06 MeV/particle.second respectively. This suggested that the filter thickness influenced the mean dose distribution, with slight variations observed between the different thicknesses.

Subsequently after completion of the simulation of the rectangular shaped filters, the modelled conically-shaped additional Aluminium Beam Hardening Filter is simulated to ascertain essentially by evaluating its hypothesised advantages over rectangular filters, improving image quality and reducing radiation dose while allowing for efficient optimization and risk management in the design process. The first 0.15 mm Conically-shaped additional Aluminum Beam Hardening Filter (CAABHF) thickness was affixed to the MCNP modelled CT scanner and simulated. Figure 4.6 showed how the X-rays head looked when the conical-shaped beam filter was fixed and Figure 4.7 depicts virtually the position of the X-ray head as part of the MCNP modelled CT scan.

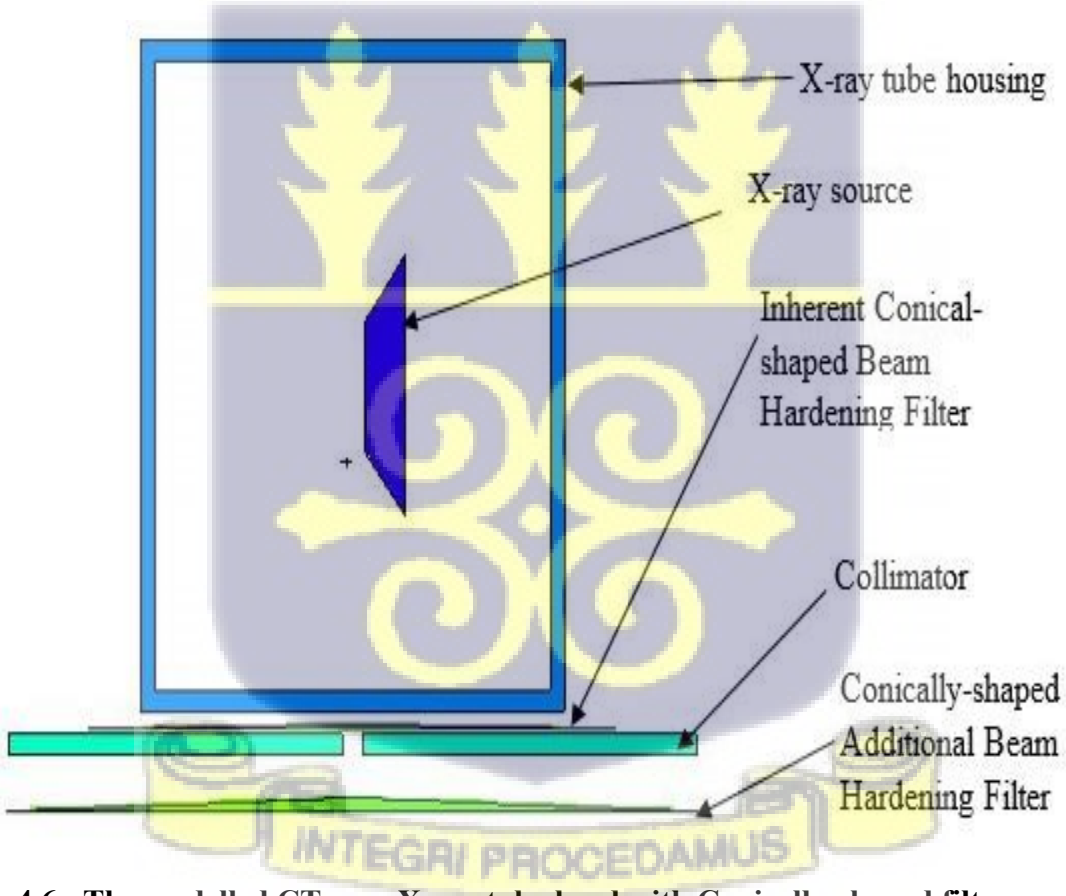

Figure 4.6: The modelled CT scan X-ray tube head with Conically-shaped filter

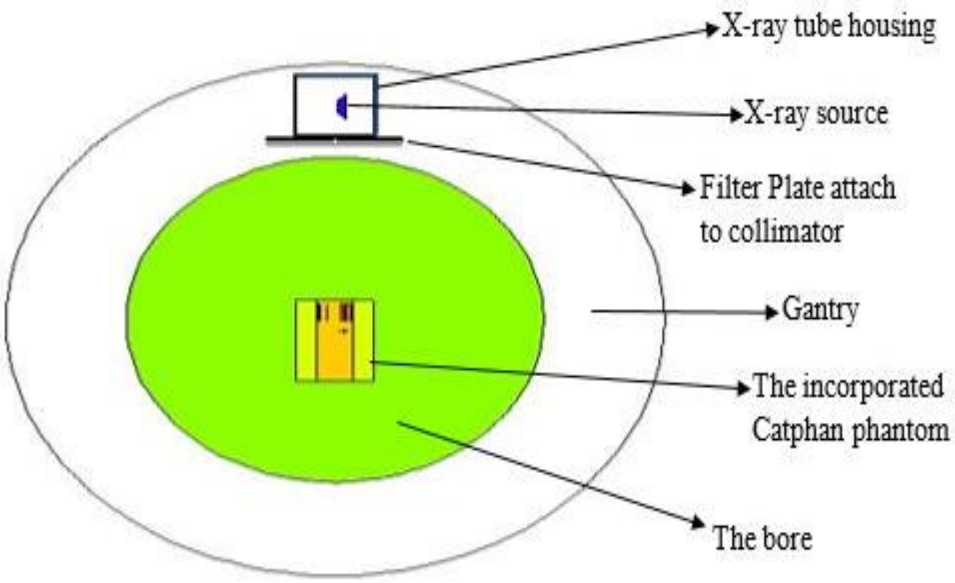

Figure 4.7: The MCNP modelled CT scanner incorporated with the Catphan phantom

After simulation, the output data result was assembled and extrapolated graphically as Figure 4.8 Generally, the trend of the output data results showed that, the thickness of the conically-shaped Aluminium filter increases the energy exposed to the cell of the Catphan phantom mostly decreases. This suggests that the thicker the filters, the dose of radiation deposited across most cell of the Catphan phantom decreases. Extrapolation of Figure 4.8, the maximum energy of 1.6071E-06 MeV/particle.second was received at a thickness of 3.08 mm by cell 18 and a minimum dose of 8.7925E-08 MeV/particle.second was received by cell 17 when the conical-shaped beam filter had a thickness of 2.60 mm.

At 0.53 mm thickness of the CAABHF, the maximum dose received was 1.5574e-06 MeV/particle.second and the minimum energy emitted after filtration was 1.2906E-07 MeV/particle.second, which were deposited at cell 18 and cell 38 respectively and stepping up the thickness to 1.06 mm, the maximum dose 1.5261E-06 MeV/particle.second and at cell. 17 the minimum dose deposited was 9.9337E-08 MeV/particle.second.

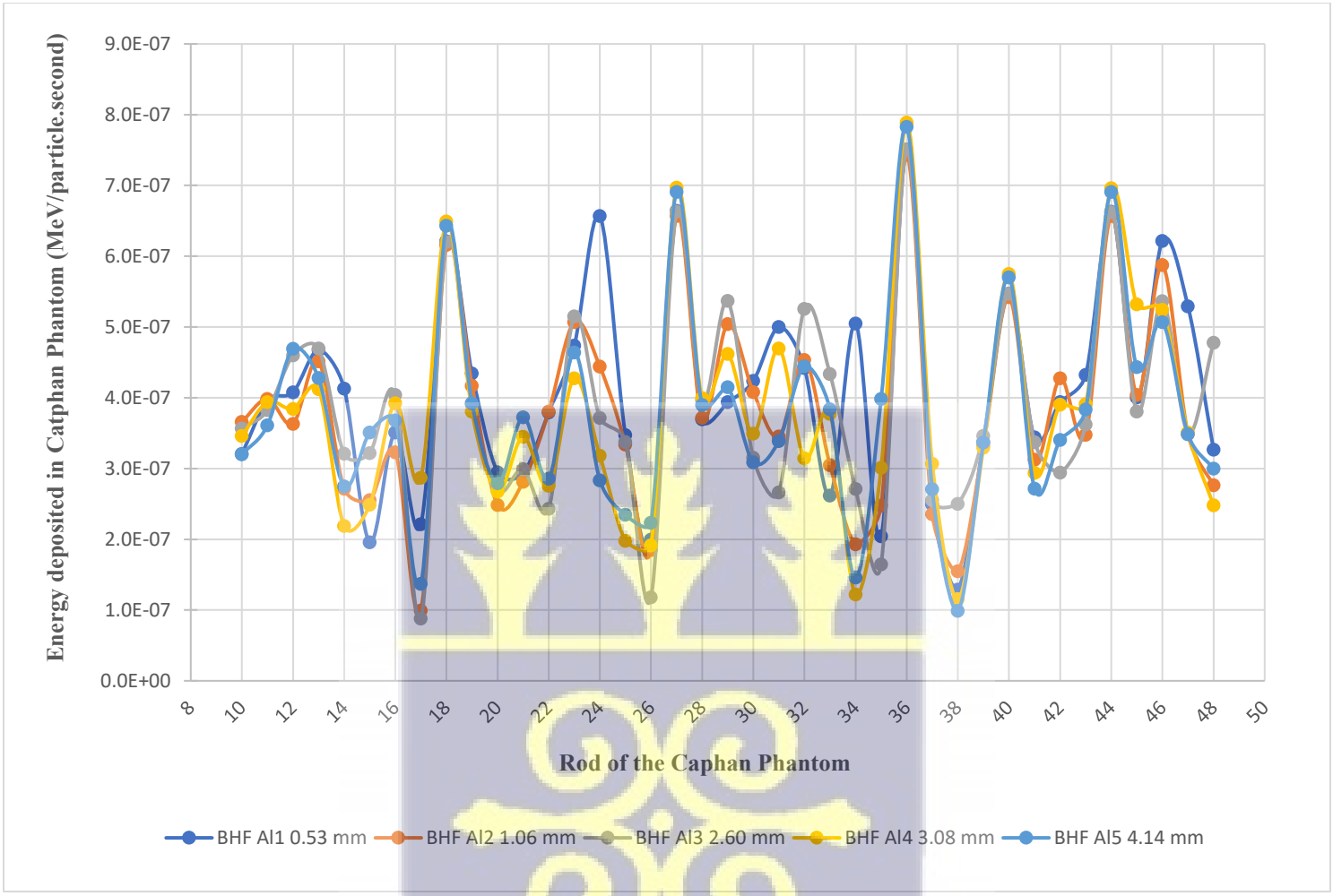

Figure 4.8: Graphical representation of dose distribution of different thicknesses of Aluminium filters when the filter is conically-shaped

When the CAABHF thickness was 2.60 mm the maximum dose was 1.5355E-06 MeV/particle.second absorb by cell 18 while the minimum was 8.7925E-08 MeV/particle.second received by cell 17.

At a filter thickness of 3.08 mm, the dose rises drastically to a maximum dose of 1.6071E-07 MeV/particle.second at cell 18 and the dose drops drastically to a minimum dose of 1.1547E-07 MeV/particle.second at cell 38. And lastly an increase of the CAABHF thickness to 4.14 mm, the dose rises to a maximum dose of 1.5919E-07 MeV/particle.second and the minimum dose was 9.9080E-08 MeV/particle.second.

Based on the generated data, the mean energy exposed to the rods for each thickness of the Conically-shaped Additional Aluminum Beam Filter was calculated and illustrated graphically as Figure 4.9.

Figure 4.9: Chart of the mean dose distribution to the varied thickness of the Conically-shaped Additional Aluminium beam filters.

When the thickness of the conically-shaped beam filters was 0.53 mm, the Rods of the Catphan received 4.05704E-07 MeV/particle.second as the highest energy while at thickness 1.06 mm the cells of the Catphan Phantom received mean dose distribution of 3.84769E-07 MeV/particle.second when the filter was CAABHF. And at a thickness of 2.06 mm, 3.08 mm and 4-14 mm, the corresponding mean energy dose were 3.9977 MeV/particle.second, 3.7839E-07 MeV/particle.second, 3.789E-07 MeV/particle.second respectively.

Further studies of the mean dose distribution to both the rectangularly shaped Aluminium beam filters and the conically shaped Aluminium beam filters was graphically represented below.

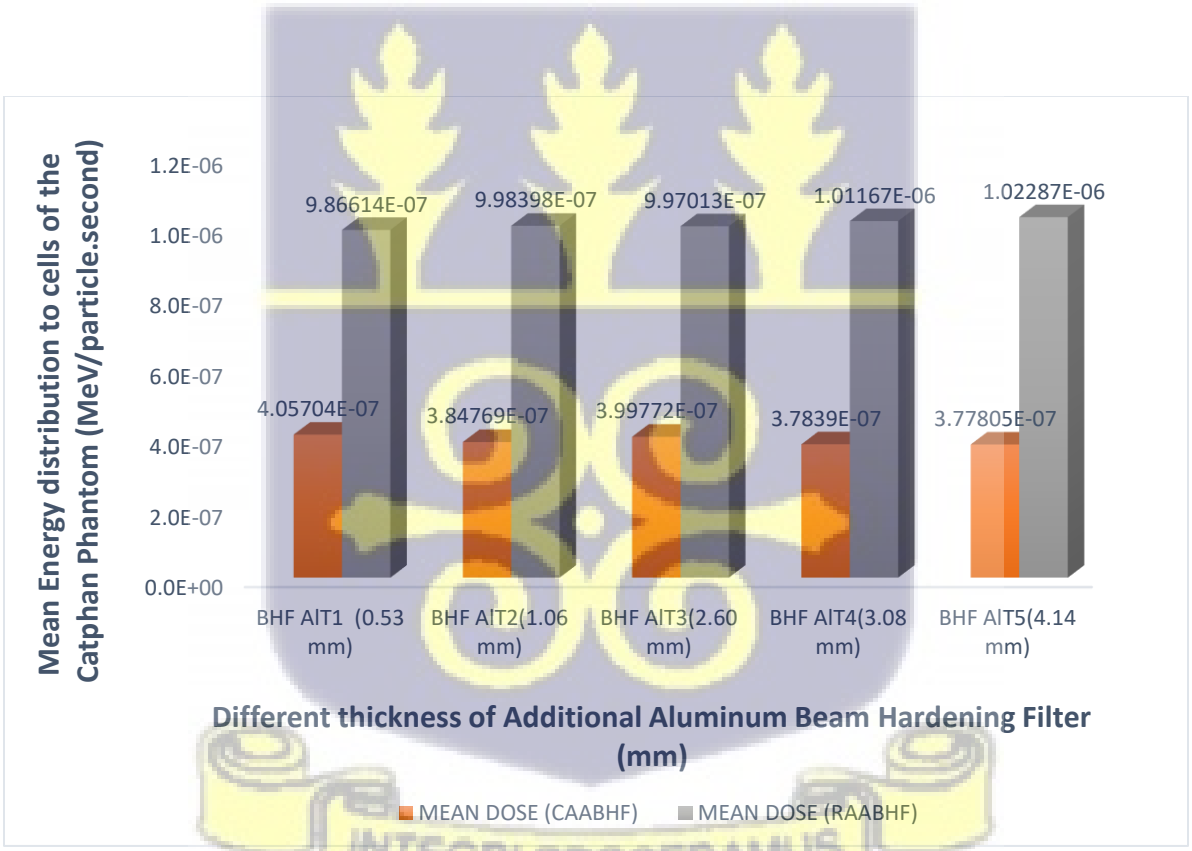

Figure 4. 10: Graphical representation of the comparison of the mean dose distribution between the Rectangular-shaped Aluminium beam filter and the Conically-shaped Additional Aluminium beam filters

Figure 4.10 indicates similar wide reduction trend and magnitude in the dose comparison across the thicknesses of the beam filters from 0.53 mm to 4.14 mm. Again, empirical extrapolation of the mean dose comparison depicts that the CAABHF is averagely 6.14025E-07 MeV/particle.second less than the RAABHF. The average percentage deviation in dose comparison between the conical-shaped aluminum additional beam hardening filter and the rectangular-shaped filter is 61.02%. This suggests generally that the CAABHF is better in dose reduction than the RAABHF.

4.1.2 Copper filter simulated results

Moreover, alternatively the copper was used as beam filter material but shaped either rectangularly or conically. After simulation, the output data results of Table 4.5 (Appendix I) was noted and enumerated graphically as Figure 4.11.

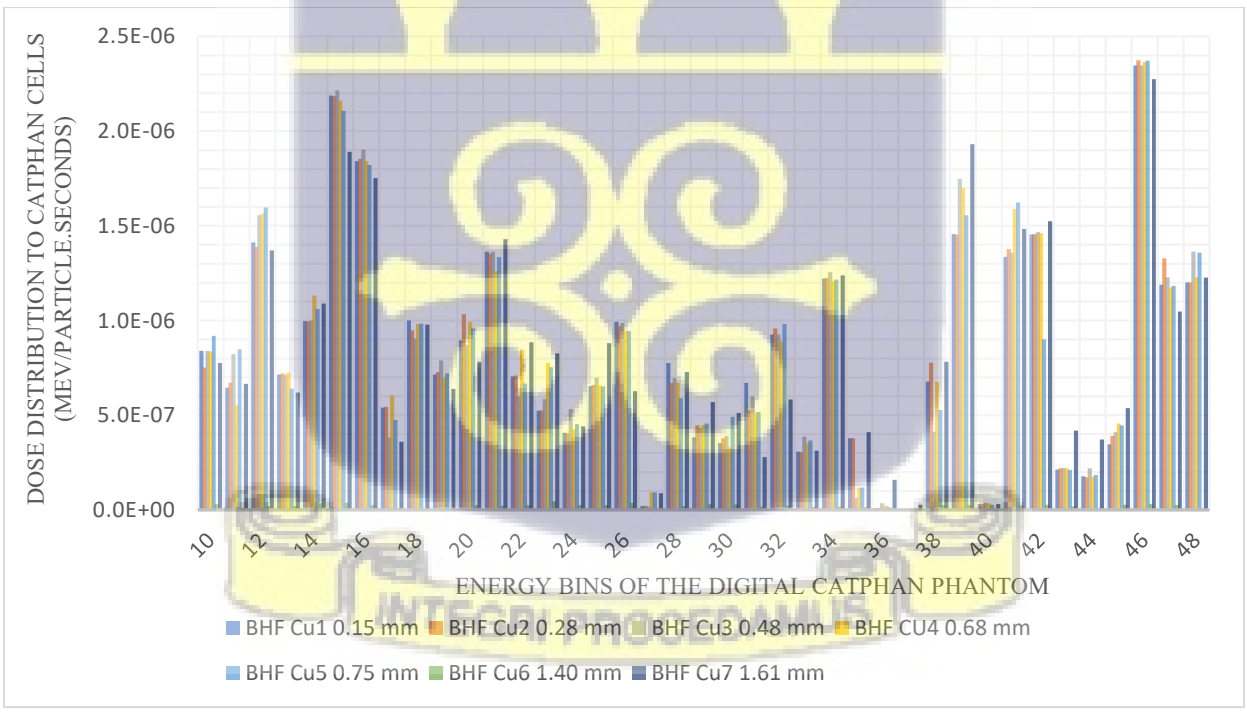

Figure 4. 11: Graphical representation of energy dose distribution to Catphan Phantom with the Rectangularly-shaped Copper Beam Hardening Filter (RACBHF)

The energy dose was distributed from cells 10 to 48 of the virtual Catphan 500 phantom when the thickness of the Copper material used as additional beam hardening filter was varied to different thicknesses. And the dose received by the rods of the phantom measured varied progressively when different thickness of copper material used as rectangular-shaped additional beam hardening filter.

The dose values fluctuate across the energy bins, indicating varying absorption and scattering effects across different regions of the phantom. At a thickness of 1.61 mm, a maximum energy of 5.614E-06 MeV/particle.second was measured with the energy bin labelled cell 18 whiles at the thickness of 0.15 mm, the minimum dose was measured as 9.569E-09 MeV/particle.second at cell 36 of the energy bins of the digital phantom. The mean energy of the energies deposited at the cell of the Catphan phantom was evaluated and graphically extrapolated.

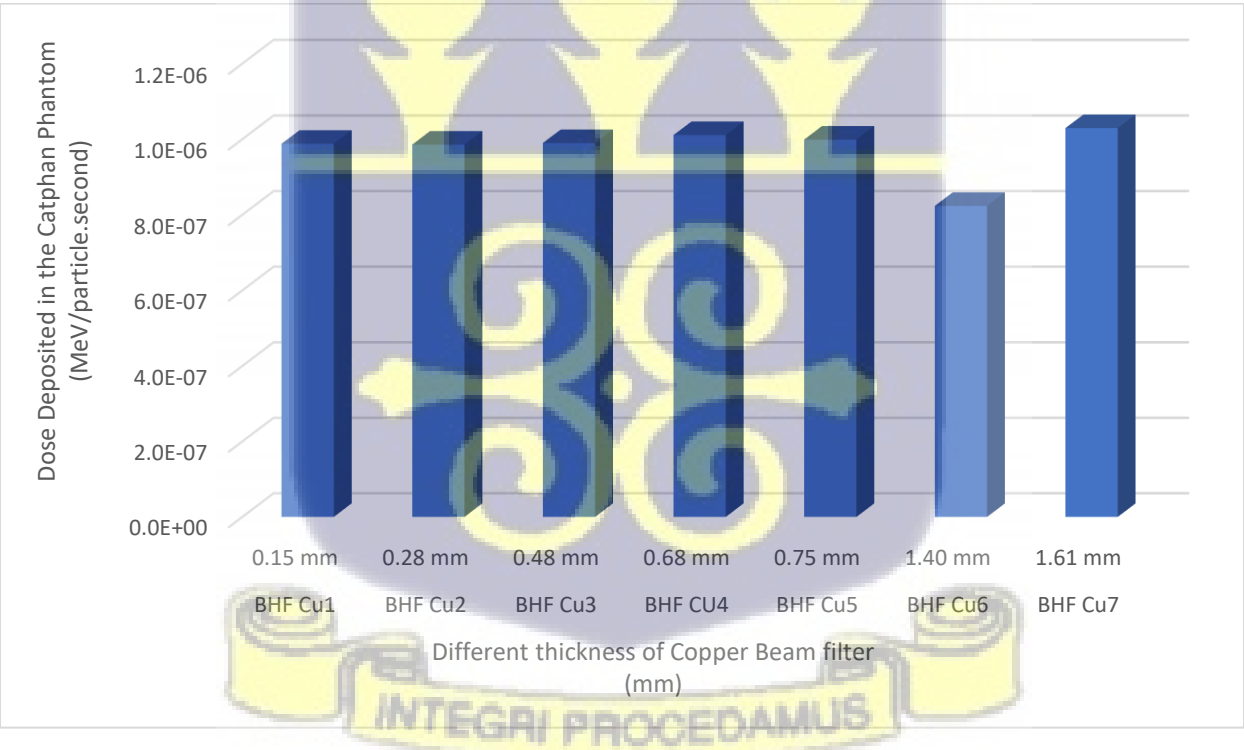

Figure 4. 12: Graphical representation of mean energy dose distribution with change of the thickness of the additional copper beam hardening filter.

Figure 4.12 showed that the graphical representation of the mean radiation dose distributed to the rods of the Catphan phantom when the thickness of the additional copper beam filters was varied. The graph showed close energy variations except the drastic drop in dose distribution when the thickness of copper material was 1.40 mm with corresponding dose of 8.2334E-07 MeV/particle.second was deposited at the energy bin labelled cell 36, suggesting significant attenuation of lower-energy X-rays. This filter may result in inadequate exposure for reliable diagnostic imaging. However, the maximum mean dose distribution was 1.02928E-06 MeV/particle.second at a thickness of 1.61 mm of additional copper filter. which may indicate an artifact or a change in the beam energy spectrum. And the minimum mean energy distribution was 8.2334E-07 MeV/particle.second when the additional thickness of the rectangularly shaped copper filter was 1.40 mm.

From the results illustrated by the graph, it may clearly indicate that thinner filters (up to 0.75 mm) ensure a high and consistent radiation dose, which is essential for producing quality images. Thicker filters should be avoided due to their significant attenuation effects, which compromise image quality.

When the conically-shaped filter of the copper material was studied, Figure 4.13 was the graphical representation of the simulated output results. The graphical representation of figure 4.8, showed similar trend as virtually depicted of Figure 4.13. The highest energy of 1.2763E-06 MeV/particle.second was detected at cell 18 and the minimum radiation energy of 7.4330E-08 MeV/particle.second was detected at cell 48. The radiation energy distribution was noted with the highest number of peak values when the conically shaped copper filter was of the thickness 0.48 mm. Generally, the energy distribution patterned a trend that showed increased filter thickness with decrease in radiation dose distribution to the cells of the Catphan phantom.

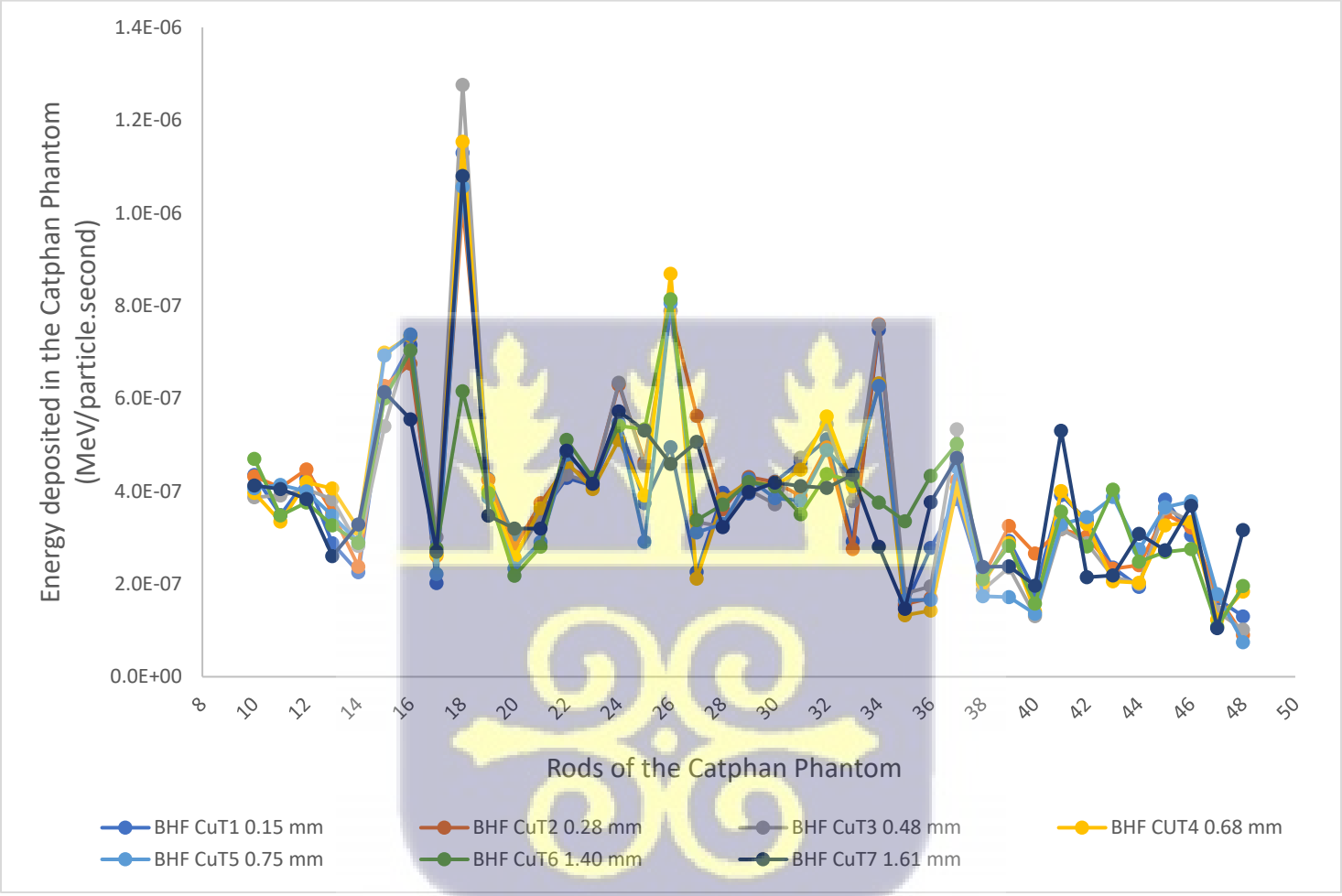

Figure 4. 13: Representation of the output data when filter was conically-shaped copper.

The mean dose distribution evaluated showed a trend of energy dose distribution as sinusoidal in shape. This was graphically represented as Figure 4.13, the least distribution height of the bar chart valued 8.1017E-07 Mev/particle.second at a Filter thickness of 0.15 mm while the maximum distribution valued 8.5161E-07 MeV/particle.second when the filter thickness was 0.28 mm.

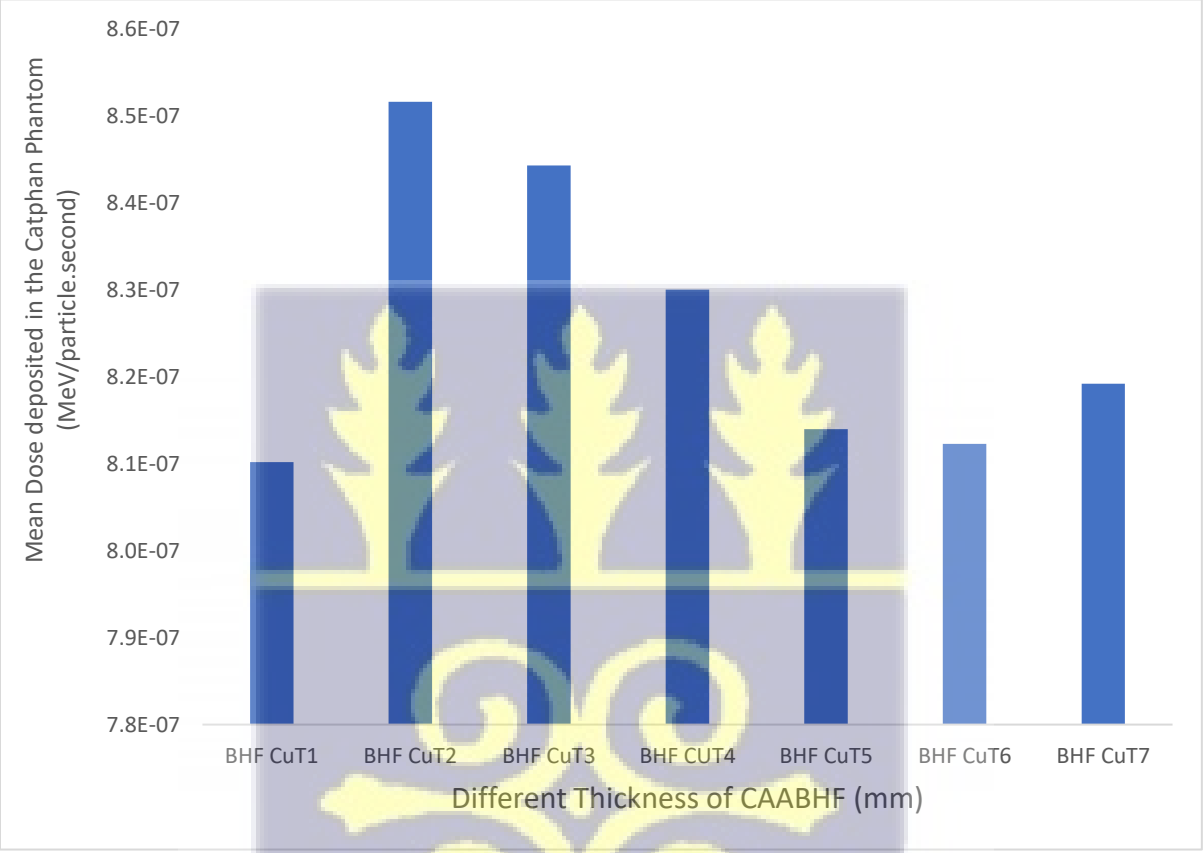

Figure 4. 14: Representation of the mean dose across the cells of the Catphan phantom when the filter material was copper and was conically shaped

The figure representation, figure 4.14 presents the mean dose deposited in a Catphan phantom considering different thicknesses of copper beam hardening filters (BHF). The graph displays mean doses in the range of approximately 8.1017E-07 MeV/particle.second to 8.5161E-07 MeV/particle.second.

The beam hardening filter labelled BHF CuT1 of thickness 0.15 mm deposited the lowest mean dose of 8.1017E-07, indicating insufficient radiation passing through. While the filter BHF CuT2 of thickness 0.28 mm recorded the maximum mean dose of 8.5161E-07 followed by the BHF CuT3 which dissipated mean doses of 8.4426E-07 to the Catphan phantom, suggesting these thicknesses effectively balance attenuation and allow suitable radiation amounts for imaging.

Comparing the two rectangularly shaped copper beam filter and the conically shaped copper material used as beam filters was an eye opening. The output data was noted and graphically represented as Figure 4.15 using their mean dose. The difference is glaring, radiation dose distribution is higher when the Copper filter material was rectangularly shaped over the Copper material that is conically shaped irrespective of the thickness of the beam filter.

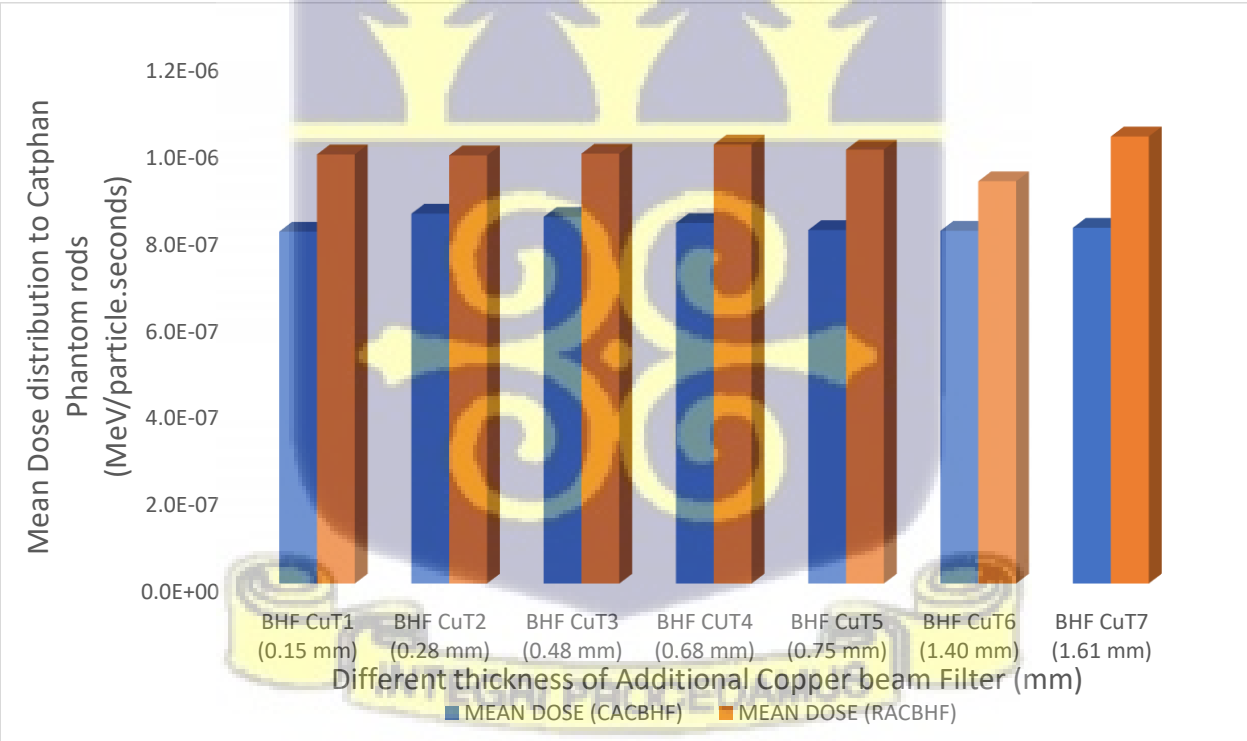

Figure 4. 15: A graphical representation of comparing the dose distribution to the Catphan cells when the conically shaped copper filter and the rectangularly shaped filters were used.

Both share common trend of dose distribution except the 1.40 mm thick rectangularly shaped copper filter, showing a drastic decline in dose from 9.98955E-07 MeV/particle.second to 2.38824E-08 MeV/particle.second breaking the predominate trend showing to showcase contrary 97.06 % percentage deviation. On the converse, excluding the 1.40 mm filter thickness, the general average percentage deviation when both differently shaped copper filter was 17.18 % compared.

4.1.3 Quality Image formation

Mean dose deviation analysis is a crucial method that is used in determining the quality of image formation of the research by evaluating the radiation dose deposited to the Catphan phantom, specifically through different filter configurations. Figure 4.16 illustrates that the mean dose deviates from the mean dose by the different filter configuration. This analysis, conducted through mathematical deductions, helps assess image quality when using a rectangular aluminum filter.

The graphical representation indicates that while energy is distributed across all cells of the Catphan Phantom, some cells exhibit noticeable fluctuations in mean dose deviations. However, the overall dose deposited appears more consistent. Notably, cell 18 recorded the highest energy deposition, regardless of the beam filter's thickness. The maximum energy recorded was 4.63955E-06 MeV/particle.second with a filter thickness of 4.14 mm. In contrast, cell 20 received the minimum energy deposition of 5.83298E-09 MeV/particle.second when the thickness of the filter was 0.5 mm.

This outcome for cell 18 may stem from its position or design within the Catphan phantom, which may be more sensitive to radiation exposure. Generally, higher energy deposition in a specific area can indicate better image quality, as it often correlates with improved contrast and detail resolution.

While other cells display noticeable fluctuations in mean dose deviations, cell 18 demonstrates consistent energy deposition, indicating its variations in radiation exposure—an essential factor for overall image quality.

Additionally, an inverse relationship between filter thickness and radiation dose is observed; as filter thickness increases, the radiation dose typically decreases. This further underscores cell 18's capability to capture finer details effectively.

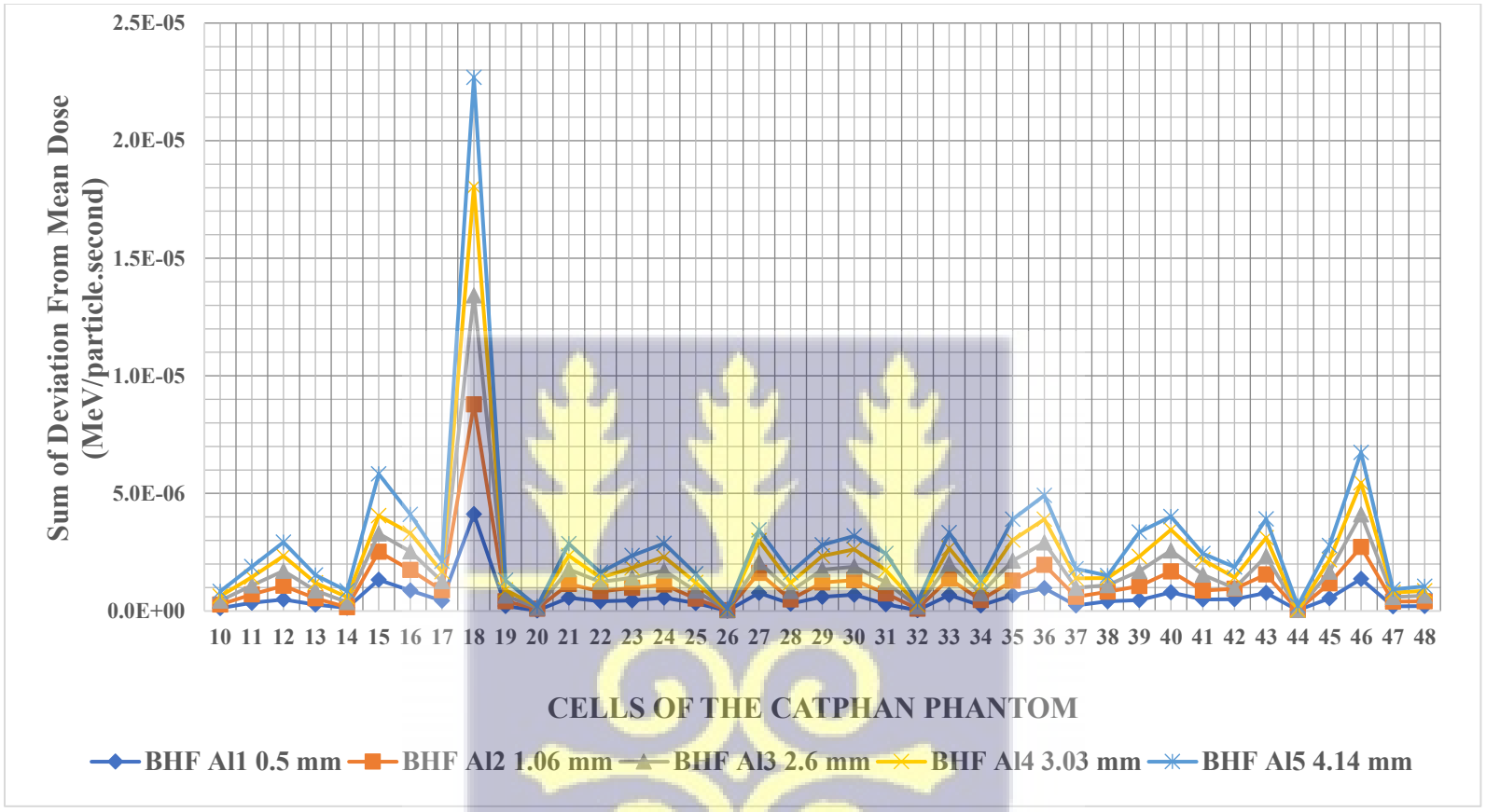

Figure 4.16: Graphical representation of dose distribution of the deviation analysis

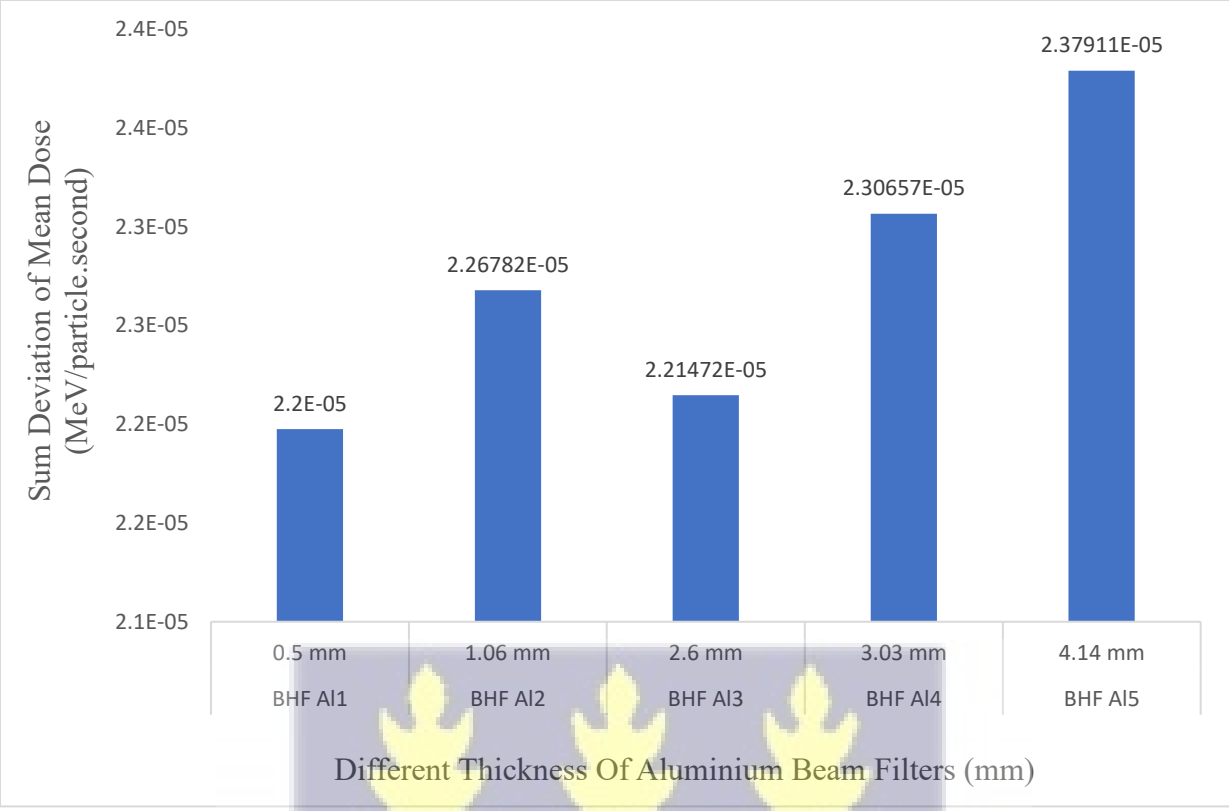

Figure 4.17: A chart representation of the mean energy when the deviation analysis is done to select the optimal thickness for image quality.

A close examination of Figure 4.17 shows that rectangularly shaped aluminium filter of thickness 0.5 mm, gives the weakest and lowest mean energy summation of the absolute deviation of the mean dose from the patient dose. This rectangular-shaped aluminum filter has the lowest sum value of the absolute of the deviation as 2.19759E-05 MeV/particle.second. Whiles the 4.14 mm filter thickness had the maximum mean radiation energy summation of the absolute of the deviation to be 2.37911E-05 MeV/particle.second.

Figure 4.18 represents the deviation analysis for image quality with respect to different thicknesses of the conical shaped additional copper beam filter (CAABHF).

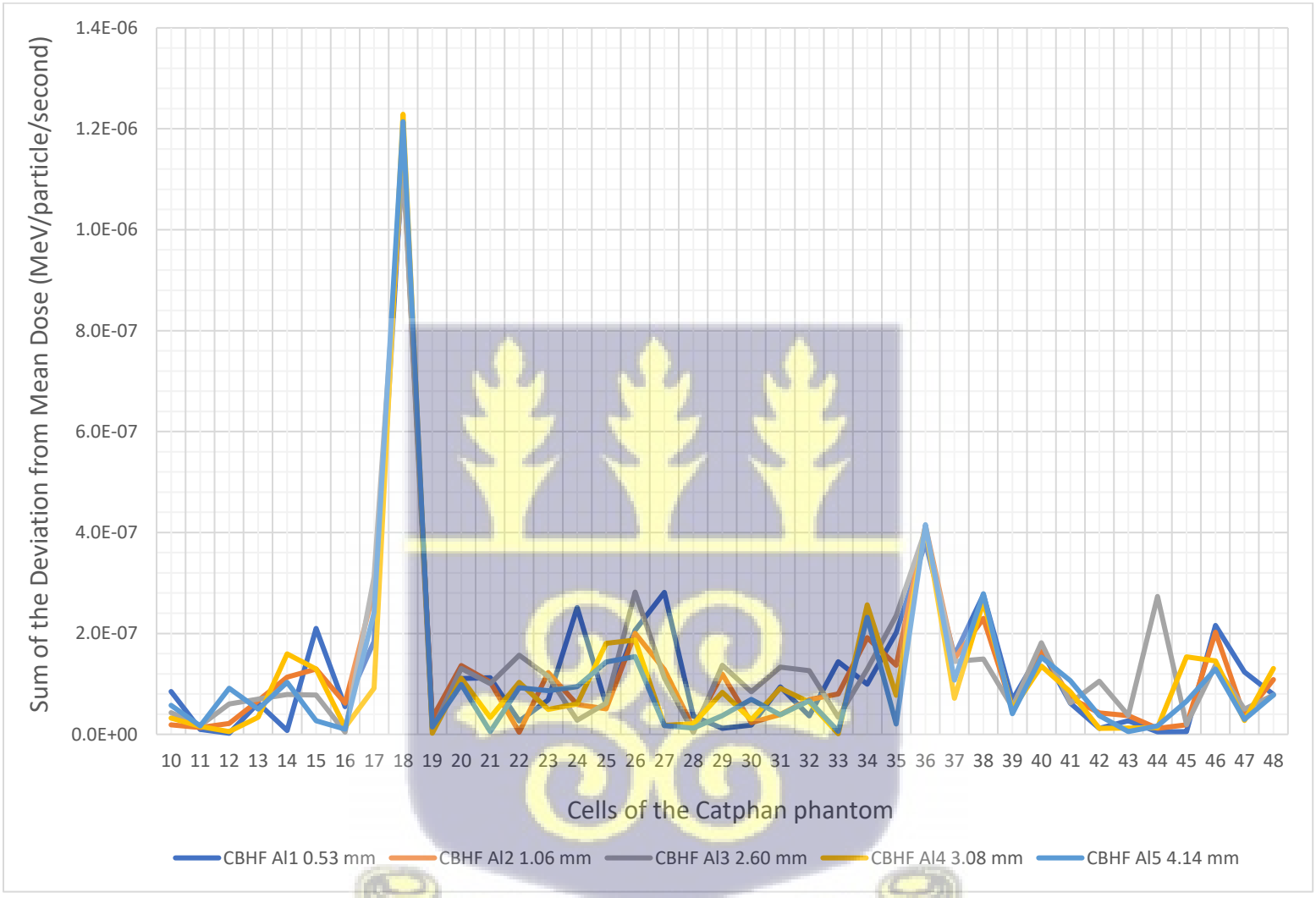

Figure 4.18: Graphical representation of dose deviation analysis with conically shaped Aluminium beam filter

Generally, there was an inverse relationship observed between the thickness of the copper filter and the radiation dose. As the filter thickness increases, the radiation dose tends to decrease resulting to decrease in dose distribution to cell. Where as the other cells showed fluctuations in dose with changing filter thickness, Cell 18 stands out as an exception with a notable increase in dose. It was noted that for each cell, the radiation dose disipated vary as the thickness of the copper filter changes. The thickness of the conically shaped copper filter that registerd the highest deposit at cell 18 was the filter with 0.48 mm. Where as the other cells showed fluctuations in dose with changing filter thickness, Cell 18 stands out as an exception with a notable increase in dose.

Again. in Figure 4.18, the deviation analysis of the Catphan phantom cells exposed to radiation doses with the Rectangular-shaped Additional Copper Beam Hardening Filter (RCABHF) is visually depicted, revealing nuanced variations in dose distribution across different filter thicknesses. Notably, cell 18 emerged as a focal point, demonstrating the highest dose deposition, particularly evident with the 1.61 mm thickness of the rectangular copper filter. Despite observing fluctuations in doses across other cells, cell 18 distinguishes itself with a substantial increase in dose. This observed pattern implies a broad inverse correlation between filter thickness and radiation dose, suggesting a general trend of decreasing radiation dose with increasing filter thickness. Intriguingly, cell 18, characterized by the highest sum of deviation doses, aligns with the best image quality among all cells. Consequently, the data suggests a meaningful connection between deviation dose and superior image quality, underscoring the distinctive imaging excellence of cell 18.

Moreover, the graphical representation in Figure 4.18 effectively communicates the distribution of radiation doses to the Catphan phantom cells, emphasizing a consistent high absorption of dose, notably prominent at varying thicknesses of the copper plate filter and particularly accentuated at

cell 18. A comparative analysis of deviation values across cells reveals varying magnitudes of discrepancy, with some cells exhibiting relatively smaller deviations, such as 0.15 mm, and others manifesting more substantial differences, reaching up to 0.48 mm. Nuanced exploration of the varying deviation values across the different cells significantly enhances our understanding of how different copper filter thicknesses affect radiation doses and, in turn, the image quality of the Catphan phantom simulation. By meticulously examining these deviations, we uncover the intricate relationships between filter thickness and radiation exposure, which are critical for optimizing imaging protocols. This comprehensive insight not only informs best practices in image formation but also ensures that diagnostic accuracy is upheld, ultimately leading to improved clinical outcomes.

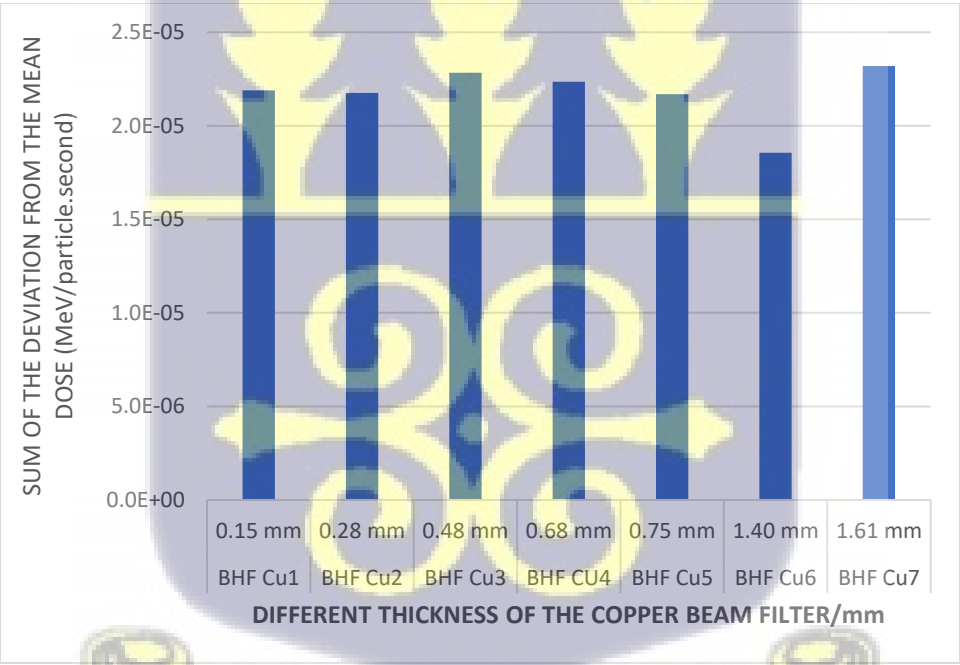

Figure 4.19: A chart to select the optimal thickness of copper for image quality

Further consideration of the graphical representation of figure 4.19, highlights subtle yet significant variations in the cumulative deviations of patient doses from the mean dose across different copper plate filter thicknesses. The overall range of the deviation sum totals fluctuates

from 2.16957E-05 MeV/particle.second to 2.28345E-05 MeV/particle.second, experiencing a sharp decline to 2.98484E-07 MeV/particle.second before a subsequent increase to 2.3036E-05 MeV/particle.second.

Notably, the copper plate filter with a thickness of 1.61 mm exhibited the highest cumulative deviation from the mean dose expexted at 2.32036E-05 MeV/particle.second, indicating significant variability in dose delivery. This dose consistency may pose risks of underdosing or overdosing patients, which is critical in medical imaging, where reliable dose delivery is essential for safety and effectiveness. In contrast, the copper plate filter of thickness 1.40 mm emerged as the least favorable option of 1.85629E-05 MeV/particle.second, demonstrating extremely the lowest summation of deviations from the mean dose. This indicate that the doses delivered are more consistent and closer to the mean value. This is generally favorable as it indicates that patients receive doses that are more predictable and within safe limits, enhancing the reliability of the imaging procedure.

This analysis underscores the intricate relationship between copper plate filter thickness and the cumulative deviations in patient doses, providing valuable insights into optimizing CT scanner settings for enhanced precision especially ensuring patient safety and optimizing imaging outcomes.

An examination of the deviation table (Table 4.10 of Appendix M) for the rectangularly shaped copper beam filters led to graphical representation of of Figure 4.20. The maximum energy received was 4.58469E-06 MeV/particle.second at cell 18, when the filter thickness was 1.61 mm and the minimum energy received was 1.91507E-9 MeV/particle.second, when the thickness of the ractangular shaped copper filter was 1.40 mm.

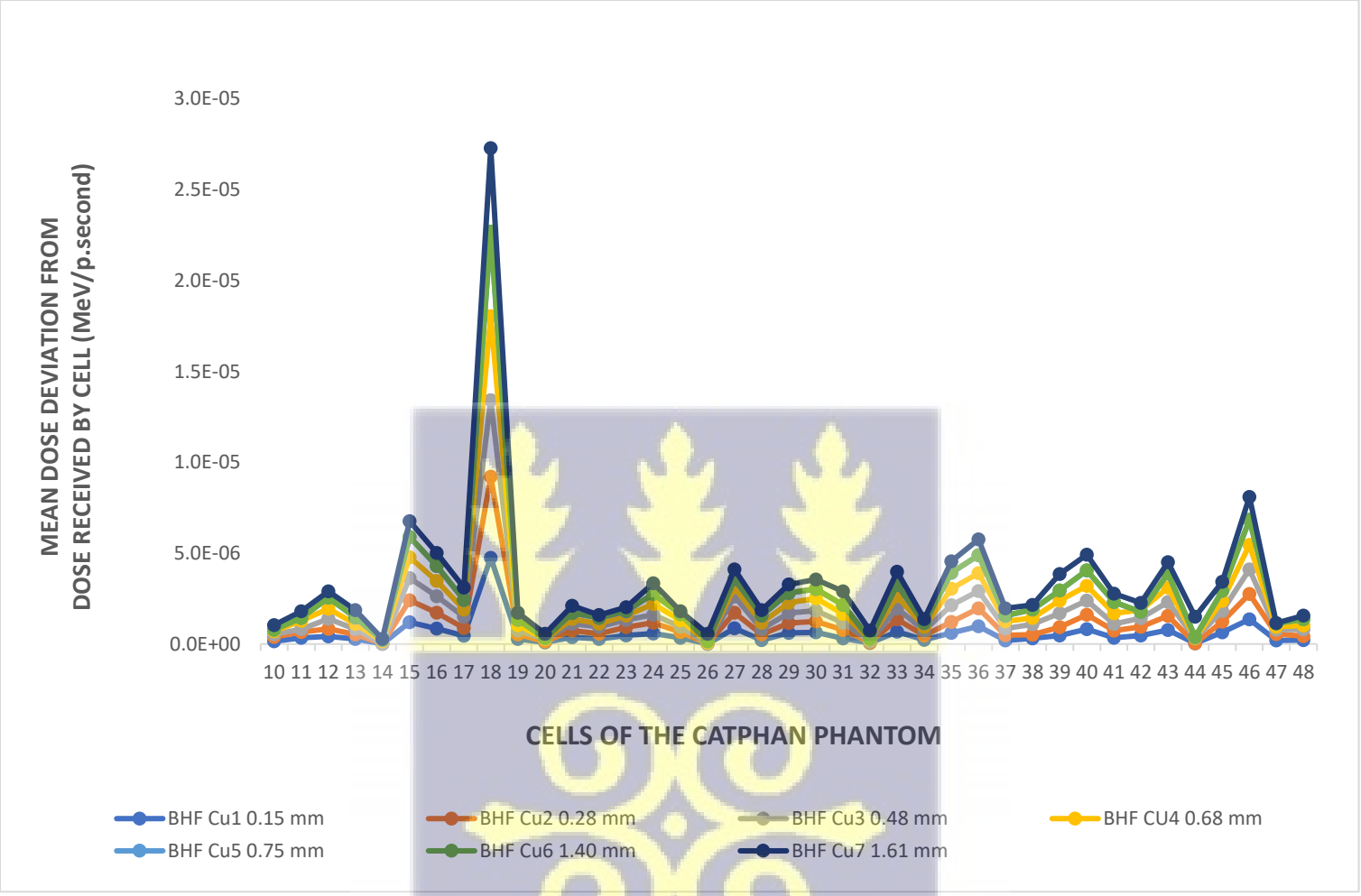

Figure 4.20: Graphical representation after deviation analysis was carried out for the selection of optimal thickness for quality image.

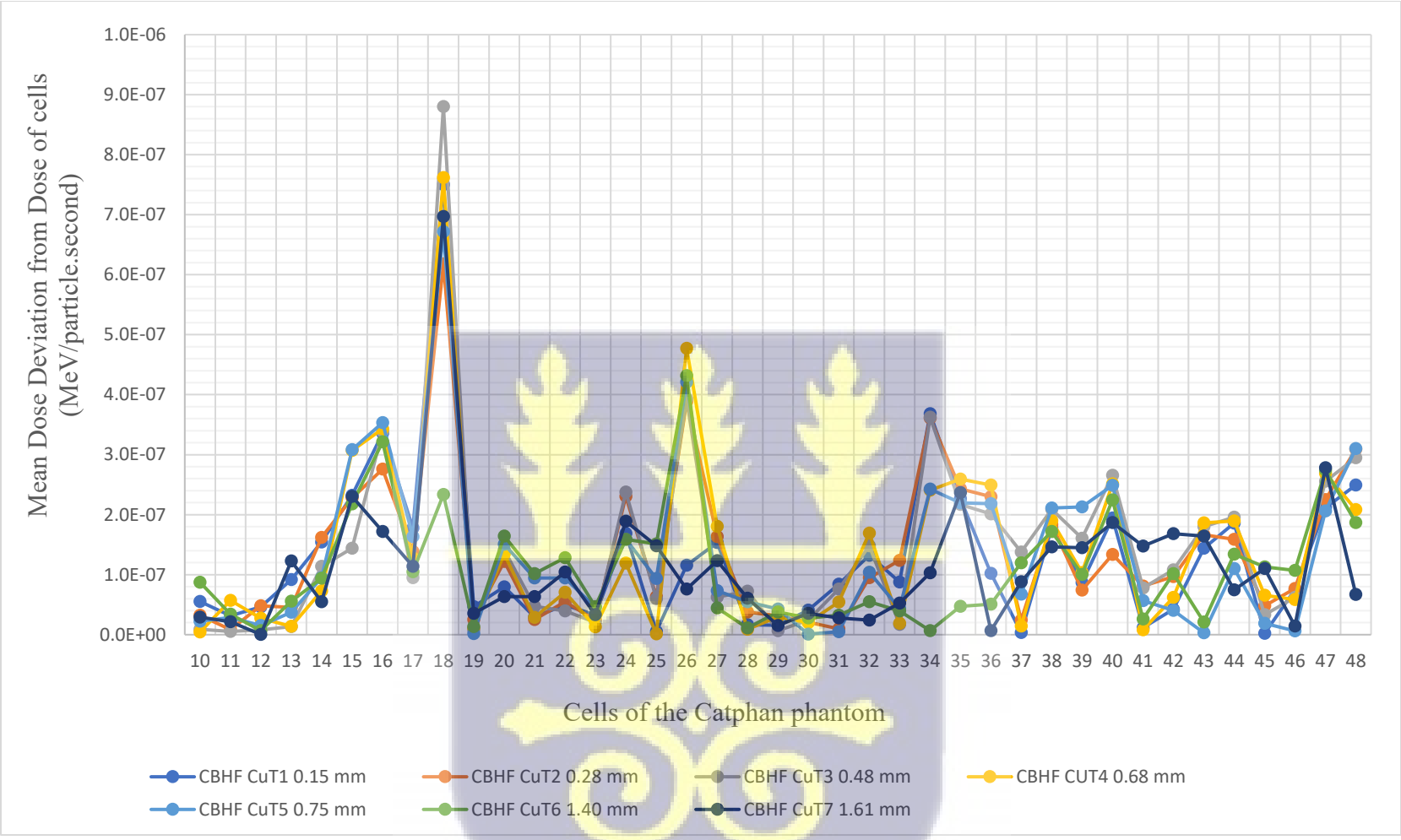

Figure 4. 21: Graphical representation of Catphan cells after deviation analysis was carried out image quality assessment

Again, the evaluated mean energy of Table 4.10 of Appendix M was graphically represented as Figure 4.22

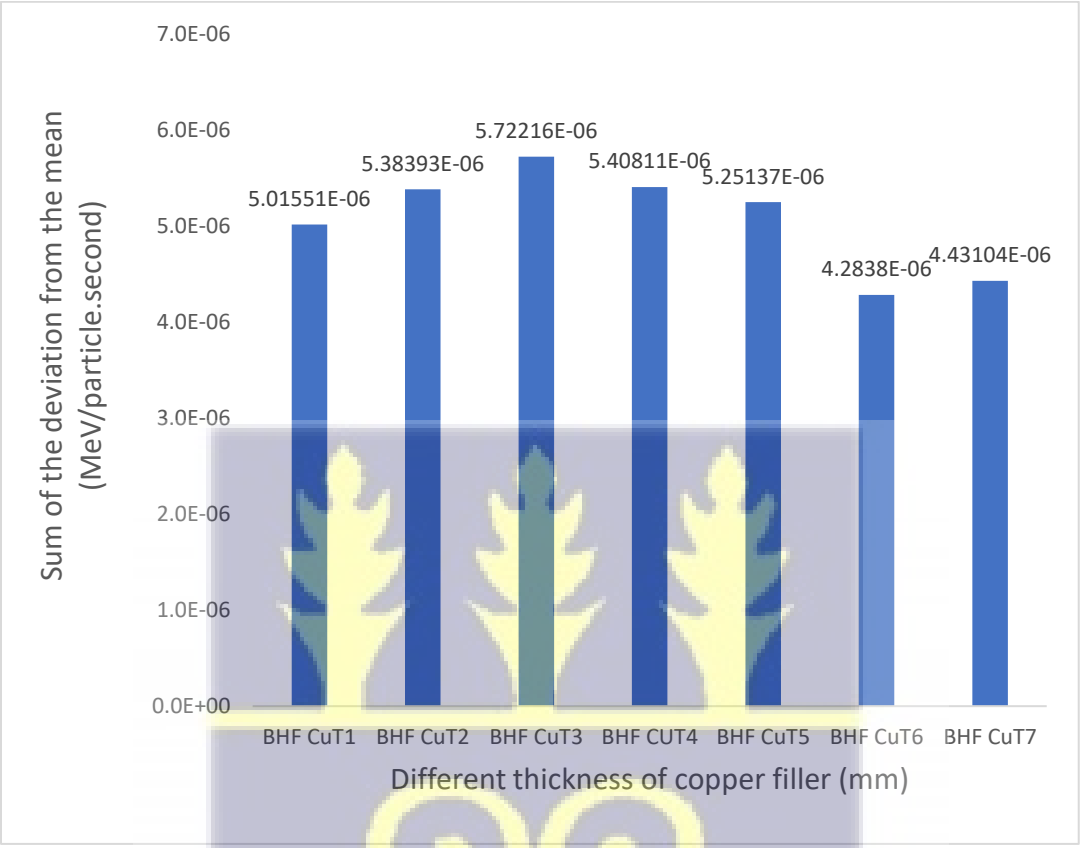

Figure 4. 22: A chart of the sum of deviation of conically shaped copper filter

This virtual representation informed of the maximum summation of deviation of 5.72216E-06 MeV/particle.second of energy observed received by the Catphan cells. This was when the conically shaped Copper was of thickness 0.48. And the minimum summation of deviation of 4.2838E-06 MeV/particle.second was noted, when the thickness of the conically shaped Coper beam filter had a thickness of 1.40 mm. The possible beam filter thickness to give the highest image quality is the filter with thickness of o.48 mm.

Table 4.2: Determination of the best of the Summation of Deviation

ID	DETERMINATION OF BEST FILTER AS OPTIMUM				
1.	Type of Beam Filter Material	**Aluminium**		**Copper**	
2.	Shape Of Filter	**Rectangular**	**Conical**	**Rectangular**	**Conical**
3.	Thickness of filter	**4.14 mm**	**2.60 mm**	**1.61 mm**	**0.48 mm**
4.	Sum of Deviation	**2.37911E-05 MeV/p.sec**	**5.37371E-06 MeV/p.sec**	**2.32036E-05 MeV/p.sec**	**5.72216 E-06 MeV/p.sec**

From Table 4.2 the various filters used and clearly extrapolated with their corresponding energy to be deposited to the cell of the Catphan phantom. It could be deduced that generally conically shaped filter materials are better. But specifically, the conically shaped Copper filter gave better filtration than the rectangular filters hence the energy emitted was 5.72216 E-06 MeV/particle.second while the rectangular shaped Aluminium emitted 2.32036E-05 MeV/particle.second and again the greater the summation of deviation the best quality of image was given by the modelled CT scanner.

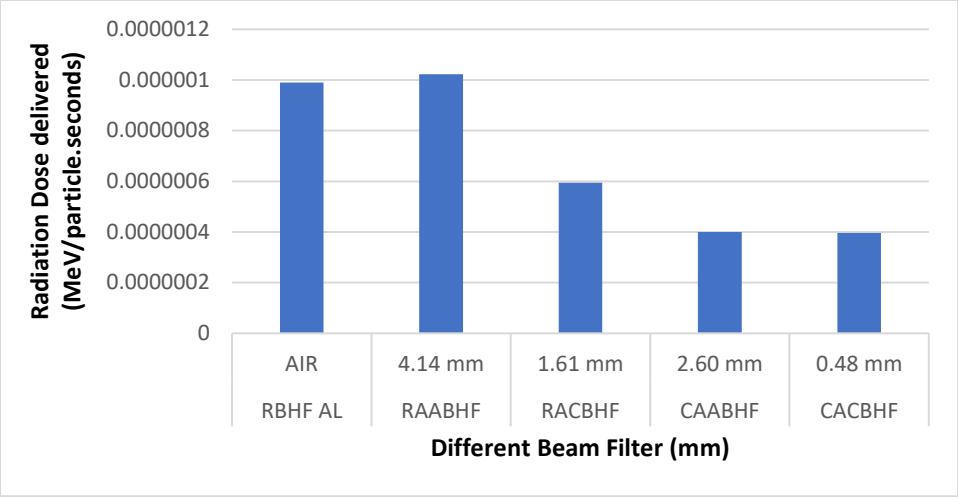

Figure 4.23: A chart indicating the summation of the mean dose deviations for different Beam Hardening Filters

Figure 4.23 indicate a bar chart comparing radiation dose delivered at different beam filters; RACBHF-4.14 mm, RACBHF-1.61 mm, CAABHF-2.60 mm and CACBHF-0.48 to when there was no filter RBHF AL (AIR). From the study, it can be deduced there was reduction in the dose delivered with the conically shaped filters as compared to the rectangularly shaped filters. When 4.14 mm rectangular shaped Aluminium filter (RAABHF) was used as optimum filter, 1.02287E-06 MeV/particle.second was delivered to Catphan phantom rods (cells), and 3.9772E-07 MeV/particle.second was delivered to the Catphan phantom when the Aluminium was conically shaped (CAABHF) at a thickness of 2.60 mm. Again, when conically shaped Copper was used as an optimum filter at a thickness of 0.48 mm, an energy of 3.95988E-07 MeV/particle.second was delivered to the Catphan rods. But when the rectangularly shaped Copper of thickness 1.61 mm was an optimum filter, it exposed 5.94964E-7 MeV/particle.second to the rods of the Catphan phantom.

4.2.3.1 Patient dose

As observed in the graphical representations (Figures 4.15, 4.19, 4.12 and 4.14), that the mean dose received by the Catphan phantom increased notably with increasing filter thickness. This

trend is consistent with the findings of Ay et al. (2013), affirming that as filter thickness increases, the dose received by the rods of the Catphan phantom increases, and vice versa.

This research study reveals that, the thickness of the copper and aluminum beam hardening filter significantly influence the dose delivered and image quality. Therefore, filtering plays a pivotal role to substantially reduce the dose delivered to the Catphan during CT imaging. However, it necessitates an optimum filter by which the images still retain their diagnostic quality.

The lower energies observed as received by the rods of the Catphan phantom are attributed to the soft and low-energy beam filtration, necessary for transforming the polychromatic X-ray beams emitted by CT scanner into a homogeneous high-energy beam essential for quality image formation.

However, when the thickness of the filtering material becomes excessively large, a problem arises. The beam is overly filtered, resulting in the production of beams that are too soft X-rays and low in energy. These beams, also known as soft beams, lack the necessary hardness to penetrate the Catphan phantom and are instead absorbed by it. This excessive filtration leads to a significant increase in patient dose exposure, which could potentially compromise the patient's health. The thicker the beam filter the more excessive the filtration of the polychromatic beams emitted by the X-ray source. This excessive filtration of the beam makes the beam to become excessively soft. When such a beam is exposed to the patient in a real clinical setting necessitate detrimental effect. Excessive filtration led to higher radiation absorption by the energy bins of the Catphan phantom. As a result, the image quality was negatively impacted, potentially leading to incorrect diagnoses. The lower energy of the incident photons causes more attenuation and results in a higher dose being delivered to the patient.

Therefore, the best optimum filter thickness to be selected considering patient dose only in relation to ALARA principles is the 0.5 mm thickness aluminum beam hardening filter and for copper plate, the 1.40 mm thickness of copper beam hardening filter

4.1.3.2 Image Quality

In Figure 4.11, the thickness of the copper filter yielded the highest summation of deviations from the mean dose, was 0.48 mm. This particular thickness serves to effectively enhance the beam hardening characteristics, resulting in a more precise and consistent dose delivery to the target area.

Conversely, the thickness with lowest summation of deviation is 1.40 mm. this thickness significantly degrades the image clarity and quality. Utilizing such a thick copper plate hampers the quality of the resulting images, making it challenging to discern fine details and potentially compromising diagnostic accuracy. For the aluminum filters, the filter thickness with the maximum summation of the absolute deviation was 4.14 mm thickness filter and the lowest was the filter with 0.5 mm thickness.

To ensure optimal image quality and accurate dose distribution, it is evident that selecting the appropriate thickness of the copper plate plays a critical role in optimizing both dose distribution and image quality. A thickness of 0.48 mm of the copper plate filter and 4.14 mm thickness of the aluminum plate filter is recommended for maximizing dose accuracy, to compromise a favourable balance between beam hardening and image quality, while avoiding the use of a 1.40 mm thick copper plate and 0.5 mm thick aluminum plate filter is advised to ensure high-quality imaging in medical applications. This careful consideration of the copper plate's thickness can significantly enhance the overall effectiveness of the imaging, radiation therapy processes and patient care.

4.2 Discussion

In the field of medical imaging, the application of beam hardening filters (BHF) plays a critical role in optimizing image quality while minimizing radiation exposure to patients. This research focuses on the computational assessment of additional copper (Cu) and aluminum (Al) BHFs and their impact on patient dose and image quality in a 64-slice Philips CT scanner. The findings underscore the significant influence that these filters have on both patient safety and diagnostic accuracy.

Beam hardening, while a natural phenomenon in CT scanning, can lead to non-uniform radiation distribution and the introduction of image artifacts. Therefore, selecting materials with proven attenuative properties that are both readily available and cost-effective is essential for achieving uniform radiation distribution and high-quality imaging results. A crucial outcome of this study is the determination of optimal filter thicknesses and design for an additional filter plate, which effectively balances the need for dose reduction with the preservation of image quality.

The delicate trade-off inherent in the application of BHFs is vital for ensuring that diagnostic imaging remains both effective and safe. In the quest to identify an optimal beam hardening filter (BHF) thickness, a careful balancing approach was undertaken to achieve the best compromise between dose reduction and image quality. This process involved calculating the Absolute Mean Dose Deviation (MDD), which provides insight into the impact of various filter configurations on the delivered dose and the resulting image characteristics. By quantitatively evaluating the effects of different filter materials—specifically aluminum and copper, as well as their shapes and thicknesses, the study aims to identify configurations that provide the best compromise between patient dose and image quality.

Through careful assessment of the graphical data and statistical metrics, the analysis illuminated the performance of various BHFs and emphasise their importance in enhancing spatial resolution and noise-to-contrast ratios.

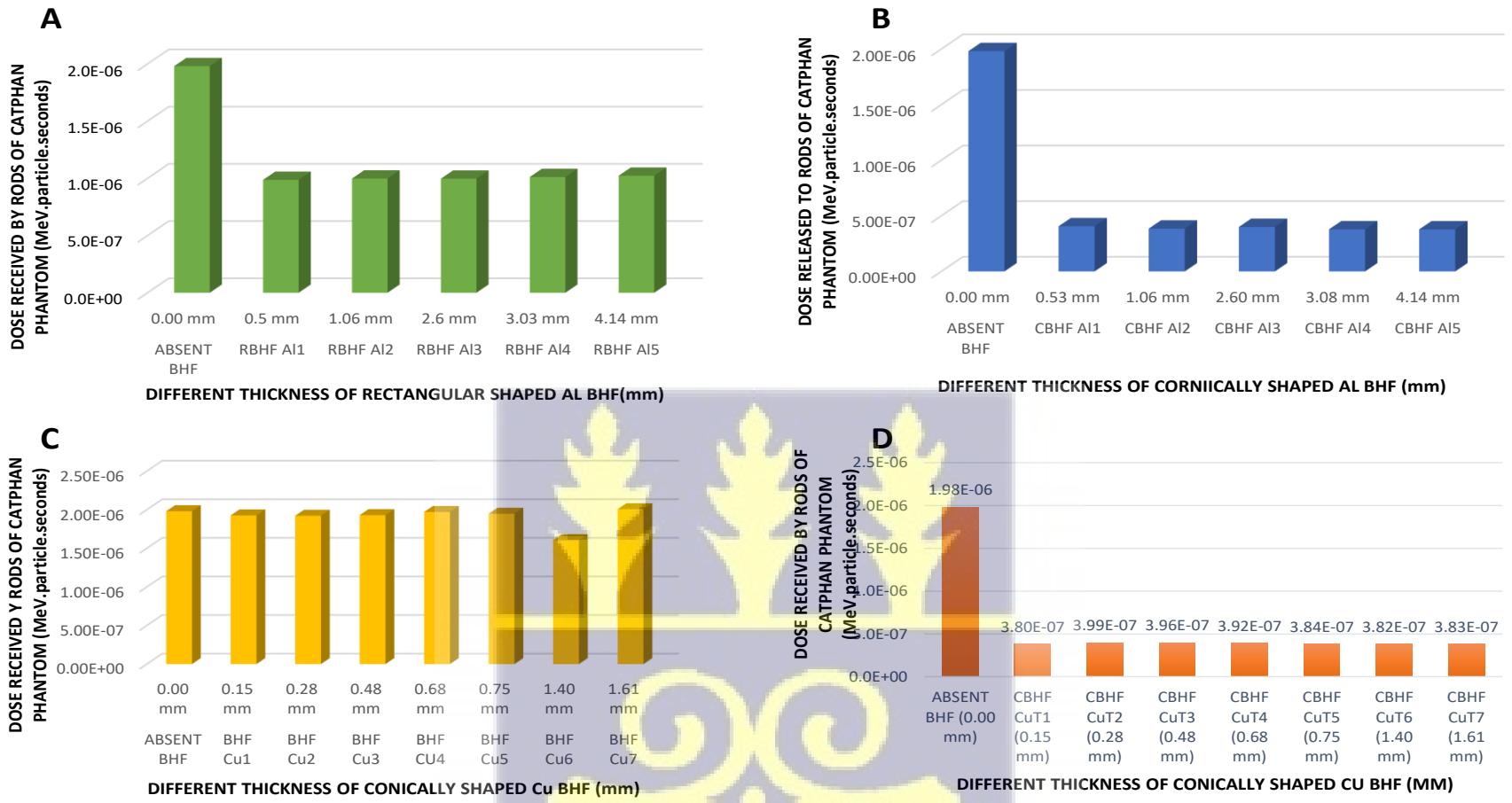

Figure 4. 24A Four different graphical representation labelled A – D illustrating the mean doses received per particle by the Catphan phantom when different materials shaped either rectangularly or conically at different thicknesses. Graph A is comparing rectangularly shaped aluminum BHF at different thicknesses against the CT scanner with no additional filter, graph B compares conically shaped aluminum BHF at various thicknesses against the CT scanner with no additional filter, graph C illustrates the mean doses with rectangularly shaped copper BHF at different thicknesses compared to the absent filter and graph D demonstrates mean doses with conically shaped copper BHF at different thicknesses against the absent filter.

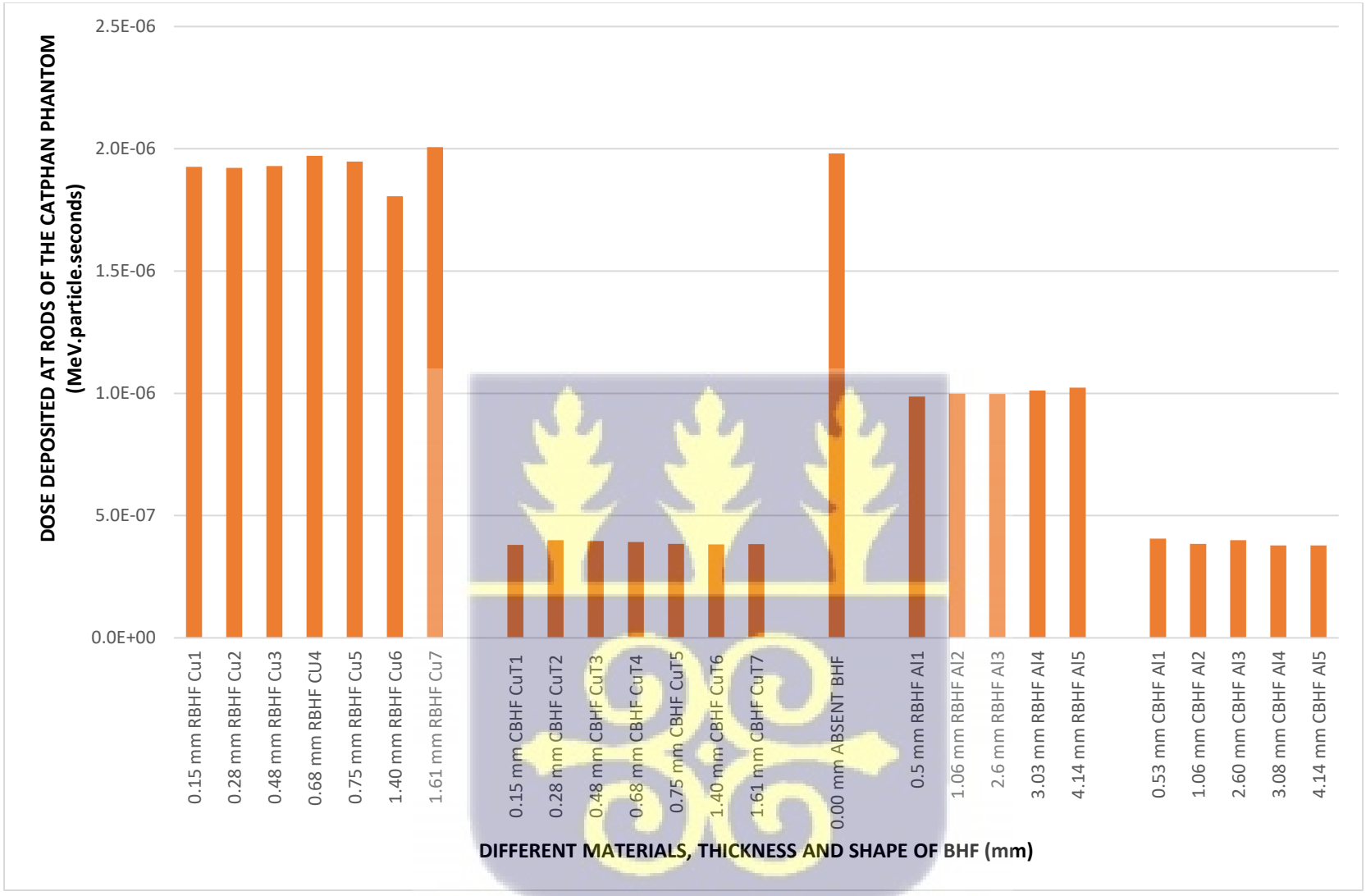

Figure 4.25B A Is a plot of the mean dose received per particle by the virtual Catphan phantom when all the differently shaped additional BHF materials either rectangularly or conically are used with varied thickness and compared to the baseline filter (i.e without a beam hardening filter, BHF) for the selection of the best filter that will yield an improved image.

The comparative analysis of figure 4.24A and figure 4.24B, revealed key insights into the beam filtering at the different configurations of beam-hardening filters (BHFs) to achieve an enhanced CT image. The graphs compared the mean dose delivered to a virtual Catphan phantom using different filter materials (aluminum and copper), at different shapes (rectangular and conical), and varying the thicknesses. The results of the different BHFs were compared against a baseline (i.e. without an additional filter thus by simulating the configuration from the CT manual).

The graphical representation demonstrates that filter material and shape significantly influence the mean dose received by the phantom. As shown in figure 4.24A and figure 4.24B, rectangularly shaped aluminum BHFs are compared to rectangularly shaped copper BHFs and conically shaped aluminum BHFs are compared to conically shaped copper BHFs. These comparisons indicated conically shaped BHF demonstrates a notable reduction in the mean dose received by the Catphan phantom compared to the CT scanner simulation without an additional filter.

Again, even though the aluminum filters significantly showed reduction in mean dose conversely, copper filters consistently result in a lower mean dose to the Catphan phantom than aluminum filters of similar thickness. This superior efficacy outcome is expected, as copper, with its higher atomic number, is generally more effective at filtering out the lower-energy photons in the X-ray beam, thereby achieving greater dose reduction.

However, it is essential to note that while a lower mean dose is a desirable outcome, selecting the optimal filter configuration solely on this basis is insufficient for predicting image quality. This is due to a fundamental inverse relationship: as the dose decreases, image noise increases. This phenomenon is a direct result of quantum mottle, which describes the statistical fluctuations in the number of X-ray photons reaching the detector. A lower photon count, caused by a thicker filter or a less intense X-ray beam, leads to more pronounced quantum mottle and a grainier, noisier image.

As the dose decreases, image noise tends to increase, which can detrimentally affect the image quality metrics such as Noise-to-Contrast Ratio (CNR) and Spatial Resolution. An increase in quantum mottle significantly lowers the CNR, making it more challenging to differentiate between objects with subtle differences in density, such as soft tissues or low-contrast lesions. The improved dose reduction from a more effective filter like copper may, therefore, come at the cost of reduced visibility. Also Elevated noise levels can obscure fine details and blur the appearance of sharp edges, thereby degrading the perceived spatial resolution of the image.

Therefore, while these studies highlight the superior dose-reducing properties of copper BHFs, an optimal filter configuration requires balancing dose reduction against the preservation of diagnostically valuable image quality. The ideal filter is one that minimizes dose by effectively pre-hardening the beam, yet does not introduce an unacceptable level of quantum mottle that would compromise CNR and spatial resolution.

MEAN DOSE DEVIATION ANALYSIS FOR OPTIMAL FILTER SELECTION

The process of selecting an optimal beam-hardening filter (BHF) for the purpose of this study involved achieving a balance between minimizing radiation dose exposure and maintaining high image quality. This analysis utilizes the Mean Dose Deviation (MDD) metric to evaluate the effectiveness of various filter configurations. This metric quantifies the dose reduction achieved by conically shaped filter material compared to the mean dose by the equation:

$$\textbf{Absolute Mean Dose Deviation}(MDD) = \left|\left(Dose_{filter} - \textbf{Mean dose}\right)\right| \ldots\ldots \textbf{Eqn 4.1}$$

The MDD data generated is graphically extrapolated as shown as figure 4.24C below, correlates the different BHF materials with reduced dose (Aluminum and Copper) both conically shaped.

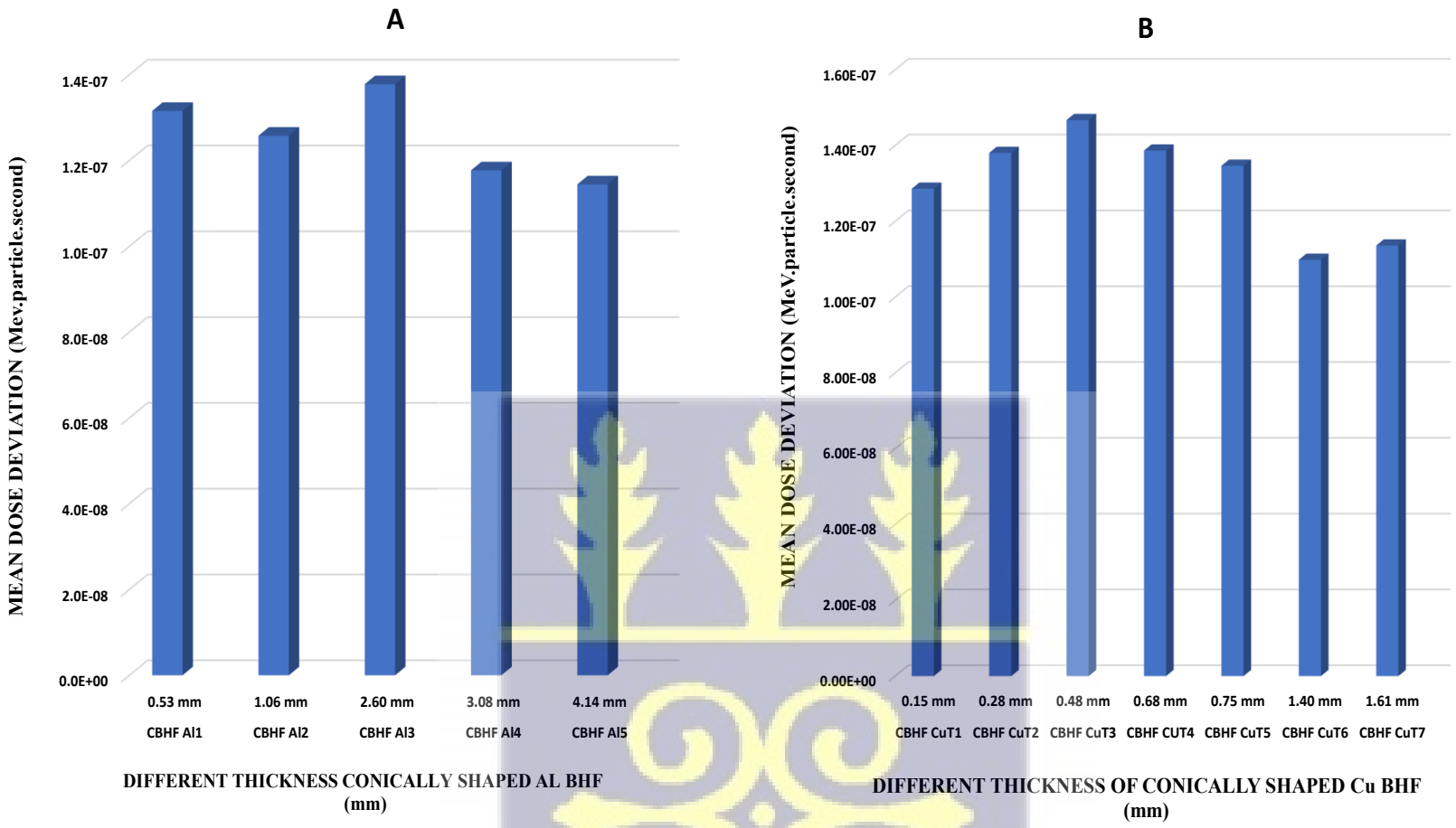

Figure 4.26C Graph showing the Mean Dose Deviation (MDD) for conically-shaped BHF materials of different thickness

The graphs on MDD illustrates that both the material and shape of the filter significantly influence the dose received by the phantom. As expected, copper filters consistently demonstrate a comparable higher absolute MDD as compared to aluminum filters of similar thickness, indicating that copper is generally more effective at filtering low-energy photons and achieving a higher MDD for attaining an enhanced CT image.

Table 4.3D: Shows a summary information of the possible filter configuration to provide better image quality

FILTER MATERIAL	SHAPE OF FILTER MATERIAL	MAXIMUM MEAN DOSE DEVIATION	MAXIMUM FILTER THICKNESS	MINIMUM MEAN DOSE DEVIATION	MANIMUM FILTER THICKNESS	RANGE OF MDD	ENERGY DOSE DEPOSITED	PATIENT DOSE RECEIVED	IMAGE QUALITY (Contrast, Noise, Resolution)
Copper	Conical	1.47E-07	0.48 mm	1.10E-07	1.40 mm	3.70E-08	Lowest	Lowest	Excellent contrast, low noise and higher spatial resolution
Aluminum	Conical	1.38E-07	2.60 mm	1.14E-07	4.14 mm	2.40E-08	Low	Low	Good contrast, low noise and good spatial resolution

An evaluation of the data on MDD for conically-shaped filters reveals specific optimal configurations for each material. Among the conically-shaped aluminum filters, the one with a thickness of 2.60 mm exhibits the highest absolute mean dose deviation of 1.38E-07 MeV/particle.second. Similarly, the conically-shaped copper filter with a thickness of 0.48 mm demonstrates the highest absolute mean dose deviation within its group, with a value of 1.47E-07 MeV/particle.second. A comparative summary of the data from both materials shows that conically-shaped copper filters consistently yield higher mean dose deviations, suggesting they are a more effective choice for dose reduction.

While a higher MDD indicates a more significant dose reduction, this is only one aspect of filter performance. It is crucial to consider the inverse relationship between dose and image noise. A substantial reduction in dose can lead to an increase in image noise due to quantum mottle, which in turn degrades the image's overall quality by negatively impacting the noise-to-contrast ratio (CNR) and perceived spatial resolution.

Based on a comprehensive analysis of the dose reduction data, the conically-shaped copper filter with a thickness of 0.48 mm emerges as the optimal choice hence the optimal filter. It provides the best compromise between dose reduction and the preservation of image quality by demonstrating the highest mean dose deviation. This specific filter configuration is projected to yield images with high spatial resolution, an excellent noise-to-contrast ratio, and superior uniformity, ensuring the diagnostic utility of the final image without exposing the patient to unnecessary radiation.

The identified optimal filter thicknesses underscore the effectiveness of beam hardening filters in achieving the dual objectives of dose reduction and image quality preservation. The substantial reduction in patient dose, coupled with the maintenance of reasonable image quality in terms of contrast and spatial resolution, positions BHF as a valuable tool for healthcare professionals seeking to optimize CT imaging procedures.

The practical implications of this research are noteworthy. By empowering healthcare professionals with information on optimal filter thicknesses, the study facilitates informed decision-making in the clinical setting. The potential for a remarkable reduction in radiation exposure without compromising diagnostic quality aligns with the overarching goals of enhancing patient care and safety.

In the context of the increasing utilization of CT scans, the study's contribution extends beyond individual patient care. The optimization of beam hardening filters not only mitigates health risks associated with ionizing radiation but also contributes to cost-effectiveness and advances in medical imaging practices. Clinicians can leverage these findings to implement more radiation-conscious protocols, ultimately benefiting both individual patients and the healthcare system at large.

4.3 Limitations to the study

Despite the significant contributions of this research to the understanding of beam hardening filters in X-ray Computed Tomography (CT), several important limitations must be acknowledged. First, the study's reliance on virtual experimental phantom measurements may not fully capture the complexities and variability of human anatomy and pathology. While computational models provide valuable insights, they may not accurately replicate the unique interactions that occur in live patients, potentially limiting the full applicability of the findings to real-world clinical scenarios.

First, the study primarily relies on virtual experimental phantom measurements, which, although sophisticated, may not fully replicate the complexities and variability of human anatomy and pathology of real-world patient scenarios. This reliance on computational models provides valuable insights however, could limit the generalizability of the findings to clinical practice, where variations in patient anatomy and positioning can significantly influence dose distribution and image quality.

Additionally, the Monte Carlo N-Particle Code (MCNP) simulations, while highly regarded for their accuracy, depend on precise input parameters and modeling assumptions. Any inaccuracies

in these parameters could introduce biases in the results, affecting the reliability of the optimal filter thicknesses proposed. Moreso, the specific configurations tested may not encompass all possible filter designs or thicknesses, that could further optimize patient safety and diagnostic efficacy.

Lastly, as technological advancements in CT imaging continue to evolve, the findings of this study may need to be reassessed in the context of new hardware and software developments. Future research should aim to validate these results through empirical studies involving human subjects and explore the long-term implications of using various beam hardening filters across diverse clinical populations. This will ensure that the recommendations provided remain relevant and effective in enhancing patient care while minimizing radiation exposure.

CHAPTER FIVE

CONCLUSION AND RECOMMENDATION

This chapter recaps the study by presenting the conclusion and recommendations. This chapter assesses the objectives to see whether they were met and recommendations for further study were also presented here.

5.1 Conclusion

In conclusion, this research employed a computational simulation approach to examine the impact of beam hardening filters (BHF) on CT image quality and patient radiation dose in a 64-slice CT scanner. The findings revealed significant variations in dose distribution across different regions of the digital Catphan phantom when utilizing various thicknesses of aluminum and copper as BHFs.

Through a thorough analysis of Absolute Mean Dose Deviation (MDD), identification is made of optimal filter thicknesses that maximize diagnostic efficacy while minimizing patient radiation exposure. The results underscored that BHF configurations significantly influence image quality; some configurations improved image quality, while others imposed a trade-off between quality and dose. This emphasizes the necessity of selecting materials and designs that effectively mitigate beam hardening effects while ensuring high spatial resolution, noise-to-contrast ratios, and overall image uniformity.

The optimal configurations identified include a 0.48 mm thickness of the conically shaped copper filter and a 1.61 mm thickness of the rectangular copper filter. For aluminum, the optimal thickness yielding the best image quality is 2.60 mm of the conically shaped filter. These configurations

allow for adequate X-ray beam filtration, significantly reducing patient dose while maintaining acceptable image quality in terms of contrast and spatial resolution.

The study highlights the importance of carefully selecting BHF configurations to achieve optimal imaging outcomes. Utilizing materials with superior attenuative properties, particularly copper and aluminum, enables clinicians to enhance diagnostic quality without unnecessary radiation exposure.

Analyzing radiation absorption by the Catphan phantom, which simulates human tissue, provided deeper insights into the implications of BHF on patient exposure. This understanding can aid in optimizing CT imaging protocols, balancing radiation dose minimization with diagnostic accuracy.

Ultimately, the insights from this research establish a valuable foundation for future studies and clinical applications, empowering practitioners to make informed decisions that prioritize patient safety and enhance diagnostic accuracy. The commitment to refining imaging techniques through evidence-based methods is essential for advancing the quality of care in medical imaging and ensuring optimal patient outcomes.

5.2 Recommendation

It is recommended that Further research in this area could explore to assess the scanner's dose efficiency and image quality with the recommended filters in a clinical setting. Also, additional factors that may influence BHF optimization and expand the understanding of its impact on CT imaging.

REFERENCES

Anaafi, E. (2020). *Computed tomography protocol optimisation for pediatric head trauma: radiation on dose and image quality assessment.* Accra: University of Ghana http://ugspace.ug.edu.gh. Retrieved from University of Ghana http://ugspace.ug.edu.gh.

Ay, M. R., & Zaidi, H. (2005). Development and validation of MCNP4C-based Monte Carlo simulator for fan-and cone-beam x-ray CT." 50.20 (2005): 4863. *Physics in Medicine & Biology, 50*(20), 4863.

Ay, M. R., Abolfazl, M., Asghar, M., Hossien, G., Pardis, G., & Habib, Z. (2013). Experimental assessment of the influence of beam hardening filters on image quality and patient dose in volumetric 64-slice X-ray CT scanners. *Physica Medica, 29*(3), 249-260.

Barua, R., Datta, S., & Banerjee, D. (2022). Computational Study of In-Vivo CT-Based FEM Application in Bone Tissue Engineering. *Technological Adoption and Trends in Health Sciences Teaching, Learning, and Practice*, 300--316.

Bazalova, M., & Verhaegen, F. (2007). Monte Carlo simulation of a computed tomography x-ray tube. *Physics in medicine and biology, 52*, 5945–5955. doi:10.1088/0031-9155/52/19/015

Benítez, R. B., Ehsan , S., Pelc, N. J., & Ning, R. (February 2010). Development of a beam hardening filter and characterization of the spatial resolution for a Cone Beam CT imaging system. *Physics of Medical Imaging, 7622*, 762237-1. doi:10.1117/12.844333

Boas, F. E., & Fleischmann, D. (2012). CT Artifacts: Causes and Reduction Techniques. *Imaging Med., 4*(2), 229-240. doi:10.2217/IIM.12.1

Catphan. (2006). *Catphan 500 and 600 Manual.* New York: The Phantom Laboratory Incorporated.

Chantzi, S., Papanastasioa, E., Athanasopoulou, C., Molyvda-Athanasopoulou, E., Bamidis, P., & Siountas, A. (2020). Design of a Monte Carlo model based on dual-source computed tomography (DSCT) scanners for dose and image. *Polish Journal of Medical Physics and Engineering, 26*(1), 11-20.

Chen, S., Xiaoqi , X., Lei , L., Leifei , L., Yu , H., Jingyu , W., & Bin, Y. (2016). A filter design method for beam hardening correction in middle-energy x-ray computed tomography. *Eighth International Conference on Digital Image Processing (ICDIP 2016), 10033*, 1004--1009.

Choi, J. H., Kim, T., Jung, J., & Joo, J. W. (2020). Development of a computational model for optimizing the design of a beam hardening filter for CT imaging of high-density materials. *Journal of X-Ray Science and Technology, 28*(3), 535-550.

Chu, J. C., Galvin, J. M., Lockett,, P., & Bloch., P. (1981). Use of a tungsten filter to improve beam uniformity. *Medical Physics, 8*(4), 520-522.

Cierniak, R. (2011). *X-ray computed tomography in biomedical engineering.* London: Springer Science & Business Media.

Cohen, L., Manion, L., & Morrison, K. (2007). Experiments, quasi-experiments, single-case research and meta-analysis. *Research methods in education, 6*.

Cruz-Bastida, J. P., Zhang, D., Liu, X., & Shaw, C. C. (2014). A comparison of image quality and dose delivered between traditional and new iterative techniques in a GE discovery CT750 HD scanner. *Journal of Applied Clinical Medical Physics,, 15*(1), 4578.

Davis, A. T., Palmer, A. L., & Nisbet, A. (2020). Can different Catphan phantoms be used in a multi-centre audit of radiotherapy CT image quality? *Physica Medica, 78*, 38-47.

Dougherty, G., & Davros, W. (2010). Digital image processing for medical applications. *Medical Physics, 37*(2), 948. doi:10.1118/1.3285412

Faby, S., Kuchenbecker, S., Sawall, S., Simons, D., Kach, M., & Kachelrieß, M. (2015). Performance of today's dual energy CT and future multi energy CT in virtual non-contrast imaging and in iodine quantification: a simulation study. *Medical physics, 42*(7), 4349-4366.

Forster III, A. R., Rising, M. E., & Sood, A. (2021, July 15). *The History of Monte Carlo and MCNP at Los Alamos [Slides].* Los Alamos National Lab.(LANL), Los Alamos, NM (United States).

Glas, M. V. (2000). Principles of Computerized Tomographic Imaging.

Goodenough, D. J., Weaver, K. E., & Davis., D. O. (1977). Development of a phantom for evaluation and assurance of image quality in CT scanning. *Optical engineering, 16*(1), 52-65.

Hendee, W. R., & Ritenour, R. E. (2003). *Medical imaging physics* (4th ed.). John Wiley & Sons.

Hendee, W. R., Becker, G. J., Borgstede, J. P., Bosma, J., Casarella, W. J., Erickson, B. A., . . . Wallner, P. E. (2010, October). Addressing Overutilization in Medical Imaging. *Radiology, 257*(1), 240–245. doi:10.1148/radiol.10100063

Hsieh, J. (1998). Adaptive streak artifact reduction in computed tomography resulting from excessive x-ray photon noise. *Medical Physics, 25*(11), 2139-2147.

Hsieh, J. (2003). *Computed tomography: principles, design, artifacts, and recent advances.* SPIE press.

Husby, E., Svendsen, , E. D., Andersen, H. K., & Martinsen, A. T. (2017). 100 days with scans of the same Catphan phantom on the same CT scanner. *Journal of applied clinical medical physics, 18*(6), 224-231.

ICRP. (2007, March). Managing patient dose in multi-detector computed tomography (MDCT). *ICRP publication 102 (Annals of the ICRP)*(37), 1-79.

Jansen, J. T. (2009). Development of PC based Monte Carlo simulations for the calculation of scanner-specific normalized organ doses from CT},. *and Shrimpton, Paul C and Zankl, Maria*.

Jennings, R. J. (1988). A method for comparing beamhardening filter materials for diagnostic radiology. *Medical Physics (Lancaster), 15*(4), 588-599.

Justin, C. E., Nathan, C. D., Jonathan, T. E., & Jennifer, B. L. (2013, December). CT Radiation Dose: Current Controversies and Dose Reduction Strategies. *American Journal of Roentgenology, 201*(6), 1283-1290.

Kalender, W. A. (2011). *Computed tomography: fundamentals, system technology, image quality, applications.* John Wiley & Sons.

Kalra, M. K., Maher, M. M., Toth, T. L., Hamberg, L. M., Blake, M. A., Shepard, J.-A., & Saini, S. (2004). Strategies for CT radiation dose optimization. *Radiology, 230*(3), 619-628.

Karabut, A. B. (2006). Research Into Characteristics of X-Ray Emission Laser Beams from Solid-State Cathode Medium of High-Current Glow Discharge. *Condensed Matter Nuclear Science*, 253-268.

Karimipourfard, M., Sina, S., Sadeghi, M., Safari, R., & Alavi, M. S. (2021). Assessment of PET scanner quantitative factors: Analysis and validation of GATE Monte Carlo simulation with experimental study. *Imaging Med., 13*(8).

Khattak, M. A., Borhana, A. A., Shafii, L. F., & Khan, R. (2018). MCNPX'S Water Equivalent Thickness Simulation of Material with Different Density via Proton Beam Irradiation. International Journal of Engineering & Technology. *7*(4.35), 678-682.

Manser, P., Peter, S., Volken, W., Zulliger, M. A., Laib, A., Koller, B., & Fix, M. K. (2017). Implementation and application of a Monte Carlo model for an in vivo micro computed tomography system. *Physica medica, 44*, 34-41.

Men, K., Dai, J.-R., Li, M.-H., Chen, X.-Y., Zhang, K., Tian, Y., . . . Xu, Y.-J. (2015). A Method to Improve Electron Density Measurement of Cone-Beam CT Using Dual Energy Technique. *BioMed research international, 2015*(1), 858907.

Michael, G. (2001). X-ray computed tomography. *Physics Education, 36*(6), 442-451.

Miller, D. L., Linet, M. S., Slovis, T. L., Kleinerman, R., Lee, C., Rajaraman, P., & Berrington de Gonzalez, A. (2012). Cancer risks associated with external radiation from diagnostic imaging procedures. *CA: a cancer journal for clinicians, 62*(2), 75-100.

Morrell, R. E., Rogers, A. T., Jobling, J. C., & Shakespeare, K. E. (2004). Barium enema: use of increased copper filtration to optimize dose and image quality. *The British Journal of Radiology, 77*(914), 116--122.

Moström, U., Bergström, K., Pech, P., & Ytterbergh, C. (1986). Deep-frozen biologic phantom for performance evaluation of CT scanners. *Journal of computer assisted tomography, 10*(6), 1016-1024.

Nakaya, H., Matsuno, T., Kamegawa, T., Hiraki, T., Inoue, T., Yanou, A., . . . Gofuku, A. (2014). CT phantom for development of robotic interventional radiology. *2014 IEEE/SICE International Symposium on System Integration* , 82-87.

Nickoloff, E. L., & Alderson, P. O. (2001, August 01). Radiation Exposures to Patients from CT: Reality, Public Perception, and Policy. *American Journal of Roentgenology, 177*(2), 285-287. doi:10.2214/AJR.177.2.1770285

Olerud, H. M., Olsen, J. B., & Skretting, A. (1999). An anthropomorphic phantom for receiver operating characteristic studies in CT imaging of liver lesions. *The British Journal of Radiology, 72*(853), 35-43.

Pelc, N. J. (2014). Recent and future directions in CT imaging. *Annals of biomedical engineering, 42*, 260-268.

Philips. (2021). *Brilliance iCT Family Version 4.1.10.* Netherlands: Philips Medical Systems Nederland B.V.

Plautz, T., Bashkirov,, V., Feng, V., Hurley, F, Johnson,, R. P., Leary, C., . . . Others. (2014). 200 MeV proton radiography studies with a hand phantom using a prototype proton CT scanner. *IEEE transactions on medical imaging, 33*(4), 875-881.

Rana, N., Rawat , D., Parmar, M., Dhawan, D. K., Bhati, A. K., & Mittal, B. R. (2015). Evaluation of external beam hardening filters on image quality of computed tomography and single photon emission computed tomography/computed tomography. *Journal of Medical Physics, 40*(4), 198-206. doi:10.4103/0971-6203.170790

Robert, J. J. (1988). A method for comparing beam-hardening filter materials for diagnostic radiology. *15*(4), 588-599.

Rogalla, P., Kloeters, C., & Hein, P. A. (2009, January). CT Technology Overview: 64-Slice and Beyond. *Radiologic Clinics of North America, 47*(1), 1-11.

Schmidt, C. W. (2012). CT scans: balancing health risks and medical benefits. *Environmental Health Perspectives, 120*(3), A119 - A121.

Schwarz, R. A., Carter, L. L., & Shrivastava, N. (1994). Creation of MCNP input files with a Visual Editor. No. WHC-SA--2019.

Schwarz, R., Carter, L. L., & Schwarz., A. (2005). *Modification to the Monte Carlo N-particle (MCNP) visual editor (MCNPVised) to read in computer aided design (CAD) files. No. DOE/ER/83844-1.* . Visual Editor Consultants.

Slovis, T. L. (2011, February 25). Where we were, what has changed, what needs doing:a decade of progress. *Pediatr Radiol, 41*(2), 456–460.

Smith, R. A., Andrews, K. S., Brooks, D., Fedewa, S. A., Manassaram-Baptiste, D., Saslow, D., . . . Wender , R. C. (2018). Cancer screening in the United States, 2018: a review of current American Cancer Society guidelines and current issues in cancer screening." 68.4 (2018):. *CA: A Cancer Journal for Clinicians, 68*(4), 297-316. doi:10.3322/caac.21446

Stegawski, M. A., & Schaumann, R. (1998). A new virtual-instrumentation-based experimenting environment for undergraduate laboratories with application in research and manufacturing. *IEEE Transactions on Instrumentation and Measurement, 47*(6), 1503-1506.

Szulc, M., & Judy, P. F. (1979). Effect of x-ray source filtration on dose and image performance of CT scanners. *Medical Physics, 6*(6), 479--486.

Thomas, A. M., Banerjee, A. K., & Busch, U. (2005). Classic Papers in Modern Diagnostic Radiology. *Berlin, Heidelberg: Springer Berlin Heidelberg.*, 253–330.

Tomography, ask Group on Control of Radiation Dose in Computed. (2000, January). Managing patient dose in computed tomography. A report of the International Commission on Radiological Protection. *Annals of the ICRP, 30*(4), 7-45. doi:10.1016/s0146-6453(01)00049-5

Vahid, M., Erfanian, V., & Ashoor., M. (2020). Estimation of optimized timely system matrix with improved image quality in iterative reconstruction algorithm: A simulation study. *Heliyon, 6*(1).

Villarraga-Gómez, H., Herazo, E. L., & Smith, S. T. (2019). X-ray computed tomography: from medical imaging to dimensional metrologY. *Precision Engineering, 60*, 544-569.

Ward, R. C., Yambert, M. W., Toedte, R. J., Munro, N. B., Easterly, C. E., Difilippo, E. P., & Stallings, D. C. (2000). Creating a human phantom for the virtual human program. *Medicine Meets Virtual Reality 2000*, 368-374.

Yang, Q., Fullagar, W. K., Myers, G. R., Latham, S. J., Varslot, T., Sheppard, A. P., & Kingston, A. M. (2020, October 10). X-ray attenuation models to account for beam hardening in computed tomography. *Applied optics, 59*(29), 9126-9136.

Yubao, Q., Weifeng, Q., Jiayi, L., Feng, G., & Qiang, Z. (2017). Application of Virtual Simulation and Computer Technology in Experiment and Practical Teaching. *Computer Science, Education*.

Zhao B. (2017). Optimization of tungsten-based beam-hardening filter for pediatric cardiac CT imaging using Monte Carlo simulations. *Physics in Medicine and Biology, 62* (6), 2256-2267.

Zheng, L. (2010). Application of Virtual Simulation Experiment in Experiment. *Physical Experiment of College*.

APPENDIX A

INPUT FILE FOR A CT SCANNER WITH ONLY AN INHERENT CONICAL FILTER (ABSENCE OF ADDITIONAL BEAM FILTER)

```
c
c
c MCNP input file of a Catphan phantom placed in a CT scanner,
written by Emmanuel Word Attaaku (STD ID:10934571)
c Purpose: Medical Physics Thesis at University of Ghana
c Thesis Topic: Computational Assessment of the influence of
Beam Hardening Filter on Image Quality and Patience Dose
c input file for a CT scanner with only an Inherent Conical
Filter
c
c input file for a CT scanner
c cell cards
1 1 -19.3 -23 $ Tungsten anode
2 2 -1.85 12 -13 -19 21 15 -16 :12 -13 -19 21 -17 18 &
     :-16 18 19 -20 12 -13 :-16 18 -21 22 12 -13 :22 &
     -20 11 -12 -15 17:22 -20 13 -14 -15 17 $ X ray tube envelope
made of Beryllium
3 0 12 -13 -15 17 -19 21 #1 $ Vacuum in X ray tube
4 3 -10.22 -5 8 9 -10 $ Collimator made of molybdenum
5 4 -2.7 -51 7 $ Additional filter
6 0 1 -2 -3 4 #1 #2 #3 #4 #5 #49 $ Gantry vacuum
7 5 -0.0029 -1 -3 4 #8 #9 #10 #11 #12 #13 #14 &
     #15 #16 #17 #18 #19 #20 #21 #22 #23 #24 #25 #26 #27 #28
#29 #30 #31 #32 &
     #33 #34 #35 #36 #37 #38 #39 #40 #41 #42 #43 #44 #45 #46
#47 #48 $ Air in gantry where patient is placed
8 6 -1.4 200 -100 147 -400 $ Cylinder
9 7 -1 -200 147 -400 #10 #11 #12 #13 #14 &
```

```
     #15 #16 #17 #18 #19 #20 #21 #22 #23 #24 #25 #26 #27 #28
#29 #30 #31 #32 &
     #33 #34 #35 #36 #37 #38 #39 #40 #41 #42 #43 #44 #45 #46
#47 #48 &
     vol=698.099784 $ Water fill
10 8 -1.15 -700 300 -146 vol=7.06858 $ Rod
11 8 -1.15 -800 300 -146 vol=2.01062 $ Rod
12 8 -1.15 -900 300 -146 vol=1.53938 $ Rod
13 8 -1.15 -110 300 -146 vol=1.36848 $ Rod
14 8 -1.15 -111 300 -146 vol=1.13097 $ Rod
15 8 -1.15 -112 300 -146 vol=7.85398E-01 $ Rod
16 8 -1.15 -113 300 -146 vol=5.02655E-01 $ Rod
17 8 -1.15 -114 300 -146 vol=2.82743E-01 $ Rod
18 8 -1.15 -115 300 -146 vol=1.25664E-01 $ Rod
19 8 -1.15 -116 300 -146 vol=7.06858 $ Rod
20 8 -1.15 -117 300 -146 vol=2.54469 $ Rod
21 8 -1.15 -118 300 -146 vol=2.01062 $ Rod
22 8 -1.15 -119 300 -146 vol=1.53938 $ Rod
23 8 -1.15 -120 300 -146 vol=1.13097 $ Rod
24 8 -1.15 -121 300 -146 vol=7.85398E-01 $ Rod
25 8 -1.15 -122 300 -146 vol=5.02655E-01 $ Rod
26 8 -1.15 -123 300 -146 vol=2.82743E-01 $ Rod
27 8 -1.15 -124 300 -146 vol=1.25664E-01 $ Rod
28 8 -1.15 -125 300 -146 vol=7.06858 $ Rod
29 8 -1.15 -126 300 -146 vol=2.54469 $ Rod
30 8 -1.15 -127 300 -146 vol=2.01062 $ Rod
31 8 -1.15 -128 300 -146 vol=1.53938 $ Rod
32 8 -1.15 -129 300 -146 vol=1.13097 $ Rod
33 8 -1.15 -130 300 -146 vol=7.85398E-01 $ Rod
34 8 -1.15 -131 300 -146 vol=5.02655E-01 $ Rod
35 8 -1.15 -132 300 -146 vol=2.82743E-01 $ Rod
36 8 -1.15 -133 300 -146 vol=1.25664E-01 $ Rod
```

```
37 8 -1.15 -134 300 -146 vol=2.54469 $ Rod
38 8 -1.15 -135 300 -146 vol=1.53938 $ Rod
39 8 -1.15 -136 300 -146 vol=7.85398E-01 $ Rod
40 8 -1.15 -137 300 -146 vol=2.82743E-01 $ Rod
41 8 -1.15 -138 300 -146 vol=2.54469 $ Rod
42 8 -1.15 -139 300 -146 vol=1.53938 $ Rod
43 8 -1.15 -140 300 -146 vol=7.85398E-01 $ Rod
44 8 -1.15 -141 300 -146 vol=2.82743E-01 $ Rod
45 8 -1.15 -142 300 -146 vol=2.54469 $ Rod
46 8 -1.15 -143 300 -146 vol=1.53938 $ Rod
47 8 -1.15 -144 300 -146 vol=7.85398E-01 $ Rod
48 8 -1.15 -145 300 -146 vol=2.82743E-01 $ Rod
49 4 -2.7 -5 609 -709 $ Inherent Aluminium filter
50 0 #1 #2 #3 #4 #5 #6 #7 #8 #9 #10 #11 #12 #13 #14 &
     #15 #16 #17 #18 #19 #20 #21 #22 #23 #24 #25 #26 #27 #28
#29 #30 #31 #32 &
     #33 #34 #35 #36 #37 #38 #39 #40 #41 #42 #43 #44 #45 #46
#47 #48 #49 $ Outside World

c surface card
1 cy 40 $ Gantry inner cylinder
2 cy 63 $ Gantry outer cylinder
3 py 20 $ First Plane truncating gantry cylinder
4 py -20 $ Second Plane truncating gantry cylinder
5 cz 13 $ Aluminium filter
51 k/z 0 0 42.7 1900 -1 $ Aluminium filter
c 6 pz 43 $ First Plane truncating aluminium filter
7 pz 42.7 $ Second Plane truncating aluminium filter
8 cz 0.4 $ Collimator opening
9 pz 44 $ First plane truncating the collimator
10 pz 44.5 $ Second plane truncating the collimator
11 pz 45 $ X-ray tube envelope first surface
```

```
12 pz 45.5 $ X-ray tube envelope second surface
13 pz 60 $ X-ray tube envelope third surface
14 pz 60.5 $ X-ray tube envelope fourth surface
15 py 7.5 $ X-ray tube envelope fifth surface
16 py 8 $ X-ray tube envelope sixth surface
17 py -7.5 $ X-ray tube envelope seventh surface
18 py -8 $ X-ray tube envelope eight surface
19 px 7.5 $ X-ray tube envelope ninth surface
20 px 8 $ X-ray tube envelope tenth surface
21 px -7.5 $ X-ray tube envelope eleventh surface
22 px -8 $ X-ray tube envelope twelve surface
23 trc 0.5 0 52.5 1.5 0 0 1.5 3 $ Truncated cone with base
radius at 0 0 52.5 and height 4 along the x axis and base/top
radius 3/1.5 resp
100 cz 7.5
200 cz 3.5
300 pz 0
400 pz 5
500 cz 2.7 $ outer radius of where rods will be
600 cz 1.3  $ Inner radius of where rods will be
700 c/z 2.6441 -0.50 0.75
609 pz 44.6 $ First Plane truncating Inherent aluminium filter
709 k/z 0 0 44.7 9900 -1 $ Second Plane truncating Inherent
aluminium filter
800 c/z 2.8942 0.6454 0.4
900 c/z 2.6227 1.3669 0.35
110 c/z 2.3337 1.9837 0.33
111 c/z 1.9 2.4959 0.3
112 c/z 1.49 2.8740 0.25
113 c/z 1.0559 3.0239 0.2
114 c/z 0.6843 3.1746 0.15
115 c/z 0.3105 3.2939 0.1
```

```
116 c/z -0.3621 2.6293 0.75
117 c/z -1.6304 2.4356 0.45
118 c/z -2.35 1.95 0.4
119 c/z -2.8249 1.3367 0.35
120 c/z -3.0951 0.739501 0.3
121 c/z -3.1810 0.1855 0.25
122 c/z -3.1511 -0.3070 0.2
123 c/z -3.0559 -0.7631 0.15
124 c/z -2.8180 -1.1842 0.1
125 c/z -1.93 -1.897 0.75
126 c/z -1.0 -2.7446 0.45
127 c/z -0.16 -2.88 0.4
128 c/z 0.5864 -2.7763 0.35
129 c/z 1.2317 -2.6558 0.3
130 c/z 1.7869 -2.3886 0.25
131 c/z 2.1329 -1.9314 0.2
132 c/z 2.4126 -1.6360 0.15
133 c/z 2.4747 -1.35190 0.1
134 c/z -0.9196 -0.9196 0.45
135 c/z -0.1817 -1.2537 0.35
136 c/z 0.4791 -1.1862 0.25
137 c/z 0.8942 -0.8867 0.15
138 c/z 1.32 -0.2146 0.45
139 c/z 1.0408 0.6102 0.35
140 c/z 0.6913 1.1768 0.25
141 c/z 0.3232 1.5248 0.15
142 c/z -0.4931 1.3671 0.45
143 c/z -1.2091 0.8684 0.35
144 c/z -1.5725 0.2173 0.25
145 c/z -1.3920 -0.2968 0.15
146 pz 4 $ Top of rods
147 pz -15 $ Bottom of container
```

```
c Data card
Mode P E
IMP:P 1 48r 0
IMP:E 1 48r 0
SDEF Pos= 0.94 0 50.4 ERG=10 PAR=3
f4:P 10 11 12 13 14 15 16 17 18 19 20 21 22 23 24 25 26 27 28
29 $ Rods flux
f24:P 30 31 32 33 34 35 36 37 38 39 40 41 42 43 44 45 46 47 48
$ Rods flux
f6:P 10 11 12 13 14 15 16 17 18 19 20 21 22 23 24 25 26 27 28
29 $ Rods flux
f26:P 30 31 32 33 34 35 36 37 38 39 40 41 42 43 44 45 46 47 48
$ Rods flux
E0 0.01 0.03 0.05 0.07 0.1 0.15 0.2 0.25 0.3 0.35 0.4 0.45 0.5
&
     0.55 0.6 0.65 0.7 $ ANSI/ANS6.1.11977 Energy bins of Photon
flux to Dose Conversion Factors From
f5:P 0 0 0 0.05 1 0 37 0.05 0 0 31 0.05
tmesh
rmesh31:P
cora31 -3.5 3.5
corb31 -3.5 3.5
corc31 4 63I 0
ENDMD
m1 73000 -1 $ Tungsten page 579 mcnpx manual
m2 4000 -1 $ Beryllium X-ray envelope
m3 42000 -1 $ Molybdenum collimator
m4 13000 -1 $ Aluminium filter
m5 7014 -0.78084 8016 -0.20947 18000 -0.009684 $ Air Elemental
Weight c c composition
m6 1001 -0.0816326 6012 -0.6122449 8016 -0.3265306 $ Container
```

```
m7 1001 -0.111898 8016 -0.888102 $ Water
m8 1001 -0.0816326 6012 -0.6122449 8016 -0.3265306 $ Rods
nps 400000
```

APPENDIX B

INPUT FILE FOR RECTANGULARLY-SHAPED ADDITIONAL ALUMINIUM BEAM HARDENING FILTER (AABHF) WHEN THE THICKNESS IS 0.53 mm

```
c
c
c
c MCNP input file of a Catphan phantom placed in a CT scanner,
written by Emmanuel Word Attaaku (STD ID:10934571)
c Purpose: Medical Physics Thesis at University of Ghana
c Thesis Topic: Computational Assessment of the influence of Beam
Hardening Filter on Image Quality and Patience Dose
c input file for an additional Aluminum Filter thickness 0.53 mm
for a CT scanner
c
c
c
c
c cell cards
1 1 -19.3 -23 $ Tungsten anode
2 2 -1.85 12 -13 -19 21 15 -16 :12 -13 -19 21 -17 18 &
     :-16 18 19 -20 12 -13 :-16 18 -21 22 12 -13 :22 &
     -20 11 -12 -15 17:22 -20 13 -14 -15 17 $ X ray tube envelope
made of Beryllium
3 0 12 -13 -15 17 -19 21 #1 $ Vacuum in X ray tube
4 3 -10.22 -5 8 9 -10 $ Collimator made of molybdenum
5 9 -2.7 -5 6 -7 $ Aluminium additional filter
6 0 1 -2 -3 4 #1 #2 #3 #4 #5 #49 $ Gantry vacuum
7 5 -0.0029 -1 -3 4 #8 #9 #10 #11 #12 #13 #14 &
     #15 #16 #17 #18 #19 #20 #21 #22 #23 #24 #25 #26 #27 #28 #29
#30 #31 #32 &
     #33 #34 #35 #36 #37 #38 #39 #40 #41 #42 #43 #44 #45 #46 #47
#48 $ Air in gantry where patient is placed
8 6 -1.4 200 -100 147 -400 $ Cylinder
9 7 -1 -200 147 -400 #10 #11 #12 #13 #14 &
     #15 #16 #17 #18 #19 #20 #21 #22 #23 #24 #25 #26 #27 #28 #29
#30 #31 #32 &
     #33 #34 #35 #36 #37 #38 #39 #40 #41 #42 #43 #44 #45 #46 #47
#48 $ Water fill
10 8 -1.15 -700 300 -146 vol=7.06858 $ Rod
11 8 -1.15 -800 300 -146 vol=2.01062 $ Rod
12 8 -1.15 -900 300 -146 vol=1.53938 $ Rod
13 8 -1.15 -110 300 -146 vol=1.36848 $ Rod
14 8 -1.15 -111 300 -146 vol=1.13097 $ Rod
```

```
15 8 -1.15 -112 300 -146 vol=0.785398 $ Rod
16 8 -1.15 -113 300 -146 vol=0.502655 $ Rod
17 8 -1.15 -114 300 -146 vol=0.282743 $ Rod
18 8 -1.15 -115 300 -146 vol=0.125664 $ Rod
19 8 -1.15 -116 300 -146 vol=7.06858 $ Rod
20 8 -1.15 -117 300 -146 vol=2.54469 $ Rod
21 8 -1.15 -118 300 -146 vol=2.01062 $ Rod
22 8 -1.15 -119 300 -146 vol=1.53938 $ Rod
23 8 -1.15 -120 300 -146 vol=1.13097 $ Rod
24 8 -1.15 -121 300 -146 vol=0.785398 $ Rod
25 8 -1.15 -122 300 -146 vol=0.502655 $ Rod
26 8 -1.15 -123 300 -146 vol=0.282743 $ Rod
27 8 -1.15 -124 300 -146 vol=0.125664 $ Rod
28 8 -1.15 -125 300 -146 vol=7.06858 $ Rod
29 8 -1.15 -126 300 -146 vol=2.54469 $ Rod
30 8 -1.15 -127 300 -146 vol=2.01062 $ Rod
31 8 -1.15 -128 300 -146 vol=1.53938 $ Rod
32 8 -1.15 -129 300 -146 vol=1.13097 $ Rod
33 8 -1.15 -130 300 -146 vol=0.785398 $ Rod
34 8 -1.15 -131 300 -146 vol=0.502655 $ Rod
35 8 -1.15 -132 300 -146 vol=0.282743 $ Rod
36 8 -1.15 -133 300 -146 vol=0.125664 $ Rod
37 8 -1.15 -134 300 -146 vol=2.54469 $ Rod
38 8 -1.15 -135 300 -146 vol=1.53938 $ Rod
39 8 -1.15 -136 300 -146 vol=0.785398 $ Rod
40 8 -1.15 -137 300 -146 vol=0.282743 $ Rod
41 8 -1.15 -138 300 -146 vol=2.54469 $ Rod
42 8 -1.15 -139 300 -146 vol=1.53938 $ Rod
43 8 -1.15 -140 300 -146 vol=0.785398 $ Rod
44 8 -1.15 -141 300 -146 vol=0.282743 $ Rod
45 8 -1.15 -142 300 -146 vol=2.54469 $ Rod
46 8 -1.15 -143 300 -146 vol=1.53938 $ Rod
47 8 -1.15 -144 300 -146 vol=0.785398 $ Rod
48 8 -1.15 -145 300 -146 vol=0.282743 $ Rod
49 4 -2.7 -5 609 -709 $ Inherent Aluminium filter
50 0 #1 #2 #3 #4 #5 #6 #7 #8 #9 #10 #11 #12 #13 #14 &
     #15 #16 #17 #18 #19 #20 #21 #22 #23 #24 #25 #26 #27 #28 #29
#30 #31 #32 &
     #33 #34 #35 #36 #37 #38 #39 #40 #41 #42 #43 #44 #45 #46 #47
#48 #49 $ Outside World

c surface card
1 cy 40 $ Gantry inner cylinder
2 cy 63 $ Gantry outer cylinder
3 py 20 $ First Plane truncating gantry cylinder
4 py -20 $ Second Plane truncating gantry cylinder
5 cz 13 $ Aluminum filter
```

```
6 pz 43 $ First Plane truncating Aluminium filter
7 pz 43.053 $ Second Plane truncating Aluminium filter
8 cz 0.4 $ Collimator opening
9 pz 44 $ First plane truncating the collimator
10 pz 44.5 $ Second plane truncating the collimator
11 pz 45.18 $ X-ray tube envelope first surface
12 pz 45.5 $ X-ray tube envelope second surface
13 pz 60 $ X-ray tube envelope third surface
14 pz 60.5 $ X-ray tube envelope fourth surface
15 py 7.5 $ X-ray tube envelope fifth surface
16 py 8 $ X-ray tube envelope sixth surface
17 py -7.5 $ X-ray tube envelope seventh surface
18 py -8 $ X-ray tube envelope eight surface
19 px 7.5 $ X-ray tube envelope ninth surface
20 px 8 $ X-ray tube envelope tenth surface
21 px -7.5 $ X-ray tube envelope eleventh surface
22 px -8 $ X-ray tube envelope twelve surface
23 trc 0.5 0 52.5 1.5 0 0 1.5 3 $ Truncated cone with base radius
at 0 0 52.5 and height 4 along the x axis and base/top radius 3/1.5
resp
100 cz 7.5
200 cz 3.5
300 pz 0
400 pz 5
500 cz 2.7 $ outer radius of where rods will be
600 cz 1.3 $ Inner radius of where rods will be
700 c/z 2.6441 -0.50 0.75
609 pz 44.6 $ First Plane truncating Inherent Aluminium filter
709 pz 45.08 $ Second Plane truncating Inherent Aluminium filter
800 c/z 2.8942 0.6454 0.4
900 c/z 2.6227 1.3669 0.35
110 c/z 2.3337 1.9837 0.33
111 c/z 1.9 2.4959 0.3
112 c/z 1.49 2.8740 0.25
113 c/z 1.0559 3.0239 0.2
114 c/z 0.6843 3.1746 0.15
115 c/z 0.3105 3.2939 0.1
116 c/z -0.3621 2.6293 0.75
117 c/z -1.6304 2.4356 0.45
118 c/z -2.35 1.95 0.4
119 c/z -2.8249 1.3367 0.35
120 c/z -3.0951 0.739501 0.3
121 c/z -3.1810 0.1855 0.25
122 c/z -3.1511 -0.3070 0.2
123 c/z -3.0559 -0.7631 0.15
124 c/z -2.8180 -1.1842 0.1
125 c/z -1.93 -1.897 0.75
```

```
126 c/z -1.0 -2.7446 0.45
127 c/z -0.16 -2.88 0.4
128 c/z 0.5864 -2.7763 0.35
129 c/z 1.2317 -2.6558 0.3
130 c/z 1.7869 -2.3886 0.25
131 c/z 2.1329 -1.9314 0.2
132 c/z 2.4126 -1.6360 0.15
133 c/z 2.4747 -1.35190 0.1
134 c/z -0.9196 -0.9196 0.45
135 c/z -0.1817 -1.2537 0.35
136 c/z 0.4791 -1.1862 0.25
137 c/z 0.8942 -0.8867 0.15
138 c/z 1.32 -0.2146 0.45
139 c/z 1.0408 0.6102 0.35
140 c/z 0.6913 1.1768 0.25
141 c/z 0.3232 1.5248 0.15
142 c/z -0.4931 1.3671 0.45
143 c/z -1.2091 0.8684 0.35
144 c/z -1.5725 0.2173 0.25
145 c/z -1.3920 -0.2968 0.15
146 pz 4 $ Top of rods
147 pz -15 $ Bottom of container

c Data card
Mode P E
IMP:P 1 48r 0
IMP:E 1 48r 0
SDEF Pos= 0.94 0 50.4 ERG=10 PAR=3
f4:P 10 11 12 13 14 15 16 17 18 19 20 21 22 23 24 25 26 27 28 29
$ Rods flux
f24:P 30 31 32 33 34 35 36 37 38 39 40 41 42 43 44 45 46 47 48 $
Rods flux
f6:P 10 11 12 13 14 15 16 17 18 19 20 21 22 23 24 25 26 27 28 29
$ Rods flux
f26:P 30 31 32 33 34 35 36 37 38 39 40 41 42 43 44 45 46 47 48 $
Rods flux
E0 0.01 0.015 0.02 0.03 0.04 0.05 0.06 0.08 0.1 0.15 0.2 0.3 0.4
0.5 0.6 &
     0.8 1 1.5 2 3 4 5 6 8 10 $ ICRP-21 Energy bins of Photon flux
to Dose Conversion Factors From MCNPX 2.7.0 Users Manual
f5:P 0 0 0 0.05 1 0 37 0.05 0 0 31 0.05
C E0 0.01 0.03 0.05 0.07 0.1 0.15 0.2 0.25 0.3 0.35 0.4 0.45 0.5
&
C     0.55 0.6 0.65 0.7 $ ANSI/ANS6.1.11977 Energy bins of Photon
flux to Dose Conversion Factors From MCNPX 2.7.0 Users Manual
c tmesh
c rmesh31:P
```

```
c cora31 -3.5 20I 3.5
c corb31 -3.5 20I 3.5
c corc31 4 20I 0
c ENDMD
m1 73000 -1 $ Tungsten page 579 mcnpx manual
m2 4000 -1 $ Beryllium X-ray envelope
m3 42000 -1 $ Molybdenum collimator
m4 13000 -1 $ Aluminum filter
m5 7014 -0.78084 8016 -0.20947 18000 -0.009684 $ Air Elemental
Weight c c composition
m6 1001 -0.0816326 6012 -0.6122449 8016 -0.3265306 $ Container
m7 1001 -0.111898 8016 -0.888102 $ Water
m8 1001 -0.0816326 6012 -0.6122449 8016 -0.3265306 $ Rods
m9 13000 -1 $ Aluminium filter material
nps 400000
```

APPENDIX C

INPUT FILE FOR CONICALLY-SHAPED ADDITIONAL ALUMINIUM BEAM HARDENING FILTER (AABHF) WHEN THE THICKNESS IS 0.53 mm

```
c input file for a CT scanner
c cell cards
1 1 -19.3 -23 $ Tungsten anode
2 2 -1.85 12 -13 -19 21 15 -16 :12 -13 -19 21 -17 18 &
     :-16 18 19 -20 12 -13 :-16 18 -21 22 12 -13 :22 &
     -20 11 -12 -15 17:22 -20 13 -14 -15 17 $ X ray tube envelope
made of Berryllium
3 0 12 -13 -15 17 -19 21 #1 $ Vacuum in X ray tube
4 3 -10.22 -5 8 9 -10 $ Collimator made of molybdenum
5 4 -2.7 -51 7 $ Additional filter
6 0 1 -2 -3 4 #1 #2 #3 #4 #5 #49 $ Gantry vacuum
7 5 -0.0029 -1 -3 4 #8 #9 #10 #11 #12 #13 #14 &
     #15 #16 #17 #18 #19 #20 #21 #22 #23 #24 #25 #26 #27 #28 #29
#30 #31 #32 &
     #33 #34 #35 #36 #37 #38 #39 #40 #41 #42 #43 #44 #45 #46 #47
#48 $ Air in gantry where patient is placed
8 6 -1.4 200 -100 147 -400 $ Cylinder
9 7 -1 -200 147 -400 #10 #11 #12 #13 #14 &
     #15 #16 #17 #18 #19 #20 #21 #22 #23 #24 #25 #26 #27 #28 #29
#30 #31 #32 &
     #33 #34 #35 #36 #37 #38 #39 #40 #41 #42 #43 #44 #45 #46 #47
#48 &
     vol=698.099784 $ Water fill
10 8 -1.15 -700 300 -146 vol=7.06858 $ Rod
11 8 -1.15 -800 300 -146 vol=2.01062 $ Rod
12 8 -1.15 -900 300 -146 vol=1.53938 $ Rod
13 8 -1.15 -110 300 -146 vol=1.36848 $ Rod
14 8 -1.15 -111 300 -146 vol=1.13097  $ Rod
```

```
15 8 -1.15 -112 300 -146 vol=7.85398E-01 $ Rod
16 8 -1.15 -113 300 -146 vol=5.02655E-01 $ Rod
17 8 -1.15 -114 300 -146 vol=2.82743E-01 $ Rod
18 8 -1.15 -115 300 -146 vol=1.25664E-01 $ Rod
19 8 -1.15 -116 300 -146 vol=7.06858 $ Rod
20 8 -1.15 -117 300 -146 vol=2.54469 $ Rod
21 8 -1.15 -118 300 -146 vol=2.01062 $ Rod
22 8 -1.15 -119 300 -146 vol=1.53938 $ Rod
23 8 -1.15 -120 300 -146 vol=1.13097 $ Rod
24 8 -1.15 -121 300 -146 vol=7.85398E-01 $ Rod
25 8 -1.15 -122 300 -146 vol=5.02655E-01 $ Rod
26 8 -1.15 -123 300 -146 vol=2.82743E-01 $ Rod
27 8 -1.15 -124 300 -146 vol=1.25664E-01 $ Rod
28 8 -1.15 -125 300 -146 vol=7.06858 $ Rod
29 8 -1.15 -126 300 -146 vol=2.54469 $ Rod
30 8 -1.15 -127 300 -146 vol=2.01062 $ Rod
31 8 -1.15 -128 300 -146 vol=1.53938 $ Rod
32 8 -1.15 -129 300 -146 vol=1.13097 $ Rod
33 8 -1.15 -130 300 -146 vol=7.85398E-01 $ Rod
34 8 -1.15 -131 300 -146 vol=5.02655E-01 $ Rod
35 8 -1.15 -132 300 -146 vol=2.82743E-01 $ Rod
36 8 -1.15 -133 300 -146 vol=1.25664E-01 $ Rod
37 8 -1.15 -134 300 -146 vol=2.54469 $ Rod
38 8 -1.15 -135 300 -146 vol=1.53938 $ Rod
39 8 -1.15 -136 300 -146 vol=7.85398E-01 $ Rod
40 8 -1.15 -137 300 -146 vol=2.82743E-01 $ Rod
41 8 -1.15 -138 300 -146 vol=2.54469 $ Rod
42 8 -1.15 -139 300 -146 vol=1.53938 $ Rod
43 8 -1.15 -140 300 -146 vol=7.85398E-01 $ Rod
44 8 -1.15 -141 300 -146 vol=2.82743E-01 $ Rod
45 8 -1.15 -142 300 -146 vol=2.54469 $ Rod
46 8 -1.15 -143 300 -146 vol=1.53938 $ Rod
```

```
47 8 -1.15 -144 300 -146 vol=7.85398E-01 $ Rod
48 8 -1.15 -145 300 -146 vol=2.82743E-01 $ Rod
49 4 -2.7 -5 609 -709 $ Inherent Aluminium filter
50 0 #1 #2 #3 #4 #5 #6 #7 #8 #9 #10 #11 #12 #13 #14 &
     #15 #16 #17 #18 #19 #20 #21 #22 #23 #24 #25 #26 #27 #28 #29
#30 #31 #32 &
     #33 #34 #35 #36 #37 #38 #39 #40 #41 #42 #43 #44 #45 #46 #47
#48 #49 $ Outside World

c surface card
1 cy 40 $ Gantry inner cylinder
2 cy 63 $ Gantry outer cylinder
3 py 20 $ First Plane truncating gantry cylinder
4 py -20 $ Second Plane truncating gantry cylinder
5 cz 13 $ Aluminium filter
51 k/z 0 0 42.753 60900 -1 $ Aluminium filter
c 6 pz 43 $ First Plane truncating aluminium filter
7 pz 42.7 $ Second Plane truncating aluminium filter
8 cz 0.4 $ Collimator opening
9 pz 44 $ First plane truncating the collimator
10 pz 44.5 $ Second plane truncating the collimator
11 pz 45 $ X-ray tube envelope first surface
12 pz 45.5 $ X-ray tube envelope second surface
13 pz 60 $ X-ray tube envelope third surface
14 pz 60.5 $ X-ray tube envelope fourth surface
15 py 7.5 $ X-ray tube envelope fifth surface
16 py 8 $ X-ray tube envelope sixth surface
17 py -7.5 $ X-ray tube envelope seventh surface
18 py -8 $ X-ray tube envelope eight surface
19 px 7.5 $ X-ray tube envelope ninth surface
20 px 8 $ X-ray tube envelope tenth surface
21 px -7.5 $ X-ray tube envelope eleventh surface
```

```
22 px -8 $ X-ray tube envelope twelve surface
23 trc 0.5 0 52.5 1.5 0 0 1.5 3 $ Truncated cone with base radius
at 0 0 52.5 and height 4 along the x axis and base/top radius 3/1.5
resp
100 cz 7.5
200 cz 3.5
300 pz 0
400 pz 5
500 cz 2.7 $ outer radius of where rods will be
600 cz 1.3  $ Inner radius of where rods will be
700 c/z 2.6441 -0.50 0.75
609 pz 44.6 $ First Plane truncating Inherent aluminium filter
709 k/z 0 0 44.7 9900 -1 $ Second Plane truncating Inherent
aluminium filter
800 c/z 2.8942 0.6454 0.4
900 c/z 2.6227 1.3669 0.35
110 c/z 2.3337 1.9837 0.33
111 c/z 1.9 2.4959 0.3
112 c/z 1.49 2.8740 0.25
113 c/z 1.0559 3.0239 0.2
114 c/z 0.6843 3.1746 0.15
115 c/z 0.3105 3.2939 0.1
116 c/z -0.3621 2.6293 0.75
117 c/z -1.6304 2.4356 0.45
118 c/z -2.35 1.95 0.4
119 c/z -2.8249 1.3367 0.35
120 c/z -3.0951 0.739501 0.3
121 c/z -3.1810 0.1855 0.25
122 c/z -3.1511 -0.3070 0.2
123 c/z -3.0559 -0.7631 0.15
124 c/z -2.8180 -1.1842 0.1
125 c/z -1.93 -1.897 0.75
```

```
126 c/z -1.0 -2.7446 0.45
127 c/z -0.16 -2.88 0.4
128 c/z 0.5864 -2.7763 0.35
129 c/z 1.2317 -2.6558 0.3
130 c/z 1.7869 -2.3886 0.25
131 c/z 2.1329 -1.9314 0.2
132 c/z 2.4126 -1.6360 0.15
133 c/z 2.4747 -1.35190 0.1
134 c/z -0.9196 -0.9196 0.45
135 c/z -0.1817 -1.2537 0.35
136 c/z 0.4791 -1.1862 0.25
137 c/z 0.8942 -0.8867 0.15
138 c/z 1.32 -0.2146 0.45
139 c/z 1.0408 0.6102 0.35
140 c/z 0.6913 1.1768 0.25
141 c/z 0.3232 1.5248 0.15
142 c/z -0.4931 1.3671 0.45
143 c/z -1.2091 0.8684 0.35
144 c/z -1.5725 0.2173 0.25
145 c/z -1.3920 -0.2968 0.15
146 pz 4 $ Top of rods
147 pz -15 $ Bottom of container

c Data card
Mode P E
IMP:P 1 48r 0
IMP:E 1 48r 0
SDEF Pos= 0.94 0 50.4 ERG=10 PAR=3
f4:P 10 11 12 13 14 15 16 17 18 19 20 21 22 23 24 25 26 27 28 29
$ Rods flux
f24:P 30 31 32 33 34 35 36 37 38 39 40 41 42 43 44 45 46 47 48 $
Rods flux
```

```
f6:P 10 11 12 13 14 15 16 17 18 19 20 21 22 23 24 25 26 27 28 29
$ Rods flux
f26:P 30 31 32 33 34 35 36 37 38 39 40 41 42 43 44 45 46 47 48 $
Rods flux
E0 0.01 0.03 0.05 0.07 0.1 0.15 0.2 0.25 0.3 0.35 0.4 0.45 0.5 &
     0.55 0.6 0.65 0.7 $ ANSI/ANS6.1.11977 Energy bins of Photon
flux to Dose Conversion Factors From
f5:P 0 0 0 0.05 1 0 37 0.05 0 0 31 0.05
tmesh
rmesh31:P
cora31 -3.5 3.5
corb31 -3.5 3.5
corc31 4 63I 0
ENDMD
m1 73000 -1 $ Tungsten page 579 mcnpx manual
m2 4000 -1 $ Beryllium X-ray envelope
m3 42000 -1 $ Molybdenum collimator
m4 13000 -1 $ Aluminium filter
m5 7014 -0.78084 8016 -0.20947 18000 -0.009684 $ Air Elemental
Weight c c composition
m6 1001 -0.0816326 6012 -0.6122449 8016 -0.3265306 $ Container
m7 1001 -0.111898 8016 -0.888102 $ Water
m8 1001 -0.0816326 6012 -0.6122449 8016 -0.3265306 $ Rods
nps 400000
```

APPENDIX D

INPUT FILE FOR RECTANGULARLY-SHAPED ADDITIONAL COPPER BEAM HARDENING FILTER (ACBHF) WHEN THE THICKNESS IS 0.15 mm

```
c

c

c
c MCNP input file of a Catphan phantom placed in a CT scanner,
written by Emmanuel Word Attaaku (STD ID:10934571)
c Purpose: Medical Physics Thesis at University of Ghana
c Thesis Topic: Computational Assessment of the influence of Beam
Hardening Filter on Image Quality and Patience Dose
c input file for additional Copper Filter of thickness 0.15 mm for
a CT scanner
c
c
c
c cell cards
1 1 -19.3 -23 $ Tungsten anode
2 2 -1.85 12 -13 -19 21 15 -16 :12 -13 -19 21 -17 18 &
     :-16 18 19 -20 12 -13 :-16 18 -21 22 12 -13 :22 &
     -20 11 -12 -15 17:22 -20 13 -14 -15 17 $ X ray tube envelope
made of Beryllium
3 0 12 -13 -15 17 -19 21 #1 $ Vacuum in X ray tube
4 3 -10.22 -5 8 9 -10 $ Collimator made of molybdenum
5 9 -8.96 -5 6 -7 $ Copper additional filter
6 0 1 -2 -3 4 #1 #2 #3 #4 #5 #49 $ Gantry vacuum
7 5 -0.0029 -1 -3 4 #8 #9 #10 #11 #12 #13 #14 &
     #15 #16 #17 #18 #19 #20 #21 #22 #23 #24 #25 #26 #27 #28 #29
#30 #31 #32 &
     #33 #34 #35 #36 #37 #38 #39 #40 #41 #42 #43 #44 #45 #46 #47
#48 $ Air in gantry where patient is placed
8 6 -1.4 200 -100 147 -400 $ Cylinder
9 7 -1 -200 147 -400 #10 #11 #12 #13 #14 &
     #15 #16 #17 #18 #19 #20 #21 #22 #23 #24 #25 #26 #27 #28 #29
#30 #31 #32 &
     #33 #34 #35 #36 #37 #38 #39 #40 #41 #42 #43 #44 #45 #46 #47
#48 $ Water fill
10 8 -1.15 -700 300 -146 vol=7.06858 $ Rod
11 8 -1.15 -800 300 -146 vol=2.01062 $ Rod
12 8 -1.15 -900 300 -146 vol=1.53938 $ Rod
13 8 -1.15 -110 300 -146 vol=1.36848 $ Rod
14 8 -1.15 -111 300 -146 vol=1.13097 $ Rod
15 8 -1.15 -112 300 -146 vol=0.785398 $ Rod
16 8 -1.15 -113 300 -146 vol=0.502655 $ Rod
17 8 -1.15 -114 300 -146 vol=0.282743 $ Rod
```

```
18 8 -1.15 -115 300 -146 vol=0.125664 $ Rod
19 8 -1.15 -116 300 -146 vol=7.06858 $ Rod
20 8 -1.15 -117 300 -146 vol=2.54469 $ Rod
21 8 -1.15 -118 300 -146 vol=2.01062 $ Rod
22 8 -1.15 -119 300 -146 vol=1.53938 $ Rod
23 8 -1.15 -120 300 -146 vol=1.13097 $ Rod
24 8 -1.15 -121 300 -146 vol=0.785398 $ Rod
25 8 -1.15 -122 300 -146 vol=0.502655 $ Rod
26 8 -1.15 -123 300 -146 vol=0.282743 $ Rod
27 8 -1.15 -124 300 -146 vol=0.125664 $ Rod
28 8 -1.15 -125 300 -146 vol=7.06858 $ Rod
29 8 -1.15 -126 300 -146 vol=2.54469 $ Rod
30 8 -1.15 -127 300 -146 vol=2.01062 $ Rod
31 8 -1.15 -128 300 -146 vol=1.53938 $ Rod
32 8 -1.15 -129 300 -146 vol=1.13097 $ Rod
33 8 -1.15 -130 300 -146 vol=0.785398 $ Rod
34 8 -1.15 -131 300 -146 vol=0.502655 $ Rod
35 8 -1.15 -132 300 -146 vol=0.282743 $ Rod
36 8 -1.15 -133 300 -146 vol=0.125664 $ Rod
37 8 -1.15 -134 300 -146 vol=2.54469 $ Rod
38 8 -1.15 -135 300 -146 vol=1.53938 $ Rod
39 8 -1.15 -136 300 -146 vol=0.785398 $ Rod
40 8 -1.15 -137 300 -146 vol=0.282743 $ Rod
41 8 -1.15 -138 300 -146 vol=2.54469 $ Rod
42 8 -1.15 -139 300 -146 vol=1.53938 $ Rod
43 8 -1.15 -140 300 -146 vol=0.785398 $ Rod
44 8 -1.15 -141 300 -146 vol=0.282743 $ Rod
45 8 -1.15 -142 300 -146 vol=2.54469 $ Rod
46 8 -1.15 -143 300 -146 vol=1.53938 $ Rod
47 8 -1.15 -144 300 -146 vol=0.785398 $ Rod
48 8 -1.15 -145 300 -146 vol=0.282743 $ Rod
49 4 -2.7 -5 609 -709 $ Inherent Aluminium filter
50 0 #1 #2 #3 #4 #5 #6 #7 #8 #9 #10 #11 #12 #13 #14 &
     #15 #16 #17 #18 #19 #20 #21 #22 #23 #24 #25 #26 #27 #28 #29
#30 #31 #32 &
     #33 #34 #35 #36 #37 #38 #39 #40 #41 #42 #43 #44 #45 #46 #47
#48 #49 $ Outside World

c surface card
1 cy 40 $ Gantry inner cylinder
2 cy 63 $ Gantry outer cylinder
3 py 20 $ First Plane truncating gantry cylinder
4 py -20 $ Second Plane truncating gantry cylinder
5 cz 13 $ Aluminium filter
6 pz 43 $ First Plane truncating copper filter
7 pz 43.015 $ Second Plane truncating copper filter
8 cz 0.4 $ Collimator opening
```

```
9 pz 44 $ First plane truncating the collimator
10 pz 44.5 $ Second plane truncating the collimator
11 pz 45.18 $ X-ray tube envelope first surface
12 pz 45.5 $ X-ray tube envelope second surface
13 pz 60 $ X-ray tube envelope third surface
14 pz 60.5 $ X-ray tube envelope fourth surface
15 py 7.5 $ X-ray tube envelope fifth surface
16 py 8 $ X-ray tube envelope sixth surface
17 py -7.5 $ X-ray tube envelope seventh surface
18 py -8 $ X-ray tube envelope eight surface
19 px 7.5 $ X-ray tube envelope ninth surface
20 px 8 $ X-ray tube envelope tenth surface
21 px -7.5 $ X-ray tube envelope eleventh surface
22 px -8 $ X-ray tube envelope twelve surface
23 trc 0.5 0 52.5 1.5 0 0 1.5 3 $ Truncated cone with base radius
at 0 0 52.5 and height 4 along the x axis and base/top radius 3/1.5
resp
100 cz 7.5
200 cz 3.5
300 pz 0
400 pz 5
500 cz 2.7 $ outer radius of where rods will be
600 cz 1.3  $ Inner radius of where rods will be
700 c/z 2.6441 -0.50 0.75
609 pz 44.6 $ First Plane truncating Inherent aluminium filter
709 pz 45.08 $ Second Plane truncating Inherent aluminium filter
800 c/z 2.8942 0.6454 0.4
900 c/z 2.6227 1.3669 0.35
110 c/z 2.3337 1.9837 0.33
111 c/z 1.9 2.4959 0.3
112 c/z 1.49 2.8740 0.25
113 c/z 1.0559 3.0239 0.2
114 c/z 0.6843 3.1746 0.15
115 c/z 0.3105 3.2939 0.1
116 c/z -0.3621 2.6293 0.75
117 c/z -1.6304 2.4356 0.45
118 c/z -2.35 1.95 0.4
119 c/z -2.8249 1.3367 0.35
120 c/z -3.0951 0.739501 0.3
121 c/z -3.1810 0.1855 0.25
122 c/z -3.1511 -0.3070 0.2
123 c/z -3.0559 -0.7631 0.15
124 c/z -2.8180 -1.1842 0.1
125 c/z -1.93 -1.897 0.75
126 c/z -1.0 -2.7446 0.45
127 c/z -0.16 -2.88 0.4
128 c/z 0.5864 -2.7763 0.35
```

```
129 c/z 1.2317 -2.6558 0.3
130 c/z 1.7869 -2.3886 0.25
131 c/z 2.1329 -1.9314 0.2
132 c/z 2.4126 -1.6360 0.15
133 c/z 2.4747 -1.35190 0.1
134 c/z -0.9196 -0.9196 0.45
135 c/z -0.1817 -1.2537 0.35
136 c/z 0.4791 -1.1862 0.25
137 c/z 0.8942 -0.8867 0.15
138 c/z 1.32 -0.2146 0.45
139 c/z 1.0408 0.6102 0.35
140 c/z 0.6913 1.1768 0.25
141 c/z 0.3232 1.5248 0.15
142 c/z -0.4931 1.3671 0.45
143 c/z -1.2091 0.8684 0.35
144 c/z -1.5725 0.2173 0.25
145 c/z -1.3920 -0.2968 0.15
146 pz 4 $ Top of rods
147 pz -15 $ Bottom of container

c Data card
Mode P E
IMP:P 1 48r 0
IMP:E 1 48r 0
SDEF Pos= 0.94 0 50.4 ERG=10 PAR=3
f4:P 10 11 12 13 14 15 16 17 18 19 20 21 22 23 24 25 26 27 28 29
$ Rods flux
f24:P 30 31 32 33 34 35 36 37 38 39 40 41 42 43 44 45 46 47 48 $
Rods flux
f6:P 10 11 12 13 14 15 16 17 18 19 20 21 22 23 24 25 26 27 28 29
$ Rods flux
f26:P 30 31 32 33 34 35 36 37 38 39 40 41 42 43 44 45 46 47 48 $
Rods flux
E0 0.01 0.015 0.02 0.03 0.04 0.05 0.06 0.08 0.1 0.15 0.2 0.3 0.4
0.5 0.6 &
     0.8 1 1.5 2 3 4 5 6 8 10 $ ICRP-21 Energy bins of Photon flux
to Dose Conversion Factors From MCNPX 2.7.0 Users Manual
f5:P 0 0 0 0.05 1 0 37 0.05 0 0 31 0.05
C E0 0.01 0.03 0.05 0.07 0.1 0.15 0.2 0.25 0.3 0.35 0.4 0.45 0.5
&
C     0.55 0.6 0.65 0.7 $ ANSI/ANS6.1.11977 Energy bins of Photon
flux to Dose Conversion Factors From MCNPX 2.7.0 Users Manual
tmesh
rmesh31:P
cora31 -3.5 20I 3.5
corb31 -3.5 20I 3.5
corc31 4 20I 0
```

```
ENDMD
m1 73000 -1 $ Tungsten page 579 mcnpx manual
m2 4000 -1 $ Beryllium X-ray envelope
m3 42000 -1 $ Molybdenum collimator
m4 13000 -1 $ Aluminum filter
m5 7014 -0.78084 8016 -0.20947 18000 -0.009684 $ Air Elemental
Weight c c composition
m6 1001 -0.0816326 6012 -0.6122449 8016 -0.3265306 $ Container
m7 1001 -0.111898 8016 -0.888102 $ Water
m8 1001 -0.0816326 6012 -0.6122449 8016 -0.3265306 $ Rods
M9 23000 -1 $ Copper filter material
nps 400000
```

APPENDIX E

INPUT FILE FOR CONICALLY-SHAPED ADDITIONAL COPPER BEAM HARDENING FILTER (AABHF) WHEN THE THICKNESS IS 0.15 mm

```
c
c
c MCNP input file of a Catphan phantom placed in a CT scanner,
written by Emmanuel Word Attaaku (STD ID:10934571)
c Purpose: Medical Physics Thesis at University of Ghana
c Thesis Topic: Computational Assessment of the influence of Beam
Hardening Filter on Image Quality and Patience Dose
c input file for additional conical Copper Filter of thickness
0.015 cm for a CT scanner
c
c input file for a CT scanner
c cell cards
1 1 -19.3 -23 $ Tungsten anode
2 2 -1.85 12 -13 -19 21 15 -16 :12 -13 -19 21 -17 18 &
     :-16 18 19 -20 12 -13 :-16 18 -21 22 12 -13 :22 &
     -20 11 -12 -15 17:22 -20 13 -14 -15 17 $ X ray tube envelope
made of Beryllium
3 0 12 -13 -15 17 -19 21 #1 $ Vacuum in X ray tube
4 3 -10.22 -5 8 9 -10 $ Collimator made of molybdenum
5 4 -8.96 -51 7 $ Additional filter
6 0 1 -2 -3 4 #1 #2 #3 #4 #5 #49 $ Gantry vacuum
7 5 -0.0029 -1 -3 4 #8 #9 #10 #11 #12 #13 #14 &
     #15 #16 #17 #18 #19 #20 #21 #22 #23 #24 #25 #26 #27 #28 #29
#30 #31 #32 &
     #33 #34 #35 #36 #37 #38 #39 #40 #41 #42 #43 #44 #45 #46 #47
#48 $ Air in gantry where patient is placed
8 6 -1.4 200 -100 147 -400 $ Cylinder
9 7 -1 -200 147 -400 #10 #11 #12 #13 #14 &
     #15 #16 #17 #18 #19 #20 #21 #22 #23 #24 #25 #26 #27 #28 #29
#30 #31 #32 &
     #33 #34 #35 #36 #37 #38 #39 #40 #41 #42 #43 #44 #45 #46 #47
#48 &
     vol=698.099784 $ Water fill
10 8 -1.15 -700 300 -146 vol=7.06858 $ Rod
11 8 -1.15 -800 300 -146 vol=2.01062 $ Rod
12 8 -1.15 -900 300 -146 vol=1.53938 $ Rod
13 8 -1.15 -110 300 -146 vol=1.36848 $ Rod
14 8 -1.15 -111 300 -146 vol=1.13097 $ Rod
15 8 -1.15 -112 300 -146 vol=7.85398E-01 $ Rod
16 8 -1.15 -113 300 -146 vol=5.02655E-01 $ Rod
17 8 -1.15 -114 300 -146 vol=2.82743E-01 $ Rod
18 8 -1.15 -115 300 -146 vol=1.25664E-01 $ Rod
19 8 -1.15 -116 300 -146 vol=7.06858 $ Rod
```

```
20 8 -1.15 -117 300 -146 vol=2.54469 $ Rod
21 8 -1.15 -118 300 -146 vol=2.01062 $ Rod
22 8 -1.15 -119 300 -146 vol=1.53938 $ Rod
23 8 -1.15 -120 300 -146 vol=1.13097 $ Rod
24 8 -1.15 -121 300 -146 vol=7.85398E-01 $ Rod
25 8 -1.15 -122 300 -146 vol=5.02655E-01 $ Rod
26 8 -1.15 -123 300 -146 vol=2.82743E-01 $ Rod
27 8 -1.15 -124 300 -146 vol=1.25664E-01 $ Rod
28 8 -1.15 -125 300 -146 vol=7.06858 $ Rod
29 8 -1.15 -126 300 -146 vol=2.54469 $ Rod
30 8 -1.15 -127 300 -146 vol=2.01062 $ Rod
31 8 -1.15 -128 300 -146 vol=1.53938 $ Rod
32 8 -1.15 -129 300 -146 vol=1.13097 $ Rod
33 8 -1.15 -130 300 -146 vol=7.85398E-01 $ Rod
34 8 -1.15 -131 300 -146 vol=5.02655E-01 $ Rod
35 8 -1.15 -132 300 -146 vol=2.82743E-01 $ Rod
36 8 -1.15 -133 300 -146 vol=1.25664E-01 $ Rod
37 8 -1.15 -134 300 -146 vol=2.54469 $ Rod
38 8 -1.15 -135 300 -146 vol=1.53938 $ Rod
39 8 -1.15 -136 300 -146 vol=7.85398E-01 $ Rod
40 8 -1.15 -137 300 -146 vol=2.82743E-01 $ Rod
41 8 -1.15 -138 300 -146 vol=2.54469 $ Rod
42 8 -1.15 -139 300 -146 vol=1.53938 $ Rod
43 8 -1.15 -140 300 -146 vol=7.85398E-01 $ Rod
44 8 -1.15 -141 300 -146 vol=2.82743E-01 $ Rod
45 8 -1.15 -142 300 -146 vol=2.54469 $ Rod
46 8 -1.15 -143 300 -146 vol=1.53938 $ Rod
47 8 -1.15 -144 300 -146 vol=7.85398E-01 $ Rod
48 8 -1.15 -145 300 -146 vol=2.82743E-01 $ Rod
49 4 -2.7 -5 609 -709 $ Inherent Aluminum filter
50 0 #1 #2 #3 #4 #5 #6 #7 #8 #9 #10 #11 #12 #13 #14 &
     #15 #16 #17 #18 #19 #20 #21 #22 #23 #24 #25 #26 #27 #28 #29
#30 #31 #32 &
     #33 #34 #35 #36 #37 #38 #39 #40 #41 #42 #43 #44 #45 #46 #47
#48 #49 $ Outside World

c surface card
1 cy 40 $ Gantry inner cylinder
2 cy 63 $ Gantry outer cylinder
3 py 20 $ First Plane truncating gantry cylinder
4 py -20 $ Second Plane truncating gantry cylinder
5 cz 20 $ Cupper filter
51 k/z 0 0 42.715 1800900 -1 $ Copper filter
c 6 pz 43 $ First Plane truncating aluminium filter
7 pz 42.7 $ Second Plane truncating aluminium filter
8 cz 0.4 $ Collimator opening
9 pz 44 $ First plane truncating the collimator
```

```
10 pz 44.5 $ Second plane truncating the collimator
11 pz 45 $ X-ray tube envelope first surface
12 pz 45.5 $ X-ray tube envelope second surface
13 pz 60 $ X-ray tube envelope third surface
14 pz 60.5 $ X-ray tube envelope fourth surface
15 py 7.5 $ X-ray tube envelope fifth surface
16 py 8 $ X-ray tube envelope sixth surface
17 py -7.5 $ X-ray tube envelope seventh surface
18 py -8 $ X-ray tube envelope eight surface
19 px 7.5 $ X-ray tube envelope ninth surface
20 px 8 $ X-ray tube envelope tenth surface
21 px -7.5 $ X-ray tube envelope eleventh surface
22 px -8 $ X-ray tube envelope twelve surface
23 trc 0.5 0 52.5 1.5 0 0 1.5 3 $ Truncated cone with base radius
at 0 0 52.5 and height 4 along the x axis and base/top radius 3/1.5
resp
100 cz 7.5
200 cz 3.5
300 pz 0
400 pz 5
500 cz 2.7 $ outer radius of where rods will be
600 cz 1.3  $ Inner radius of where rods will be
700 c/z 2.6441 -0.50 0.75
609 pz 44.6 $ First Plane truncating Inherent aluminium filter
709  k/z  0  0  44.7  9900  -1  $  Second  Plane  truncating  Inherent
aluminium filter
800 c/z 2.8942 0.6454 0.4
900 c/z 2.6227 1.3669 0.35
110 c/z 2.3337 1.9837 0.33
111 c/z 1.9 2.4959 0.3
112 c/z 1.49 2.8740 0.25
113 c/z 1.0559 3.0239 0.2
114 c/z 0.6843 3.1746 0.15
115 c/z 0.3105 3.2939 0.1
116 c/z -0.3621 2.6293 0.75
117 c/z -1.6304 2.4356 0.45
118 c/z -2.35 1.95 0.4
119 c/z -2.8249 1.3367 0.35
120 c/z -3.0951 0.739501 0.3
121 c/z -3.1810 0.1855 0.25
122 c/z -3.1511 -0.3070 0.2
123 c/z -3.0559 -0.7631 0.15
124 c/z -2.8180 -1.1842 0.1
125 c/z -1.93 -1.897 0.75
126 c/z -1.0 -2.7446 0.45
127 c/z -0.16 -2.88 0.4
128 c/z 0.5864 -2.7763 0.35
```

```
129 c/z 1.2317 -2.6558 0.3
130 c/z 1.7869 -2.3886 0.25
131 c/z 2.1329 -1.9314 0.2
132 c/z 2.4126 -1.6360 0.15
133 c/z 2.4747 -1.35190 0.1
134 c/z -0.9196 -0.9196 0.45
135 c/z -0.1817 -1.2537 0.35
136 c/z 0.4791 -1.1862 0.25
137 c/z 0.8942 -0.8867 0.15
138 c/z 1.32 -0.2146 0.45
139 c/z 1.0408 0.6102 0.35
140 c/z 0.6913 1.1768 0.25
141 c/z 0.3232 1.5248 0.15
142 c/z -0.4931 1.3671 0.45
143 c/z -1.2091 0.8684 0.35
144 c/z -1.5725 0.2173 0.25
145 c/z -1.3920 -0.2968 0.15
146 pz 4 $ Top of rods
147 pz -15 $ Bottom of container

c Data card
Mode P E
IMP:P 1 48r 0
IMP:E 1 48r 0
SDEF Pos= 0.94 0 50.4 ERG=10 PAR=3
f4:P 10 11 12 13 14 15 16 17 18 19 20 21 22 23 24 25 26 27 28 29
$ Rods flux
f24:P 30 31 32 33 34 35 36 37 38 39 40 41 42 43 44 45 46 47 48 $
Rods flux
f6:P 10 11 12 13 14 15 16 17 18 19 20 21 22 23 24 25 26 27 28 29
$ Rods flux
f26:P 30 31 32 33 34 35 36 37 38 39 40 41 42 43 44 45 46 47 48 $
Rods flux
E0 0.01 0.03 0.05 0.07 0.1 0.15 0.2 0.25 0.3 0.35 0.4 0.45 0.5 &
     0.55 0.6 0.65 0.7 $ ANSI/ANS6.1.11977 Energy bins of Photon
flux to Dose Conversion Factors From
f5:P 0 0 0 0.05 1 0 37 0.05 0 0 31 0.05
tmesh
rmesh31:P
cora31 -3.5 3.5
corb31 -3.5 3.5
corc31 4 63I 0
ENDMD
m1 73000 -1 $ Tungsten page 579 mcnpx manual
m2 4000 -1 $ Beryllium X-ray envelope
m3 42000 -1 $ Molybdenum collimator
m4 20000 -1 $ Copper filter
```

```
m5  7014  -0.78084  8016  -0.20947  18000  -0.009684  $  Air  Elemental
Weight c c composition
m6 1001 -0.0816326 6012 -0.6122449 8016 -0.3265306 $ Container
m7 1001 -0.111898 8016 -0.888102 $ Water
m8 1001 -0.0816326 6012 -0.6122449 8016 -0.3265306 $ Rods
nps 400000
```

APPENDIX F

Table 4.3: Representation of the radiation dose to cells of the Catphan phantom when filter was rectangularly-shaped

ID	CELLS	RADIATION DOSE EXPOSED TO RODS / CELLS OF THE CATPHAN PHANTOM (MeV/particle.second)				
		BHF Al1 0.5 mm	BHF Al2 1.06 mm	BHF Al3 2.6 mm	BHF Al4 3.03 mm	BHF Al5 4.14 mm
1.	10	8.5971E-07	8.5564E-07	8.3057E-07	1.1978E-06	8.1132E-07
2.	11	6.4145E-07	6.4278E-07	6.1624E-07	6.5378E-07	5.8327E-07
3.	12	1.4700E-06	1.5829E-06	1.6348E-06	1.6505E-06	1.5990E-06
4.	13	7.1938E-07	7.3034E-07	6.5812E-07	6.8351E-07	6.9141E-07
5.	14	1.1155E-06	9.7073E-07	1.2162E-06	1.2225E-06	1.2902E-06
6.	15	2.3166E-06	2.1812E-06	1.7750E-06	1.7694E-06	1.7865E-06
7.	16	1.8539E-06	1.8726E-06	1.7835E-06	1.7879E-06	1.8286E-06
8.	17	5.4822E-07	5.5946E-07	6.1239E-07	6.0180E-07	5.8244E-07
9.	18	5.1065E-06	5.6647E-06	5.6305E-06	5.6386E-06	5.6624E-06
10.	19	7.7178E-07	7.9716E-07	7.6459E-07	7.6079E-07	6.2238E-07
11.	20	9.6543E-07	9.2253E-07	9.6615E-07	9.4591E-07	1.0170E-06
12.	21	1.5475E-06	1.5830E-06	1.6198E-06	1.5982E-06	1.5284E-06
13.	22	5.7499E-07	5.8393E-07	5.8684E-07	8.3910E-07	7.8457E-07
14.	23	5.3147E-07	4.6702E-07	5.7204E-07	5.8690E-07	5.1056E-07
15.	24	4.1785E-07	4.3859E-07	4.1076E-07	4.2149E-07	4.5312E-07
16.	25	6.5389E-07	8.0964E-07	6.5712E-07	6.6629E-07	6.4975E-07

ID	CELLS	RADIATION DOSE EXPOSED TO RODS / CELLS OF THE CATPHAN PHANTOM (MeV/particle.second)				
		BHF Al1 0.5 mm	BHF Al2 1.06 mm	BHF Al3 2.6 mm	BHF Al4 3.03 mm	BHF Al5 4.14 mm
17.	26	9.7531E-07	1.0154E-06	1.0071E-06	1.0058E-06	9.6576E-07
18.	27	2.1339E-07	1.5097E-07	5.3854E-07	1.0743E-07	5.5681E-07
19.	28	6.7355E-07	8.1937E-07	6.3966E-07	6.6228E-07	5.9123E-07
20.	29	3.8283E-07	3.9350E-07	4.4272E-07	4.2848E-07	5.6129E-07
21.	30	2.9257E-07	3.7907E-07	4.3036E-07	2.6538E-07	4.5239E-07
22.	31	6.9563E-07	5.4285E-07	5.1973E-07	5.0673E-07	3.0511E-07
23.	32	9.5676E-07	9.3015E-07	9.1634E-07	9.2607E-07	8.9872E-07
24.	33	3.1106E-07	2.9885E-07	3.5842E-07	3.5969E-07	3.5575E-07
25.	34	1.2196E-06	1.2300E-06	1.2727E-06	1.3011E-06	1.2976E-06
26.	35	3.1742E-07	3.8554E-07	1.3902E-07	1.3405E-07	1.3683E-07
27.	36	9.5692E-09	1.5513E-08	4.9323E-08	1.5513E-08	1.5513E-08
28.	37	7.5007E-07	6.2814E-07	6.1780E-07	6.0519E-07	6.2217E-07
29.	38	5.6835E-07	5.9383E-07	7.2284E-07	7.0412E-07	9.2799E-07
30.	39	1.4559E-06	1.5885E-06	1.6258E-06	1.6421E-06	2.0551E-06
31.	40	1.8813E-07	1.1426E-07	1.0887E-07	1.2884E-07	4.5875E-07
32.	41	1.4792E-06	1.3757E-06	1.6729E-06	1.6362E-06	1.2969E-06
33.	42	1.4850E-06	1.4479E-06	9.7982E-07	1.4762E-06	1.4638E-06
34.	43	2.1595E-07	2.1648E-07	2.1487E-07	2.3442E-07	2.1859E-07

ID	CELLS	RADIATION DOSE EXPOSED TO RODS / CELLS OF THE CATPHAN PHANTOM (MeV/particle.second)				
		BHF Al1 0.5 mm	**BHF Al2 1.06 mm**	**BHF Al3 2.6 mm**	**BHF Al4 3.03 mm**	**BHF Al5 4.14 mm**
45.	44	1.0209E-06	1.0035E-06	1.0051E-06	1.0109E-06	1.1952E-06
36.	45	4.4265E-07	3.7454E-07	4.9862E-07	5.0377E-07	4.1502E-07
37.	46	2.3465E-06	2.3625E-06	2.3749E-06	2.3587E-06	2.3146E-06
38.	47	1.1859E-06	1.2026E-06	1.1854E-06	1.2021E-06	1.1650E-06
39.	48	1.1978E-06	1.2062E-06	1.2283E-06	1.2156E-06	1.2210E-06

APPENDIX G

Table 4.4: Representation of the radiation dose exposed to the rod of the Catphan phantom when filters was conically-shaped.

SN	CELL	ENERGY EXPOSED TO CELLS OF THE CATPHAN PHANTOM (MeV/particle.second)				
		CBHF Al1 0.53 mm	CBHF Al2 1.06 mm	CBHF Al3 2.60 mm	CBHF Al4 3.08 mm	CBHF Al5 4.14 mm
1.	10	3.2055E-07	3.6601E-07	3.5675E-07	3.4592E-07	3.2006E-07
2.	11	3.9585E-07	3.9821E-07	3.8246E-07	3.9403E-07	3.6115E-07
3.	12	4.0785E-07	3.6311E-07	4.5990E-07	3.8406E-07	4.6916E-07
4.	13	4.6763E-07	4.5148E-07	4.6955E-07	4.1232E-07	4.2779E-07
5.	14	4.1312E-07	2.7146E-07	3.2100E-07	2.1869E-07	2.7474E-07
6.	15	1.9568E-07	2.5545E-07	3.2186E-07	2.4878E-07	3.5083E-07
7.	16	3.5096E-07	3.2306E-07	4.0399E-07	3.9223E-07	3.6776E-07
8.	17	2.2128E-07	9.9337E-08	8.7925E-08	2.8692E-07	1.3686E-07
9.	18	1.5574E-06	1.5261E-06	1.5355E-06	1.6071E-06	1.5919E-06
10.	19	4.3425E-07	4.1706E-07	3.9101E-07	3.8059E-07	3.9223E-07
11.	20	2.9481E-07	2.4845E-07	2.6929E-07	2.6734E-07	2.7914E-07
12.	21	2.9325E-07	2.8119E-07	2.9916E-07	3.4503E-07	3.7237E-07
13.	22	3.7933E-07	3.8053E-07	2.4302E-07	2.7549E-07	2.8558E-07
14.	23	4.7387E-07	5.0700E-07	5.1491E-07	4.2766E-07	4.6418E-07
15.	24	6.5672E-07	4.4418E-07	3.7155E-07	3.1812E-07	2.8339E-07
16.	25	3.4725E-07	3.3400E-07	3.3777E-07	1.9777E-07	2.3466E-07
17.	26	1.9941E-07	1.8469E-07	1.1780E-07	1.9133E-07	2.2341E-07
18.	27	1.2411E-07	5.1314E-07	5.1143E-07	3.6053E-07	3.6053E-07
19	28	3.6940E-07	3.7152E-07	3.9628E-07	3.9961E-07	3.9001E-07
20.	29	3.9370E-07	5.0411E-07	5.3674E-07	4.6193E-07	4.1493E-07
21.	30	4.2388E-07	4.0803E-07	3.1525E-07	3.4922E-07	3.0873E-07
22.	31	4.9990E-07	3.4526E-07	2.6630E-07	4.6982E-07	3.3890E-07
23.	32	4.4211E-07	4.5341E-07	5.2574E-07	3.1447E-07	4.4463E-07
24.	33	2.6193E-07	3.0489E-07	4.3367E-07	3.7718E-07	3.8368E-07

SN	CELL	ENERGY EXPOSED TO CELLS OF THE CATPHAN PHANTOM (MeV/particle.second)				
		CBHF Al1 0.53 mm	**CBHF Al2 1.06 mm**	**CBHF Al3 2.60 mm**	**CBHF Al4 3.08 mm**	**CBHF Al5 4.14 mm**
25.	34	5.0510E-07	1.9306E-07	2.7105E-07	1.2194E-07	1.4577E-07
26.	35	2.0414E-07	2.4762E-07	1.6458E-07	3.0112E-07	3.9853E-07
27.	36	7.8550E-07	7.9813E-07	8.0470E-07	7.9038E-07	7.9336E-07
28.	37	2.4920E-07	2.3538E-07	2.5536E-07	3.0694E-07	2.7056E-07
29.	38	1.2906E-07	1.5478E-07	2.5023E-07	1.1547E-07	9.9080E-08
30.	39	3.3751E-07	3.3249E-07	3.4607E-07	3.2938E-07	3.3685E-07
31.	40	2.3856E-07	2.1602E-07	2.1825E-07	2.4323E-07	2.2490E-07
32.	41	3.4406E-07	3.1251E-07	3.3732E-07	2.9400E-07	2.7156E-07
33.	42	3.9388E-07	4.2738E-07	2.9431E-07	3.9039E-07	3.4060E-07
34.	43	4.3247E-07	3.4779E-07	3.6233E-07	3.9102E-07	3.8336E-07
45.	44	4.0100E-07	3.7292E-07	6.7332E-07	3.9186E-07	3.9465E-07
36.	45	4.0026E-07	4.0389E-07	3.8038E-07	5.3210E-07	4.4313E-07
37.	46	6.2170E-07	5.8742E-07	5.3670E-07	5.2416E-07	5.0707E-07
38.	47	5.2928E-07	3.4873E-07	3.4990E-07	3.5095E-07	3.4837E-07
39.	48	3.2653E-07	2.7620E-07	4.7777E-07	2.4811E-07	3.0001E-07
40.	SUM TOTAL	**1.5822E-05**	**1.5006E-05**	**1.5591E-05**	**1.4757E-05**	**1.4734E-05**
41.	MEAN DOSE	**4.0570E-07**	**3.8477E-07**	**3.9977E-07**	**3.7839E-07**	**3.7781E-07**

APPENDIX H

Table 4.5: Radiation dose output results of the cells of the virtual Catphan phantom when filter is rectangularly shaped

ID	CELLS	RADIATION DOSE (MeV) TO RODS / CELLS OF THE CATPHAN PHANTOM (MeV/particle.second)						
		BHF Cu1	BHF Cu2	BHF Cu3	BHF CU4	BHF Cu5	BHF Cu6	BHF Cu7
		0.15 mm	0.28 mm	0.48 mm	0.68 mm	0.75 mm	1.40 mm	1.61 mm
1.	10	8.39239E-07	7.51505E-07	8.39966E-07	8.36396E-07	9.20006E-07	2.97324E-08	7.75827E-07
2.	11	6.46189E-07	6.72123E-07	8.23698E-07	5.52958E-07	8.48154E-07	9.52976E-09	6.65182E-07
3.	12	1.41306E-06	1.38912E-06	1.55562E-06	1.56537E-06	1.59639E-06	1.88435E-08	1.37087E-06
4.	13	7.15133E-07	7.19090E-07	7.13032E-07	7.24751E-07	6.40770E-07	2.08825E-08	6.19748E-07
5.	14	9.97013E-07	9.95702E-07	1.00045E-06	1.13222E-06	1.06078E-06	3.48360E-08	1.08990E-06
6.	15	2.18750E-06	2.18480E-06	2.21484E-06	2.16060E-06	2.10651E-06	3.70152E-08	1.89015E-06
7.	16	1.84218E-06	1.85439E-06	1.90299E-06	1.84120E-06	1.82209E-06	2.46093E-08	1.75219E-06
8.	17	5.40733E-07	5.44138E-07	3.81765E-07	6.04620E-07	4.75656E-07	9.55094E-09	3.60415E-07
9.	18	5.73748E-06	5.43965E-06	5.20526E-06	5.63543E-06	5.64653E-06	3.29729E-08	5.61387E-06
10.	19	7.14827E-07	7.27925E-07	7.89030E-07	6.97269E-07	7.21018E-07	1.27202E-08	6.38430E-07
11.	20	8.96106E-07	1.03420E-06	8.71727E-07	9.91702E-07	9.58473E-07	2.52129E-08	7.82498E-07
12.	21	1.36361E-06	1.35378E-06	1.36299E-06	1.25993E-06	1.33562E-06	2.15661E-08	1.42892E-06
13.	22	7.05228E-07	7.10079E-07	5.99980E-07	8.46834E-07	6.67285E-07	2.62032E-08	8.85524E-07
14.	23	5.24299E-07	5.25511E-07	5.84518E-07	7.77107E-07	7.52974E-07	4.58661E-08	8.27095E-07
15.	24	4.07090E-07	4.04296E-07	5.32437E-07	4.25145E-07	4.52681E-07	2.47655E-08	4.40579E-07
16.	25	6.54536E-07	6.59427E-07	6.98997E-07	6.57397E-07	6.52744E-07	2.46546E-08	8.80422E-07
17.	26	9.93671E-07	9.70686E-07	9.86269E-07	9.45215E-07	9.45215E-07	3.74088E-08	6.27457E-07
18.	27	1.21409E-07	1.26857E-07	9.67954E-08	5.29846E-07	5.29846E-07	1.09762E-08	5.04942E-07
19.	28	7.76035E-07	6.71106E-07	6.95548E-07	6.70454E-07	5.90141E-07	2.07788E-08	7.28339E-07

ID	CELLS	RADIATION DOSE (MeV) TO RODS / CELLS OF THE CATPHAN PHANTOM (MeV/particle.second)						
		BHF Cu1 0.15 mm	BHF Cu2 0.28 mm	BHF Cu3 0.48 mm	BHF CU4 0.68 mm	BHF Cu5 0.75 mm	BHF Cu6 1.40 mm	BHF Cu7 1.61 mm
20.	29	3.83001E-07	4.46837E-07	4.32350E-07	4.47338E-07	4.56855E-07	3.10127E-08	5.69106E-07
21	30	3.52790E-07	3.78927E-07	3.89955E-07	3.30403E-07	4.92419E-07	2.90712E-08	5.11385E-07
22.	31	6.71593E-07	5.25297E-07	6.00569E-07	5.13091E-07	5.17052E-07	1.61215E-08	2.78881E-07
23.	32	9.26496E-07	9.58862E-07	9.25331E-07	8.89033E-07	9.81182E-07	2.22673E-08	5.83470E-07
24.	33	3.06932E-07	3.03889E-07	3.87185E-07	3.52149E-07	3.66764E-07	1.47116E-08	3.13482E-07
25.	34	1.22104E-06	1.22589E-06	1.25613E-06	1.20839E-06	1.21599E-06	1.75621E-08	1.23903E-06
26.	35	3.79305E-07	3.79305E-07	6.43300E-08	1.15949E-07	1.17907E-07	1.28904E-08	4.10461E-07
27.	36	9.56917E-09	9.56917E-09	3.55095E-08	2.40043E-08	1.55132E-08	1.09170E-08	1.58243E-07
28.	37	7.83147E-07	7.13097E-07	6.18490E-07	6.19920E-07	6.82393E-07	5.05781E-08	6.49635E-07
29.	38	6.78148E-07	7.77585E-07	4.11876E-07	6.75733E-07	5.27648E-07	2.56595E-08	7.82226E-07
30.	39	1.45586E-06	1.45332E-06	1.74903E-06	1.69949E-06	1.55611E-06	2.52809E-08	1.93110E-06
31.	40	1.72579E-07	1.88208E-07	2.13745E-07	1.93340E-07	1.56103E-07	3.29682E-08	1.76839E-07
32.	41	1.33671E-06	1.37672E-06	1.35886E-06	1.58872E-06	1.62414E-06	2.47816E-08	1.48365E-06
33.	42	1.45529E-06	1.45684E-06	1.46751E-06	1.46224E-06	9.00942E-07	2.73307E-08	1.52401E-06
34.	43	2.12500E-07	2.20162E-07	2.20911E-07	2.19501E-07	2.11816E-07	1.85422E-08	4.19458E-07
45.	44	1.02092E-06	9.94233E-07	1.25914E-06	1.00427E-06	1.05546E-06	1.13886E-08	2.13664E-06
36.	45	3.47221E-07	3.90214E-07	4.09941E-07	4.56444E-07	4.45385E-07	2.63961E-08	5.37934E-07
37.	46	2.34766E-06	2.37391E-06	2.34668E-06	2.36502E-06	2.37231E-06	3.25292E-08	2.27484E-06
38.	47	1.19007E-06	1.32892E-06	1.22897E-06	1.17405E-06	1.18266E-06	2.57692E-08	1.04774E-06
39.	48	1.20094E-06	1.20094E-06	1.36383E-06	1.22834E-06	1.35770E-06	7.50959E-09	1.22734E-06
40.	**TOTAL**	**3.85271E-05**	**3.84371E-05**	**3.85963E-05**	**3.94219E-05**	**3.89592E-05**	**9.31413E-07**	**4.01378E-05**

41.	**MEAN DOSE**	**1.92636E-06**	**1.92186E-06**	**1.92981E-06**	**1.97109E-06**	**1.94796E-06**	**4.65706E-08**	**2.00689E-06**

APPENDIX I

Table 4.6: Representation of Radiation dose exposed to cells of the virtual Catphan phantom when filter is conically shaped

ID	CELLS	ENERGY EXPOSED TO CELLS OF THE CATPHAN PHANTOM (MeV/particle.second)						
		CBHF CuT1 0.15 mm	CBHF CuT2 0.28 mm	CBHF CuT3 0.48 mm	CBHF CUT4 0.68 mm	CBHF CuT5 0.75 mm	CBHF CuT6 1.40 mm	CBHF CuT7 1.61 mm
1.	10	4.3494E-07	4.3166E-07	3.8712E-07	3.9632E-07	4.0678E-07	4.6946E-07	4.1241E-07
2.	11	3.4817E-07	4.0769E-07	3.9060E-07	3.3476E-07	4.1333E-07	3.4805E-07	4.0468E-07
3.	12	4.2605E-07	4.4726E-07	4.0413E-07	4.1943E-07	3.9950E-07	3.7546E-07	3.8334E-07
4.	13	2.8787E-07	3.5384E-07	3.8247E-07	4.0583E-07	3.4706E-07	3.2667E-07	2.6034E-07
5.	14	2.2521E-07	2.3749E-07	2.8210E-07	3.1889E-07	2.8966E-07	2.8837E-07	3.2806E-07
6.	15	6.1164E-07	6.2702E-07	5.4003E-07	6.9911E-07	6.9284E-07	5.9995E-07	6.1347E-07
7.	16	7.1552E-07	6.7508E-07	7.3493E-07	7.3488E-07	7.3797E-07	7.0358E-07	5.5486E-07
8.	17	2.0187E-07	2.6065E-07	3.0104E-07	2.6431E-07	2.2126E-07	2.7738E-07	2.6942E-07
9.	18	1.1297E-06	1.0176E-06	1.2763E-06	1.1535E-06	1.0562E-06	6.1578E-07	1.0797E-06
10.	19	4.2612E-07	4.2430E-07	4.0407E-07	4.0319E-07	3.8608E-07	3.9564E-07	3.4739E-07
11.	20	2.9989E-07	2.7715E-07	2.5478E-07	2.5728E-07	2.3359E-07	2.1808E-07	3.1973E-07
12.	21	3.4984E-07	3.7405E-07	3.4862E-07	3.6331E-07	2.9009E-07	2.8036E-07	3.1968E-07
13.	22	4.2886E-07	4.5420E-07	4.3547E-07	4.6264E-07	4.7876E-07	5.1056E-07	4.8756E-07
14.	23	4.1247E-07	4.2357E-07	4.1681E-07	4.0483E-07	4.2977E-07	4.2885E-07	4.1623E-07
15.	24	5.4821E-07	6.2972E-07	6.3361E-07	5.1095E-07	5.4335E-07	5.4121E-07	5.7200E-07
16.	25	3.7405E-07	4.6258E-07	4.5598E-07	3.9056E-07	2.9107E-07	5.3355E-07	5.3103E-07
17.	26	4.9499E-07	7.8764E-07	7.8904E-07	8.6901E-07	8.0539E-07	8.1400E-07	4.5896E-07
18.	27	2.2607E-07	5.6275E-07	3.3327E-07	2.1151E-07	3.1123E-07	3.3761E-07	5.0655E-07
19	28	3.9628E-07	3.6134E-07	3.2366E-07	3.8299E-07	3.2967E-07	3.7113E-07	3.2240E-07
20.	29	3.9509E-07	4.3051E-07	4.0248E-07	4.2179E-07	4.2700E-07	4.1978E-07	3.9817E-07
21.	30	4.2035E-07	4.1983E-07	3.7189E-07	4.1205E-07	3.8536E-07	4.1017E-07	4.1870E-07
22.	31	4.6379E-07	3.8964E-07	4.7196E-07	4.4644E-07	3.7955E-07	3.5008E-07	4.1089E-07
23.	32	5.1191E-07	4.9415E-07	5.4409E-07	5.6111E-07	4.8842E-07	4.3698E-07	4.0706E-07
24.	33	2.9176E-07	2.7544E-07	3.7899E-07	4.1095E-07	4.2794E-07	4.2184E-07	4.3573E-07

ID	CELLS	ENERGY EXPOSED TO CELLS OF THE CATPHAN PHANTOM (MeV/particle.second)						
		CBHF CuT1	CBHF CuT2	CBHF CuT3	CBHF CUT4	CBHF CuT5	CBHF CuT6	CBHF CuT7
		0.15 mm	0.28 mm	0.48 mm	0.68 mm	0.75 mm	1.40 mm	1.61 mm
25.	34	7.4799E-07	7.6025E-07	7.5822E-07	6.3255E-07	6.2688E-07	3.7561E-07	2.8003E-07
26.	35	1.5276E-07	1.5632E-07	1.7910E-07	1.3274E-07	1.6484E-07	3.3521E-07	1.4649E-07
27.	36	2.7757E-07	1.6949E-07	1.9503E-07	1.4252E-07	1.6596E-07	4.3310E-07	3.7631E-07
28.	37	3.8312E-07	4.2337E-07	5.3375E-07	4.0626E-07	4.5190E-07	5.0171E-07	4.7142E-07
29.	38	2.0148E-07	2.1549E-07	1.8730E-07	2.0211E-07	1.7339E-07	2.1011E-07	2.3663E-07
30.	39	2.9280E-07	3.2499E-07	2.3519E-07	2.8855E-07	1.7156E-07	2.8193E-07	2.3809E-07
31.	40	1.8521E-07	2.6545E-07	1.3036E-07	1.4092E-07	1.3559E-07	1.5782E-07	1.9621E-07
32.	41	3.9113E-07	3.1841E-07	3.1826E-07	4.0008E-07	3.2797E-07	3.5608E-07	5.3054E-07
33.	42	3.3718E-07	3.0252E-07	2.8815E-07	3.2980E-07	3.4399E-07	2.8067E-07	2.1485E-07
34.	43	2.3557E-07	2.3278E-07	2.1605E-07	2.0579E-07	3.8764E-07	4.0324E-07	2.1872E-07
45.	44	1.9367E-07	2.4049E-07	2.0021E-07	2.0234E-07	2.7431E-07	2.4805E-07	3.0825E-07
36.	45	3.8167E-07	3.5123E-07	3.6284E-07	3.2607E-07	3.6551E-07	2.6920E-07	2.7301E-07
37.	46	3.0464E-07	3.2221E-07	3.3405E-07	3.3335E-07	3.7815E-07	2.7507E-07	3.6884E-07
38.	47	1.6815E-07	1.7409E-07	1.4026E-07	1.2335E-07	1.7822E-07	1.0815E-07	1.0476E-07
39.	48	1.3011E-07	9.0021E-08	1.0129E-07	1.8363E-07	7.4330E-08	1.9552E-07	3.1614E-07
40.	**SUM TOTAL**	**1.4804E-05**	**1.5572E-05**	**1.5444E-05**	**1.5286E-05**	**1.4992E-05**	**1.4906E-05**	**1.4939E-05**
41.	**MEAN DOSE**	**3.7958E-07**	**3.9929E-07**	**3.9599E-07**	**3.9194E-07**	**3.8441E-07**	**3.8220E-07**	**3.8304E-07**

APPENDIX J

Table 4.7: Deviation of the mean dose from the dose delivered to the Catphan Phantom cells when filters was rectangular

ID	CELLS	DEVIATIONS				
		RBHF Al1	RBHF Al2	RBHF Al3	RBHF Al4	RBHF Al5
		0.5 mm	1.06 mm	2.6 mm	3.03 mm	4.14 mm
1.	10	1.26905E-07	1.42757E-07	1.66447E-07	1.86157E-07	2.11558E-07
2.	11	3.45164E-07	3.55622E-07	3.80778E-07	3.57897E-07	4.39608E-07
3.	12	4.83386E-07	5.84542E-07	6.37747E-07	6.38797E-07	5.76137E-07
4.	13	2.67239E-07	2.68058E-07	3.3889E-07	3.28163E-07	3.31465E-07
5.	14	1.28846E-07	2.76673E-08	2.19197E-07	2.10817E-07	2.67337E-07
6.	15	1.32994E-06	1.18283E-06	7.7799E-07	7.57687E-07	1.78653E-06
7.	16	8.67296E-07	8.74232E-07	7.86507E-07	7.76227E-07	8.05677E-07
8.	17	4.38391E-07	4.38941E-07	3.84627E-07	4.0987E-07	4.40438E-07
9.	18	4.11992E-06	4.66632E-06	4.63344E-06	4.62696E-06	4.63955E-06
10.	19	2.14831E-07	2.01242E-07	2.32419E-07	2.50881E-07	4.00495E-07
11.	20	2.1189E-08	7.58693E-08	3.08645E-08	6.5762E-08	5.83298E-09
12.	21	5.60836E-07	5.84592E-07	6.22737E-07	5.86557E-07	5.05497E-07
13.	22	4.11629E-07	4.14466E-07	4.10172E-07	1.72577E-07	2.38307E-07
14.	23	4.55143E-07	5.3138E-07	4.2497E-07	4.24775E-07	5.12318E-07
15.	24	5.68763E-07	5.59805E-07	5.86253E-07	5.90187E-07	5.69757E-07
16.	25	3.32724E-07	1.88756E-07	3.39897E-07	3.45385E-07	3.73126E-07
17.	26	1.1302E-08	1.70217E-08	1.00365E-08	5.85303E-09	5.7115E-08
18.	27	7.73222E-07	8.4743E-07	4.58471E-07	9.04244E-07	4.66065E-07
19	28	3.1306E-07	1.79032E-07	3.57356E-07	3.49391E-07	4.31646E-07
20.	29	6.03781E-07	6.04896E-07	5.54289E-07	5.83195E-07	4.61585E-07

ID	CELLS	DEVIATIONS				
		RBHF Al1	**RBHF Al2**	**RBHF Al3**	**RBHF Al4**	**RBHF Al5**
		0.5 mm	**1.06 mm**	**2.6 mm**	**3.03 mm**	**4.14 mm**
21	30	6.94048E-07	6.1933E-07	5.66655E-07	7.46297E-07	5.70485E-07
22.	31	2.90987E-07	4.55545E-07	4.7728E-07	5.04947E-07	7.17768E-07
23.	32	2.9857E-08	6.82513E-08	8.06755E-08	8.5606E-08	1.24153E-07
24.	33	6.75556E-07	6.99552E-07	6.38591E-07	6.51987E-07	6.67124E-07
25.	34	2.32936E-07	2.31562E-07	2.75637E-07	2.89467E-07	2.74687E-07
26.	35	6.69199E-07	6.12863E-07	8.57995E-07	8.77625E-07	8.86041E-07
27.	36	9.77045E-07	9.82885E-07	9.47691E-07	9.9616E-07	1.00736E-06
28.	37	2.36547E-07	3.70263E-07	3.79215E-07	4.06486E-07	4.00708E-07
29.	38	4.18266E-07	4.04568E-07	2.74169E-07	3.07553E-07	9.4882E-08
30.	39	4.69246E-07	5.90122E-07	6.28807E-07	6.30387E-07	1.03226E-06
31.	40	7.98487E-07	8.84142E-07	8.88139E-07	8.8283E-07	5.64124E-07
32.	41	4.92576E-07	3.77272E-07	6.75907E-07	6.24567E-07	2.74017E-07
33.	42	4.98376E-07	4.49502E-07	1.71935E-08	4.64557E-07	4.40917E-07
34.	43	7.70662E-07	7.81919E-07	7.82145E-07	7.77255E-07	8.04281E-07
45.	44	3.4306E-08	5.05172E-09	8.05653E-09	-7.33028E-10	1.72367E-07
36.	45	5.43967E-07	6.23858E-07	4.98389E-07	5.07908E-07	6.07857E-07
37.	46	1.35985E-06	1.36407E-06	1.37784E-06	1.34706E-06	1.29175E-06
38.	47	1.99246E-07	2.04162E-07	1.88367E-07	1.90397E-07	1.42137E-07
39.	48	2.11216E-07	2.07822E-07	2.31327E-07	2.03937E-07	1.98117E-07
40.	**Total**	**2.19759E-05**	**2.26782E-05**	**2.21472E-05**	**2.30657E-05**	**2.37911E-05**
41.	**Mean Dose Deviation**	**5.63485E-07**	**5.81493E-07**	**5.67876E-07**	**5.91427E-07**	**6.10027E-07**

APPENDIX K

Table 4.8: Deviation of the mean dose from the dose delivered to the Catphan Phantom cells when filters was conically-shaped

SN	CELLS	DEVIATIONAL ANALYSIS FOR IMAGE QUALITY				
		CBHF Al1	CBHF Al2	CBHF Al3	CBHF Al4	CBHF Al5
		0.53 mm	1.06 mm	2.60 mm	3.08 mm	4.14 mm
1.	10	8.5156E-08	1.87589E-08	4.30176E-08	3.24676E-08	5.77483E-08
2.	11	9.85097E-09	1.34391E-08	1.73126E-08	1.56374E-08	1.66553E-08
3.	12	2.14103E-09	2.16579E-08	6.01304E-08	5.67338E-09	9.13587E-08
4.	13	6.193E-08	6.67091E-08	6.97744E-08	3.39264E-08	4.99827E-08
5.	14	7.41603E-09	1.13306E-07	7.87766E-08	1.59703E-07	1.03063E-07
6.	15	2.10028E-07	1.29324E-07	7.79086E-08	1.29612E-07	2.69793E-08
7.	16	5.4741E-08	6.17119E-08	4.21543E-09	1.38404E-08	1.00463E-08
8.	17	1.8442E-07	2.85432E-07	3.11846E-07	9.14676E-08	2.40949E-07
9.	18	1.15165E-06	1.14132E-06	1.13569E-06	1.22872E-06	1.21409E-06
10.	19	2.8549E-08	3.22911E-08	8.76057E-09	2.19938E-09	1.44247E-08
11.	20	1.10898E-07	1.36319E-07	1.30481E-07	1.11047E-07	9.86673E-08
12.	21	1.12454E-07	1.03575E-07	1.00616E-07	3.33556E-08	5.43433E-09
13.	22	2.6376E-08	4.24194E-09	1.56752E-07	1.02902E-07	9.22283E-08
14.	23	6.8163E-08	1.22235E-07	1.15137E-07	4.92664E-08	8.63737E-08
15.	24	2.51017E-07	5.94101E-08	2.82176E-08	6.02706E-08	9.44163E-08
16.	25	5.8452E-08	5.07649E-08	6.20036E-08	1.80624E-07	1.43145E-07
17.	26	2.06298E-07	2.00078E-07	2.81971E-07	1.8706E-07	1.54399E-07
18.	27	2.81599E-07	1.28367E-07	1.11658E-07	1.78556E-08	1.72713E-08
19	28	3.6306E-08	1.32499E-08	3.49657E-09	2.12184E-08	1.22087E-08
20.	29	1.2E-08	1.19337E-07	1.36971E-07	8.35424E-08	3.71277E-08
21.	30	1.8174E-08	2.32631E-08	8.45186E-08	2.91716E-08	6.90783E-08
22.	31	9.4197E-08	3.95069E-08	1.33474E-07	9.14304E-08	3.89093E-08
23.	32	3.6405E-08	6.86391E-08	1.25968E-07	6.39206E-08	6.68267E-08
24.	33	1.43775E-07	7.98749E-08	3.39004E-08	1.21162E-09	5.87467E-09

SN	CELLS	DEVIATIONAL ANALYSIS FOR IMAGE QUALITY				
		CBHF Al1 0.53 mm	CBHF Al2 1.06 mm	CBHF Al3 2.60 mm	CBHF Al4 3.08 mm	CBHF Al5 4.14 mm
25.	34	9.9398E-08	1.91705E-07	1.28724E-07	2.56449E-07	2.32035E-07
26.	35	2.01566E-07	1.37151E-07	2.35188E-07	7.72656E-08	2.07267E-08
27.	36	3.798E-07	4.13365E-07	4.04929E-07	4.11985E-07	4.15556E-07
28.	37	1.565E-07	1.49386E-07	1.44416E-07	7.14466E-08	1.07241E-07
29.	38	2.76643E-07	2.29991E-07	1.49544E-07	2.62917E-07	2.78725E-07
30.	39	6.8191E-08	5.22829E-08	5.36996E-08	4.90126E-08	4.09553E-08
31.	40	1.6714E-07	1.68753E-07	1.81526E-07	1.35165E-07	1.52905E-07
32.	41	6.164E-08	7.22619E-08	6.24536E-08	8.43896E-08	1.06244E-07
33.	42	1.1824E-08	4.26151E-08	1.05459E-07	1.20034E-08	3.72043E-08
34.	43	2.6765E-08	3.69779E-08	3.74416E-08	1.26304E-08	5.54967E-09
45.	44	4.70097E-09	1.18519E-08	2.73549E-07	1.34734E-08	1.68447E-08
36.	45	5.44597E-09	1.91201E-08	1.93876E-08	1.53713E-07	6.53287E-08
37.	46	2.15997E-07	2.02652E-07	1.36929E-07	1.45773E-07	1.2926E-07
38.	47	1.2358E-07	3.60359E-08	4.98686E-08	2.74396E-08	2.94383E-08
39.	48	7.9174E-08	1.08566E-07	7.80024E-08	1.30284E-07	7.77953E-08
40	**TOTAL**	**5.13036E-06**	**4.90553E-06**	**5.37371E-06**	**4.59007E-06**	**4.46307E-06**
41.	**MEAN DOSE DEVIATION**	**1.3155E-07**	**1.2578E-07**	**1.3779E-07**	**1.177E-07**	**1.1444E-07**

APPENDIX L

Table 4.9: Deviation of mean dose from the dose delivered to the Catphan Phantom cells when filter was rectangular

SN	CELLS	DEVIATION						
		RBHF Cu1 0.15 mm	RBHF Cu2 0.28 mm	RBHF Cu3 0.48 mm	RBHF CU4 0.68 mm	RBHF Cu5 0.75 mm	RBHF Cu6 1.40 mm	RBHF Cu7 1.61 mm
1.	10	1.486E-07	2.341E-07	1.497E-07	1.744E-07	7.895E-08	5.850E-09	2.533E-07
2.	11	3.417E-07	3.134E-07	1.659E-07	4.579E-07	1.508E-07	1.435E-08	3.640E-07
3.	12	4.252E-07	4.036E-07	5.660E-07	5.546E-07	5.974E-07	5.039E-09	3.417E-07
4.	13	2.727E-07	2.665E-07	2.766E-07	2.861E-07	3.582E-07	3.000E-09	4.094E-07
5.	14	9.138E-09	1.014E-08	1.080E-08	1.214E-07	6.183E-08	1.095E-08	6.072E-08
6	15	1.200E-06	1.199E-06	1.225E-06	1.150E-06	1.108E-06	1.313E-08	8.610E-07
7	16	8.543E-07	8.688E-07	9.133E-07	8.304E-07	8.231E-07	7.269E-10	7.230E-07
8	17	4.471E-07	4.414E-07	6.079E-07	4.062E-07	5.233E-07	1.433E-08	6.688E-07
9	18	4.750E-06	4.454E-06	4.216E-06	4.625E-06	4.648E-06	9.091E-09	4.585E-06
10.	19	2.730E-07	2.576E-07	2.006E-07	3.135E-07	2.779E-07	1.116E-08	3.907E-07
11.	20	9.177E-08	4.863E-08	1.179E-07	1.912E-08	4.048E-08	1.331E-09	2.467E-07
12.	21	3.757E-07	3.682E-07	3.733E-07	2.491E-07	3.367E-07	2.316E-09	3.997E-07
13.	22	2.826E-07	2.755E-07	3.897E-07	1.640E-07	3.317E-07	2.321E-09	1.437E-07
14.	23	4.636E-07	4.601E-07	4.051E-07	2.337E-07	2.460E-07	2.198E-08	2.021E-07
15.	24	5.808E-07	5.813E-07	4.572E-07	5.857E-07	5.463E-07	8.831E-10	5.886E-07
16.	25	3.333E-07	3.261E-07	2.907E-07	3.534E-07	3.462E-07	7.722E-10	1.488E-07
17.	26	5.796E-09	1.488E-08	3.379E-09	6.560E-08	5.374E-08	1.353E-08	4.017E-07
18.	27	8.665E-07	8.587E-07	8.929E-07	4.810E-07	4.691E-07	1.291E-08	5.242E-07
19	28	2.118E-07	3.145E-07	2.941E-07	3.404E-07	4.088E-07	3.104E-09	3.008E-07
20.	29	6.049E-07	5.387E-07	5.573E-07	5.635E-07	5.421E-07	7.130E-09	4.601E-07
21	30	6.351E-07	6.066E-07	5.997E-07	6.804E-07	5.065E-07	5.189E-09	5.178E-07

SN	CELLS	DEVIATION						
		RBHF Cu1 0.15 mm	RBHF Cu2 0.28 mm	RBHF Cu3 0.48 mm	RBHF CU4 0.68 mm	RBHF Cu5 0.75 mm	RBHF Cu6 1.40 mm	RBHF Cu7 1.61 mm
22.	31	3.163E-07	4.603E-07	3.891E-07	4.977E-07	4.819E-07	7.761E-09	7.503E-07
23.	32	6.138E-08	2.670E-08	6.432E-08	1.218E-07	1.777E-08	1.615E-09	4.457E-07
24.	33	6.809E-07	6.817E-07	6.025E-07	6.587E-07	6.322E-07	9.171E-09	7.157E-07
25.	34	2.332E-07	2.403E-07	2.665E-07	1.976E-07	2.170E-07	6.320E-09	2.099E-07
26.	35	6.086E-07	6.063E-07	9.253E-07	8.949E-07	8.810E-07	1.099E-08	6.187E-07
27.	36	9.783E-07	9.760E-07	9.541E-07	9.868E-07	9.834E-07	1.297E-08	8.709E-07
28.	37	2.047E-07	2.725E-07	3.712E-07	3.909E-07	3.166E-07	2.670E-08	3.795E-07
29.	38	3.097E-07	2.080E-07	5.778E-07	3.351E-07	4.713E-07	1.777E-09	2.469E-07
30.	39	4.680E-07	4.678E-07	7.594E-07	6.887E-07	5.572E-07	1.399E-09	9.019E-07
31.	40	8.153E-07	7.974E-07	7.759E-07	8.175E-07	8.429E-07	9.086E-09	8.523E-07
32.	41	3.488E-07	3.912E-07	3.692E-07	5.779E-07	6.252E-07	8.992E-10	4.545E-07
33.	42	4.674E-07	4.713E-07	4.779E-07	4.514E-07	9.801E-08	3.448E-09	4.948E-07
34.	43	7.754E-07	7.654E-07	7.687E-07	7.913E-07	7.871E-07	5.340E-09	6.097E-07
45.	44	3.305E-08	8.666E-09	2.695E-07	6.547E-09	5.651E-08	1.249E-08	1.107E-06
36.	45	6.407E-07	5.954E-07	5.797E-07	5.544E-07	5.536E-07	2.514E-09	4.912E-07
37.	46	1.360E-06	1.388E-06	1.357E-06	1.354E-06	1.373E-06	8.647E-09	1.246E-06
38.	47	2.022E-07	3.434E-07	2.393E-07	1.632E-07	1.837E-07	1.887E-09	1.856E-08
39.	48	2.131E-07	2.154E-07	3.742E-07	2.175E-07	3.587E-07	1.637E-08	1.982E-07
40.	**TOTAL**	**2.189E-05**	**2.176E-05**	**2.283E-05**	**2.236E-05**	**2.189E-05**	**2.985E-07**	**2.320E-05**
41.	**MEAN DOSE DEVIATION**	**5.613E-07**	**5.579E-07**	**5.855E-07**	**5.734E-07**	**5.613E-07**	**7.653E-09**	**5.950E-07**

APPENDIX M

Table 4.10: Deviation of mean dose from the dose delivered to the Catphan Phantom cells when filter was conically-shaped

ID	CELLS	DEVIATION ANALYSIS FOR IMAGE QUALITY						
	CELLS	CBHF CuT1 0.15 mm	CBHF CuT2 0.28 mm	CBHF CuT3 0.48 mm	CBHF CUT4 0.68 mm	CBHF CuT5 0.75 mm	CBHF CuT6 1.40 mm	CBHF CuT7 1.61 mm
1.	10	5.53565E-08	3.23724E-08	8.87069E-09	4.38038E-09	2.23704E-08	8.72506E-08	2.93711E-08
2.	11	3.14075E-08	8.39845E-09	5.38769E-09	5.71856E-08	2.89114E-08	3.41564E-08	2.16331E-08
3.	12	4.64655E-08	4.79754E-08	8.14231E-09	2.74864E-08	1.50834E-08	6.74838E-09	2.98077E-10
4.	13	9.17125E-08	4.54446E-08	1.35147E-08	1.38894E-08	3.73496E-08	5.55324E-08	1.22702E-07
5.	14	1.54366E-07	1.61804E-07	1.13893E-07	7.30496E-08	9.47516E-08	9.38384E-08	5.49819E-08
6.	15	2.32055E-07	2.27733E-07	1.44041E-07	3.07168E-07	3.08421E-07	2.1775E-07	2.3043E-07
7.	16	3.35936E-07	2.75788E-07	3.38946E-07	3.42938E-07	3.53551E-07	3.2138E-07	1.71815E-07
8.	17	1.77708E-07	1.38636E-07	9.49477E-08	1.27635E-07	1.63157E-07	1.04829E-07	1.13625E-07
9.	18	7.5011E-07	6.18291E-07	8.80332E-07	7.61598E-07	6.71826E-07	2.33574E-07	6.96688E-07
10.	19	4.65345E-08	2.50094E-08	8.08431E-09	1.12494E-08	1.66442E-09	1.34316E-08	3.56569E-08
11.	20	7.96935E-08	1.2214E-07	1.41205E-07	1.34663E-07	1.50825E-07	1.64127E-07	6.33079E-08
12.	21	2.97435E-08	2.52356E-08	4.73667E-08	2.86316E-08	9.43256E-08	1.01848E-07	6.33659E-08
13.	22	4.92765E-08	5.49074E-08	3.94863E-08	7.06934E-08	9.43444E-08	1.28354E-07	1.04514E-07
14.	23	3.28885E-08	2.42784E-08	2.08243E-08	1.28844E-08	4.53534E-08	4.66446E-08	3.31841E-08
15.	24	1.6863E-07	2.30435E-07	2.37623E-07	1.19006E-07	1.58934E-07	1.59002E-07	1.88961E-07
16.	25	5.52949E-09	6.32954E-08	5.99943E-08	1.38262E-09	9.33456E-08	1.51342E-07	1.47986E-07
17.	26	1.15407E-07	3.88347E-07	3.93054E-07	4.77071E-07	4.20977E-07	4.31791E-07	7.59211E-08
18.	27	1.53509E-07	1.63465E-07	6.27157E-08	1.80432E-07	7.31826E-08	4.45904E-08	1.23504E-07
19	28	1.67005E-08	3.79446E-08	7.23257E-08	8.94862E-09	5.47476E-08	1.10764E-08	6.06399E-08
20.	29	1.55065E-08	3.12234E-08	6.48831E-09	2.98454E-08	4.25874E-08	3.75706E-08	1.51301E-08
21.	30	4.07665E-08	2.05404E-08	2.40997E-08	2.01064E-08	9.48415E-10	2.79676E-08	3.56561E-08
22.	31	8.42105E-08	9.65055E-09	7.59713E-08	5.44974E-08	4.86258E-09	3.21244E-08	2.78511E-08
23.	32	1.32329E-07	9.48634E-08	1.48097E-07	1.69165E-07	1.0401E-07	5.47796E-08	2.40181E-08
24.	33	8.78245E-08	1.23852E-07	1.69977E-08	1.90104E-08	4.35244E-08	3.96306E-08	5.26901E-08
25.	34	3.68414E-07	3.60962E-07	3.6223E-07	2.40604E-07	2.42465E-07	6.59438E-09	1.03016E-07

ID	CELLS	DEVIATION ANALYSIS FOR IMAGE QUALITY						
		CBHF CuT1 0.15 mm	CBHF CuT2 0.28 mm	CBHF CuT3 0.48 mm	CBHF CUT4 0.68 mm	CBHF CuT5 0.75 mm	CBHF CuT6 1.40 mm	CBHF CuT7 1.61 mm
26.	35	2.26824E-07	2.4297E-07	2.16885E-07	2.59205E-07	2.19576E-07	4.69964E-08	2.36557E-07
27.	36	1.02014E-07	2.29795E-07	2.00961E-07	2.49421E-07	2.18453E-07	5.08996E-08	6.73692E-09
28.	37	3.53751E-09	2.40784E-08	1.37762E-07	1.43224E-08	6.74884E-08	1.19501E-07	8.83761E-08
29.	38	1.78101E-07	1.83799E-07	2.0869E-07	1.89835E-07	2.11029E-07	1.72098E-07	1.46415E-07
30.	39	8.67835E-08	7.42966E-08	1.60803E-07	1.03389E-07	2.12859E-07	1.00278E-07	1.44954E-07
31.	40	1.94372E-07	1.33839E-07	2.65624E-07	2.51027E-07	2.48825E-07	2.24383E-07	1.86831E-07
32.	41	1.15495E-08	8.08786E-08	7.77247E-08	8.13538E-09	5.64406E-08	2.61224E-08	1.47494E-07
33.	42	4.23975E-08	9.67646E-08	1.0784E-07	6.21376E-08	4.04206E-08	1.01531E-07	1.68197E-07
34.	43	1.44013E-07	1.66511E-07	1.79935E-07	1.86153E-07	3.22342E-09	2.10326E-08	1.64323E-07
45.	44	1.8591E-07	1.58804E-07	1.95778E-07	1.89602E-07	1.10104E-07	1.34151E-07	7.47909E-08
36.	45	2.08451E-09	4.80556E-08	3.31477E-08	6.58716E-08	1.89026E-08	1.13001E-07	1.10034E-07
37.	46	7.49375E-08	7.70826E-08	6.19377E-08	5.85916E-08	6.25958E-09	1.07134E-07	1.42019E-08
38.	47	2.11432E-07	2.25201E-07	2.55729E-07	2.68589E-07	2.0619E-07	2.74054E-07	2.78281E-07
39.	48	2.49471E-07	3.09268E-07	2.94703E-07	2.08308E-07	3.10084E-07	1.8668E-07	6.69049E-08
40.	**SUM TOTAL**	**5.01551E-06**	**5.38393E-06**	**5.72216E-06**	**5.40811E-06**	**5.25137E-06**	**4.2838E-06**	**4.43104E-06**
41.	**MEAN DOSE DEVIATION**	**1.28603E-07**	**1.3805E-07**	**1.46722E-07**	**1.38669E-07**	**1.34651E-07**	**1.09841E-07**	**1.13616E-07**